Alma Mater Studiorum
Università degli studi di Bologna

Department of Electrical, Electronic
and Information Engineering "Guglielmo Marconi"

Scuola di Dottorato in Bioingegneria - Ciclo XXV
Settore concorsuale di afferenza: 09/G2
Settore scientifico disciplinare di afferenza: ING-INF/06

Computational modelling of human stem cell-derived cardiomyocytes - Texture descriptors for biological image processing

presented by
Michelangelo Paci

Supervisor
Prof. Gianni Gnudi

Co-supervisor
Prof. Stefano Severi

Reviewers
Prof. Claudio Lamberti
Prof. Cristiana Corsi
Prof. Beatriz Trénor

Ph.D. Coordinator
Prof. Angelo Cappello

Year 2013, Final Exam

KEYWORDS

Cardiomyocytes
Computational models
Human embryonic stem cells
Human induced pluripotent stem cells
Current blockers
-
Image classification
Texture descriptors

ACRONYMS

I_{K1}	inward rectifier K^+ current
I_{Na}	Na^+ current
I_{Kr}	rapid delayed rectifier K^+ current
I_{Ks}	slow delayed rectifier K^+ current
I_{CaL}	L-type Ca^{2+} current
I_{CaT}	T-type Ca^{2+} current
I_{to}	transient outward K^+ current
I_f	funny current
I_{NaK}	Na^+ /K^+ pump
I_{NaCa}	Na^+ /Ca^{2+} exchanger
I_{pCa}	sarcolemmal Ca^{2+} -ATPase
I_{bCa}	Background Ca^{2+} current
I_{up}	Sarcoplasmic Reticulum (SR) uptake current
I_{rel}	SR release current
I_{leak}	SR leakage current
I_{stim}	Stimulus current

AP	Action Potential
APA	Action Potential Amplitude
APD	Action Potential Duration
APD_{10}	APD at 10% of repolarization
APD_{30}	APD at 30% of repolarization
APD_{40}	APD at 40% of repolarization
APD_{50}	APD at 50% of repolarization
APD_{70}	APD at 70% of repolarization
APD_{80}	APD at 80% of repolarization
APD_{90}	APD at 90% of repolarization
CaMK	Ca2+/calmodulin-dependent protein kinase II
Chr	3R4S-Chromanol 293B
CM	cardiomyocyte
Cm	Membrane capacitance
DDR	Diastolic Depolarization Rate
EAD	Early After Depolarization
EB	Embryod Body
EC	excitation/contraction
F	Rate of spontaneous beating
hESC	human embryonic stem cell
hiPSC	human induced pluripotent stem cell
hESC-CM	human embryonic stem cell-derived cardiomyocyte
hiPSC-CM	human induced pluripotent stem cell-derived cardiomyocyte

LQTS	Long QT Syndrome
MDP	Maximum Diastolic Potential
Nifed	Nifedipine
ORd	O'Hara - Rudy
Peak	Peak Voltage
SR	Sarcoplasmic Reticulum
TTX	Tetrodotoxine
$\mathbf{V_c}$	Cell volume
$\mathbf{V_{max}}$	Maximum Upstroke Velocity
$\mathbf{V_{maxCa,upstroke}}$	Ca^{2+} transient Maximum Upstroke Velocity
$\mathbf{V_{maxCa,decay}}$	Ca^{2+} transient Maximum Decay Velocity
$\mathbf{V_{SR}}$	Sarcoplasmic Reticulum volume
ANA	Antibody Antinucleus
ASM	Angular Second Moment
AUC	area under the ROC curve
FUSr	fusion by sum rule between MLQPr and MLPQ3
FUSu	fusion by sum rule between MLQPu and MLPQ3
GLCM	Grey Level Co-occurence Matrix
HAR	Haralick features
IIF	Indirect Immunofluorescence
L(3)	LPQ with radius = 3 pixels
L(5)	LPQ with radius = 5 pixels
L(3+5)	concatenation of the bins extracted by L(3) and L(5)

LBP	Local Binary Pattern
LE	Locate Endogenous
LPQ3	single LPQ with ternary coding
LPQ	Local Phase Quantization
LPQ3	LPQ with ternary coding
LQP	Local Quinary Pattern
LQPu	LQP with uniform mapping
LT	Locate Transfected
LTPu	single LTP with uniform mapping
LTP	Local Ternary Pattern
MLPQ3	Multi-Threshold LPQ3
MLQP	Multi-Threshold LQP
MLQPr	Multi-Threshold LQP with rotation invariant uniform mapping
MLQPu	Multi-Threshold LQP with uniform mapping
MLTPu	Multi-Threshold LTP with uniform mapping
RU(8)	rotation invariant uniform bins extracted using LBP with radius = 8 pixels
RU(16)	rotation invariant uniform bins extracted using LBP with radius = 16 pixels
RU(8+16)	concatenation of the bins extracted by RU(8) and RU(16)
STFT	Short Term Fourier Transform
SVM	Support Vector Machine
U(8)	uniform bins extracted using LBP with radius = 8 pixels
U(16)	uniform bins extracted using LBP with radius = 16 pixels

U(8+16)	concatenation of the bins extracted by U(8) and U(16)
VE	Methods to compute the LTP proposed by Véscei *at al.* in Comput Bio Med 2011; 41(6): 313-25.
VLQ	VE method applied to LQP
MV1	VE variant where a different threshold is calculated for each class in each dataset

CONTENTS

GENERAL INTRODUCTION

The main focus of this thesis deals with the mathematical modelling of the electrophysiology of human stem cells differentiated towards cardiomyocytes. Starting from the last decades of the twentieth century, challenging hopes about new treatments for tissues and organ replacements, commonly gathered under the name of regenerative medicine, were raised by seminal works such as [1, 2]. Evans *et al.* [1] showed in 1981 the feasibility of isolating pluripotent stem cells from mouse embryos and the ability of these cells in differentiating both *in-vitro* and *in-vivo* by generating teratomas, while in 1998 Thomson *et al.* [2] succeeded in isolating pluripotent stem cell lines from human embryos, i.e. *human embryonic stem cells (hESCs)*. Moreover in recent years, Yamanaka's [3] and Thomson's [4] groups were able to reprogram somatic cells from mice and humans into pluripotent cells capable to differentiate into various tissues. Dealing with *human induced pluripotent stem cells (hiPSCs)* brings several advantages, such as the *patient-specificity*, the *disease-specificity* and no use of embryos thus avoiding ethical issues.

The weak capability of adult heart of regenerate and undergo extensive repair increased the interest in differentiating human stem cells into cardiomyocytes to be used to create *in-vitro* cardiac tissue useful for replacing damaged myocardial areas, e.g. after infarction. Although functional cardiomyocytes can be differentiated, namely *human embryonic stem cell-derived cardiomyocytes (hESC-CMs)* and *human induced pluripotent stem cell-derived cardiomyocytes (hiPSC-CMs)*, they are not used for treatments and therapies yet, but they already represent well-established *in-vitro* models for basic research in electrophysiology and pharmaceutical studies.

Supporting the *in-vitro* practice with *in-silico* models can represent a strategic choice, that has potential to reduce the number of costly and time consuming in-vitro experiments. *In-silico* models could help in verifying hypotheses, in formulating new ones as well as in planning new experiments. The current models of the adult cardiac Action Potential (AP) result inadequate in describing the hESC-CM/hiPSC-CM electrophysiology, due to the differences between hESC-CMs/hiPSC-CMs and adult myocytes such as (i) the immaturity of hESC-CMs and hiPSC-CMs, (ii) their spontaneous electrical activity, i.e. APs firing without an external stimulus [5, 6], and (iii) the different AP shape [5, 6]. The first aim of this thesis is developing new models of the AP of hESC-CMs and hiPSC-CMs useful for a deeper understanding of their electrophysiological properties and their development, also in order to fill the gap between *in-vitro* and *in-silico* models.

This thesis investigates also a secondary topic, the use of texture descriptors for biological image processing. The author's interest on this topic was born during the preliminary processing of datasets of hESC and hiPSC images and constantly grew until texture analysis became an independent line of research during the Ph.D. education, worth to be detailed in a dedicated part of this thesis. Usually, texture descriptors and texture analysis were commonly used for biometric applications such as face recognition [7] or fingerprint matching [8] but their use resulted successful also on diagnostic images. For instance in [9] the Local Binary Pattern (LBP) operator was used to discern between normal parenchyma and tumoral masses in mammographic images, or in [10] LBP was used to assign a seriuosness score to endoscopical images of celiac patients. The second aim of this thesis is assessing the discriminant power of new variants of the state of the art texture descriptors (such as LBP or Local Phase Quantization (LPQ)) based on non-binary codings, in particular in classifying biological (cellular and sub-cellular) images.

Walkthrough

Because of the dual line of research followed in this thesis, it was organized in two distinct parts. Part I deals with the modelling of the AP of hESC-CMs and hiPSC-CMs while Part II investigates new variants of texture descriptors useful for biological image processing applications.

Part I outline

In Chapter 1 a brief overview on hESC/hiPSC isolation and differentiation into cardiomyocytes (CMs) is exposed: the aim of this section is not to fully describe the stem cell universe, but to provide the reader with the basic ideas about the biology of hESCs and hiPSCs only, which will result useful in the comprehension of the rest of Part I. For the same reason, also the basic concepts about CM electrophysiology and AP modelling are summarized. The first computational model developed during this Ph.D. , the hESC-CM model, is detailed in Chapter 2: this model represents the first model in literature trying to provide a comprehensive description of the electrophysiology of hESC-CMs and reproducing APs and Ca^{2+} transients at two different developmental stages, identified during the hESC-CM maturation process [6]: *Early* (between 15 and 40 days of differentiation) and *Late* (between 50 and 110 days of differentiation). Moreover it was tested also in reproducing the AP morphologial changes due (i) to the application of 2 of prototypical current blockers and (ii) to the coupling with a fibroblast model. This study was carried out in collaboration with the University of Florence (Italy). Chapter 3 describes the second computational model developed during this Ph.D. , the hiPSC-CM model, able to reproduce the AP of two different phenotypes, the *ventricular-like* and the *atrial-like* phenotype [5]. Moreover it was validated also against 4 different current blockers and finally applied to formulate specific hypotheses about the ionic currents responsible of the differences between hiPSC-CM and adult CM APs. In order to speculate on what ventricular-like hiPSC-CMs lack with respect to adult ventricular CMs, we merged the hiPSC-CM model with the state of the art O'Hara-Rudy model of adult ventricular cell [11].

Part II outline

Chapter 1 presents a brief introduction about the usage of texture descriptors, in particular for biological and diagnostic applications and afterwards describes the basic operators used in the following chapters of Part II such as Haralick features, LBP and LPQ as well as their variants making use of *non-binary codings* [12] and of the *multi-threshold approach.* Chapter 2 is focused on the use of non-binary codings for the LBP and LPQ operators, in particular the ternary coding and the quinary coding, and on the multi-threshold approach. The aim of this chapter is providing a well assessed feature set for classifying biological data sets. In fact 6 datasets of subcellular parts (mostly protein localization) and of cells (hESC-CMs and hiPSC-CMs) were classified showing the effectiveness of non-binary codings and of the multi-threshold approach [13]. Chapter 3 shows a further application of non-binary coded and multi-thresholded texture descriptors, in fact a classification method is proposed for the staining patterns observable during the Antibody Antinucleus (ANA) test. This work was born due to the clinical need of quantifying (i) the level of fluorescence from Indirect Immunofluorescence (IIF) pictures and (ii) the staining patterns observable in those pictures. If the first activity is not difficult for an expert human observer, the second one results to be critical thus making the use of an automated system helpful for the physician.

Bibliography

[1] Evans M, Kaufman M. Establishment in culture of pluripotential cells from mouse embryos. Nature 1981;292(5819):154–156.

[2] Thomson JA. Embryonic Stem Cell Lines Derived from Human Blastocysts. Science 1998;282:1145–1147.

[3] Takahashi K, Tanabe K, Ohnuki M, Narita M, Ichisaka T, Tomoda K, Yamanaka S. Induction of pluripotent stem cells from adult human fibroblasts by defined factors. Cell November 2007;131(5):861–872.

[4] Yu J, Vodyanik MA, Smuga-Otto K, Antosiewicz-Bourget J, Frane JL, Tian S, Nie J, Jonsdottir GA, Ruotti V, Stewart R, Slukvin II, Thomson JA. Induced Pluripotent Stem Cell Lines Derived from Human Somatic Cells. Science 2007;318(5858):1917–1920.

[5] Ma J, Guo L, Fiene S, Anson B, Thomson J, Kamp T, Kolaja K, Swanson B, January C. High purity human-induced pluripotent stem cell-derived cardiomyocytes: electrophysiological properties of action potentials and ionic currents. Am J Physiol Heart Circ Physiol November 2011;301(5):H2006–H2017.

[6] Sartiani L, Bettiol E, Stillitano F, Mugelli A, Cerbai E, Jaconi ME. Developmental changes in cardiomyocytes differentiated from human embryonic

stem cells: a molecular and electrophysiological approach. Stem Cells 2007; 25(5):1136–1144.

[7] Ahonen T, Hadid A, Pietikäinen M. Face description with local binary patterns: application to face recognition. IEEE transactions on pattern analysis and machine intelligence December 2006;28(12):2037–41.

[8] Nanni L, Lumini A. Local binary patterns for a hybrid fingerprint matcher. Pattern Recognition 2008;41(11):3461–66.

[9] Oliver A, Lladó X, Freixenet J, Martí J. False positive reduction in mammographic mass detection using local binary patterns. MICCAI International Conference on Medical Image Computing and Computer Assisted Intervention January 2007;10(Pt 1):286–93.

[10] Vécsei A, Amann G, Hegenbart S, Liedlgruber M, Uhl A. Automated Marsh-like classification of celiac disease in children using local texture operators. COMPUT BIOL MED April 2011;41(6):313–25.

[11] O'hara T, Virág L, Varró A, Rudy Y. Simulation of the Undiseased Human Cardiac Ventricular Action Potential: Model Formulation and Experimental Validation. PLoS Comput Biol May 2011;7(5):e1002061. ISSN 1553-7358.

[12] Nanni L, Lumini A, Brahnam S. Local binary patterns variants as texture descriptors for medical image analysis. ARTIF INTELL MED 2010; 49(2):117–25.

[13] Paci M, Nanni L, Lahti A, Aalto-Setälä K, Hyttinen J, Severi S. Non-Binary Coding for Texture Descriptors in Sub-Cellular and Stem Cell Image Classification. CURR BIOINFORM 2013;.

Part I

Human stem cell-derived cardiomyocyte functional assessment by means of modelling

CHAPTER

ONE

A BRIEF OVERVIEW ON HUMAN PLURIPOTENT STEM CELLS, THE CARDIAC ACTION POTENTIAL AND ITS COMPUTATIONAL MODELLING

1.1 Human stem cells and differentiation into cardiomyocytes

This section does not have the ambition to fully review the wide universe of human stem cells, instead it aims to provide the basic information of what a stem cell is and the necessary details to focus the *in-vitro* models we turned into *in-silico* models in chapters 2 and 3. According to the definition reported in [1] “a stem cell is a cell that can continuously produce unaltered daughters and also has the ability to produce daughter cells that have different, more restricted properties”. In spite of the informality of this definition, it implies two fundamental properties of stem cells:

- *self-renewal*, the ability to go through numerous cycles of division that repeatedly generate at least one daughter equivalent to the mother cell with latent capacity for differentiation [1];
- *potency*, the range of commitment options available to a cell [1], i.e. the capacity to differentiate into specific and specialized cells.

The different levels of potency characterizing stem cells were summarized in [1, 2]:

- *totipotent*, sufficient to form the whole organism. They can differentiate into embryonic and extra-embryonic cell types, i.e. all the lineages necessary to construct a complete organism. Totipotent cells derive from the fusion of a sperm cell and an egg cell.
- *pluripotent*, able to form all the body cell lineages. They can differentiate into all the embryonic cell types but not into the extra-embryonic ones, i.e. they can produce all the body cell lineages including the 3 germ layers (eg. embryonic stem cells).
- *multipotent*, can differentiate into diverse but closely related cell types, which constitute an entire tissue (eg. haematopoietic stem cells).
- *oligopotent*, can develop into two or more lineages within a tissue (eg. a neural stem cell that can create a subset of neurons in the brain).
- *unipotent*, can form only a single lineage but still are characterized by self-renewal, thus they are fundamentally different from non-stem cells (eg. spermatogonial stem cells, muscle stem cells).

1.1.1 Human embryonic stem cells

Human embryonic stem cells hESCs are pluripotent cells derived from *in-vitro* fertilized-spared human embryos, derived in 1998 by Thomson *et al.* [3, 4]. After the fertilization of the human oocyte, a rapid sequence of divisions of the zygote (*cleavage*) happens, thus producing a packed cluster of totipotent cells of the same size of the original zygote. Three days after fertilization, the *morula* state is reached and the outer cells start detaching from the inner cells, thus reshaping the morula as a hollow ball of cells. Between days 5 and 6 the *blastocyst* stage is reached and two primary elements are present:

- the *trofoblast* i.e. the external cell layer, surrounding the blastocyst cavity (*blastocoel*), whose development results in the placenta and other structures necessary for the *in-utero* development of the embryo;
- the *inner cell mass* which gives rise to the embryo itself. hESCs are harvested from the inner cell mass and their isolation results in the destruction of the embryo.

About 16 days after fertilization, the inner cell mass undergoes the *gastrulation* process, which leads to the formation of the 3 germ layers. Each germ layer is able to differentiate into a limited number of phenotypes:

- the *endoderm*, i.e. the internal layer, producing hepatic/pulmonary/vesical/... tissues;
- the *mesoderm*, i.e. the intermediate layer, producing osseus/muscular/cardiac/... tissues;
- the *ectoderm*, i.e. the external layer, producing dermal/nervous/... tissues

Since hESCs are cells from the inner cell mass (Fig. 1.1) they can differentiate into the tissues produced by the 3 germ layers and their pluripotency raised hope for future cellular therapies as well as discussion on the ethics of the usage of human embryos.

1.1.2 Human induced pluripotent stem cells

Human induced pluripotent stem cells hiPSCs are pluripotent cells derived by reprogramming the DNA of human somatic cells [5, 6]. This procedure was tested first by Takahashi *et al.* [7] on adult mouse fibroblasts and then it was performed on adult human dermal fibroblasts [5] producing hiPSCs. Four pluripotent genes were introduced in human fibroblasts by lentiviral vectors:

- Oct-3/4 is fundamental in maintaining pluripotency and it is one of the responsible of the embryonic stem cell differentiation potential [8];
- Sox2 is a transcription factor crucial for self-renewal and pluripotency of undifferentiated embryonic stem cells [9];
- Klf4 another factor required for embryonic stem cell pluripotency and self-renewal [10];
- c-Myc is a proto-oncogene which was demonstrated to be implicated in the generation of hiPSCs by Takahashi *et al.* [5, 7].

hiPSCs were also produced by Nagakawa *et al.* [11] removing c-Myc and by Thomson *et al.* [6] by using Lin28 and Nanog instead of c-Myc and Klf4. These new procedures were developed since in [12] it is shown that about 20% of mices

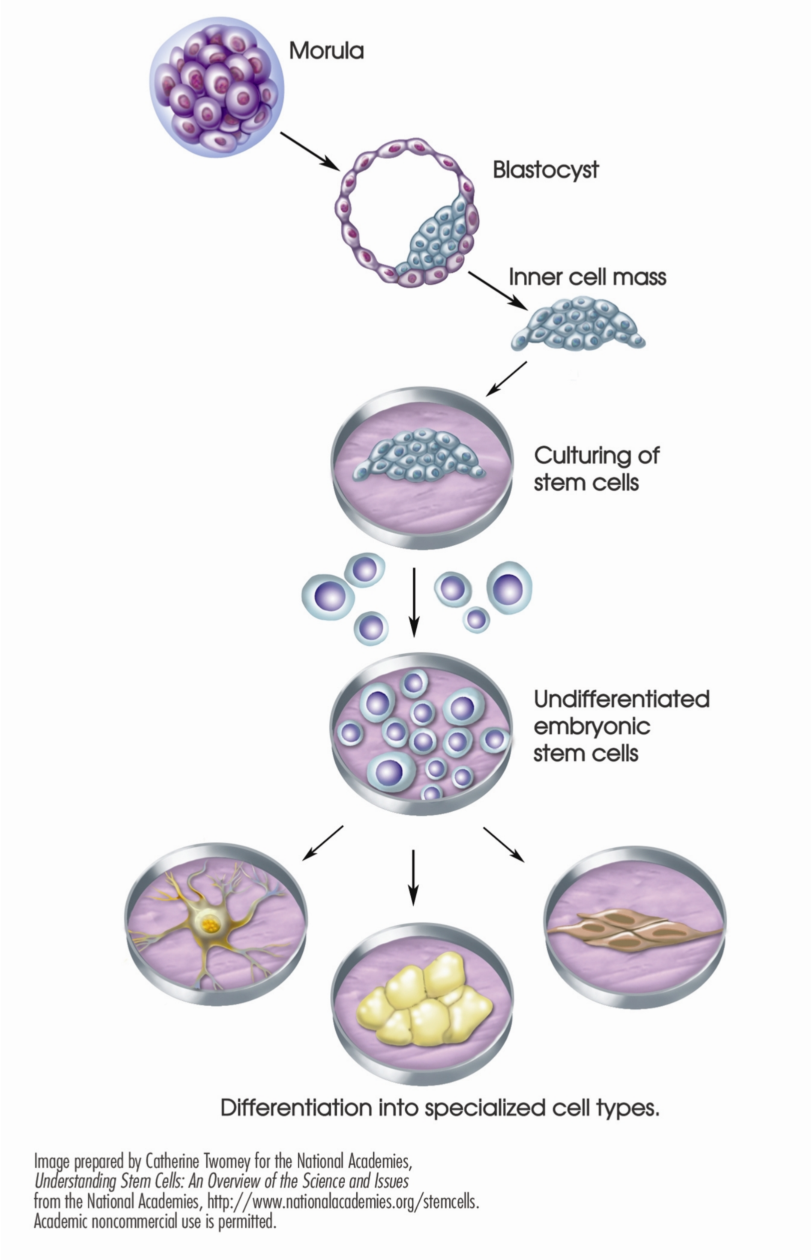

Image prepared by Catherine Twomey for the National Academies,
Understanding Stem Cells: An Overview of the Science and Issues
from the National Academies, http://www.nationalacademies.org/stemcells.
Academic noncommercial use is permitted.

Figure 1.1: Harvesting embryonic stem cells from a developing embryo.

generated by using induced pluripotent cells developed tumors imputable to the reactivation of c-Myc which was hypothesized acting as a reprogramming booster instead of a controller of pluripotency maintenance. In exchange, these new reprogamming procedures show lower efficiency than the original one: in [11] is reported that their procedure got 16 colonies out of the 3.5×10^5 reprogrammed cells while the original technique got 1000 colonies out of the 0.5×10^5 reprogrammed cells. Several tests were performed successfully on hiPSCs in terms of morphology, gene and protein expression, differentiation potency, etc. to assess the similarity of hiPSCs and hESCs. hiPSCs show some advantages than hESCs:

- no ethical issues, since no human embryos are used;
- patient-specific cells culturing is possible, since hiPSCs have the same genome as the person whose cells have been reprogrammed. It reduces the risk of rejection in the perspective of regenerative medicine;
- having patient-specific cells from diseased patient allows the production of specific disease models, as reported in [13–15].

1.1.3 Stem cell differentiation into cardiomyocytes

Since this first part of this Ph.D. thesis deals with the computational modelling of hESC-CMs and hiPSC-CMs, a summary of the best known differentiation methods of human pluripotent stem cells into CMs follows [16]. A family of methods consists in inducing the spontaneous differentiation of hESCs and hiPSCs towards the cardiac phenotype exploiting the formation of Embryoid Bodies (EBs), i.e. three-dimensional aggregates of pluripotent stem cells. Pluripotent stem cells are initially dissociated to small cell clusters and removed from the environment supporting their undifferentiated state, thus allowing the differentiation towards the 3 germ layers. Then cells are allowed to aggregate into EBs and after few days the EBs are plated on culture plates [17], thus making them proliferating in planar way. In [16] 3 main techniques are reported to promote the formation of EBs:

- aggregation of enzimatically dissociated cells cultured in suspension in the culture medium [18];
- the *hanging drops* methods, i.e. pipetting small drops of single cell suspension on the cover of a petri dish and inverting the cover on top of the dish,

thus letting the drops hanging due to the surface tension [19];

- the *forced aggregation* method, which simulates the hanging drops practice by making the cells aggregate by centrifugation [20].

About 1 day (24 -36 hours) after the EBs plating, spontaneously beating areas appear in the EBs: this is a macroscopic marker of the cardiac differentiation of the beating fraction of the EBs. In hESC differentiation the EB-based techniques were reported to have lower efficiency (8.1% of EBs spontaneously beat) than in murine stem cells differentiation (80-90% of EBs spontaneously beat) [21]. Another differentiation method, not involving the formation of EBs consists in culturing the pluripotent cells with mouse endodermal-like cells, which secrete differentiation inducing factors even if the specific factors themselves are not clearly known yet [22]. One more technique consists in inducing by growth factor the formation of mesodermal-like and endodermal-like cells since mesoderm is the germ layer originating the cardiac tissue and the endoderm is the source of the inducing signals [16]. All these differentiation methods are low efficiency processes as shown in [16], where differentiation tests on diverse hESC lines had efficiency oscillating between 2.9% - 9.4% for the cultures with mouse endodermal-like cells and between 1.6% - 12.5% for the EB method (efficiency measure reported as total number of beating areas / total number of cell aggregates). These data make the development of more efficient methods necessary, especially in the perspective of using hESC-CMs or hiPSC-CMs usable tools for pharmacological studies and for future cell therapies.

As stated in section 1.1.2, it is possible to produce hiPSC-CMs not only from healthy donors, but also from patients carrying particular genetic mutations, thus enabling the production if *in-vitro* models for the study of specific pathologies. Nowadays, many studies are focusing on the Long QT Syndrome (LQTS), a pathology delaying the heart repolarization (see section 1.2) and resulting in a prolonged QT interval in the ECG. The abnormal repolarization may lead to irregular heartbeats and evolve in syncope, faintness and finally in ventricular fibrillation [23]. Several gene mutations can induce the LQTS and some of them are currently under investigation by using hiPSC-CMs produced from LQTS-positive patients:

- in [15] hiPSC-CMs are used as *in-vitro* models for the most common type of LQTS, LQT1, which reduces the repolarizing slow delayed rectifier current

I_{Ks}, because of the mutation of the KCNQ1 gene encoding for the I_{Ks} channel;

- [13, 14] focus on the LQT2 syndrome which affects the KCNH2 gene encoding for the channel of the fast delayed rectifier current I_{Kr} and results in a smaller repolarizing current;

- in [24] they were able to produce LQT8 hiPSC-CMs carrying the mutation to the CACNA1C gene encoding for the depolarizing L-type Ca^{2+} current I_{CaL} channel, whose weakened voltage-inactivation is responsible for a sustained I_{CaL} [23].

One great advantage in using hiPSC-CMs is thus the opportunity for researchers of producing pools of cells carrying exactly the mutation / pathology to be investigated.

1.2 The cardiac action potential

The following section is a summary based on the detailed review by Walker *et al.* [25], reporting the basics about the cardiac AP and the ionic currents, pumps and mechanisms generating it. Finally some details about the hESC/hiPSC-CM APs are included. The cardiac muscle is a highly organized tissue, made of diverse cell types such as smooth muscle cells, fibroblasts and CMs. CMs represent the functional unit for the myocardial contraction and they are required to contract according to a precise scheme, in order to supply an appropriate pump action and blood perfusion. [26].

The cardiac tissue contraction is consequence of the excitation/contraction (EC) coupling: when a CM produces an AP, i.e. the membrane depolarization due to the ion transfer across the cell membrane itself, the intracellular Ca^{2+} concentration increases in response to the electrical excitation. The increased Ca^{2+} activates the myofilaments consequently initiating the crossbridge mechanism and finally resulting in the cell shortening (a more detailed description of this phenomenon will be provided at the end of this section). The myocardial contraction is the result of the coordinated activation and shortening of the single CMs throughout the heart. The AP assumes different shapes according to the location in the heart of the CM responsible of its firing (Fig. 1.2), but the most representative model to expose the AP genesis and the mechanisms involved is the ventricular AP, reported in Fig. 1.3.

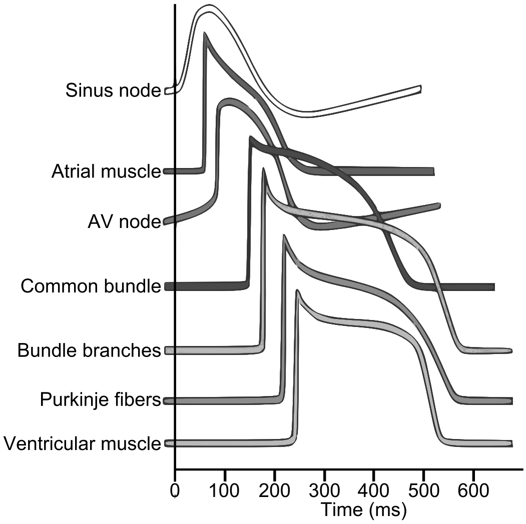

Figure 1.2: Illustrative representation of AP waveforms recorded in different regions of the human heart; displacement in time reflects the temporal sequence of propagation. Figure adapted from [27].

The four different phases of the AP are represented in Fig. 1.3 and each of them corresponds to the activation and the inactivation of specific ionic currents and pumps. During *Phase 4* the CM membrane potential is kept stable to its resting value (about -90 mV) by 4 mechanisms. Primarily the inward rectifier K^+ current (I_{K1}) allows an influx of K^+ ions, whose equilibrium potential mainly sets the CM membrane potential, since in *Phase 4* the cell membrane is basically permeable to K^+ only. The Na^+ /K^+ pump (I_{NaK}) is an ATP-dependent pump which moves 3 Na^+ into the extracellular space and 2 K^+ into the intracellular compartment, thus resulting into an outward current. I_{NaK} transports both Na^+ and K^+ against their concentration gradients by consuming ATP. The Na^+ /Ca^{2+} exchanger (I_{NaCa}) is a bidirectional transport which exchange 1 Ca^{2+} for 3 Na^+ exploiting both the concentration gradients of Na^+ and Ca^{2+} ; together with the sarcolemmal Ca^{2+} -ATPase (I_{pCa}) it contributes in balancing the intracellular Ca^{2+} and consequently in maintaining the resting potential.

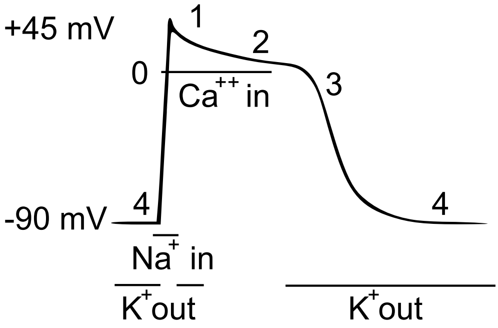

Figure 1.3: The 5 phases of the ventricular AP: (0) depolarization, (1) early (fast) repolarization, (2) plateau phase, (3) late (slow) phase of repolarization and (4) return to the resting membrane potential.

When the CM membrane potential reaches its voltage threshold (about -60 mV), it abruptly increases to about 40 - 50 mV and results in the upstroke, or *Phase 0*. The upstroke is generated by the Na^+ current (I_{Na}), a fast Na^+ influx along Na^+ concentration and electrical gradients. In *Phase 1* I_{Na} rapidly inactivates while the transient outward K^+ current (I_{to}) activates producing a transient efflux of K^+ along the electrochemical gradient: especially in ventricular cells, I_{to} induces the typical spike-and-dome shape. *Phase 2* is characterized by the AP plateau, sustained by the L-type Ca^{2+} current (I_{CaL}): this current activates during the upstroke but reaches its peak value during the plateau phase since I_{CaL} has slower dynamics than I_{Na}. I_{CaL} is also involved in the EC coupling. *Phase 3* represents the repolarization of the membrane potential and it is induced by the rapid delayed rectifier K^+ current (I_{Kr}) and the slow delayed rectifier K^+ current (I_{Ks}). At the end of *Phase 2*, first the rapid I_{Kr} channels and later the slower I_{Ks} channels open allowing the K^+ influx along the concentration gradient. In this phase the inward currents are inactivated and the delayed rectifier K^+ currents are responsible for the restoration of the resting potential [25].

Although this thesis is not dealing with the CM mechanics, it is worth to detail a bit more the EC coupling, i.e. how the electrical and the mechanical aspects are bounded and how the AP leads to the CM contraction. The elements involved in this phenomenon are the L-type Ca^{2+} channels, the T-tubules, the Sarcoplasmic Reticulum (SR) and the sarcomeres. T-tubules are invaginations of the cell membrane which make the L-type Ca^{2+} channels and the SR Ca^{2+} discharge system closer. The SR is an intracellular membrane network storing Ca^{2+} at high concentration (1.5 - 3 mM [28]) and regulating the cytosolic Ca^{2+} concentration. It contains two components fundamental for the Ca^{2+} homeostasis: the SERCA-2 and the Ca^{2+} release channels. The sarcomere represents the CM contractile unit, composed of thick and thin filaments made by myosin and actin respectively; in presence of high Ca^{2+} concentration this structure shortens its resting length (1.8 to 2.4 μm) by the crossbridge mechanism, allowing the cellular contraction [25].

During *Phase 0*, when the AP fires, the I_{CaL} channels open and Ca^{2+} flows into the CM. This small Ca^{2+} influx (trigger Ca^{2+}) is not sufficient to start the crossbridge mechanism, but it is enough to trigger the Ca^{2+} release from the SR through the SR Ca^{2+} release channels, which increases the cyosolic Ca^{2+} by about 100-fold. The cycle of crossbridge formation continues until Ca^{2+} is restored to its basal condition: this is mainly done by the ATP-dependent SERCA-2 pump, which moves the Ca^{2+} from the cytosol into the SR, where Ca^{2+} is buffered by the Ca^{2+} -binding protein calsequestrin. Moreover cytosolic Ca^{2+} is extruded into the extracellular space by I_{NaCa} and by I_{pCa}, which is activated by the complex formed by the binding of calmodulin to intracellular Ca^{2+} [25]. All these mechanisms make the intracellular Ca^{2+} concentration change, thus producing Ca^{2+} transients usually associated with APs.

1.2.1 Stem cell derived cardiomyocytes show different action potential shapes than adult myocytes

APs produced by hESC-CMs and hiPSC-CMs show some differences than adult APs, due to their immature or incomplete stage and the underway maturation process. The most evident diversities regards the *spontaneous APs* produced by hESC-CMs and hiPSC-CMs which in adult heart can be found in nodal cells only and some morphological features such as the more positive Maximum Diastolic Potential (MDP) or the smaller Maximum Upstroke Velocity (V_{max}) [29, 30]. Moreover as shown by their adult counterparts, hESC-CMs and hiPSC-CMs exhibit heterogenic AP shapes, usually classified as ventricular-like, atrial-like and nodal-like according to their resemblance to the respective adult phenotypes [13, 30] (Fig. 1.4). In [3] is shown that the expression of some ion channel genes and current intensity change during hESC-CM maturation (eg. increased I_{CaL}, I_{to}, I_{K1} and reduced funny current (I_f)), suggesting that they reach a more mature state with time in culture. These aspects will be deepened in chapters 2 and 3.

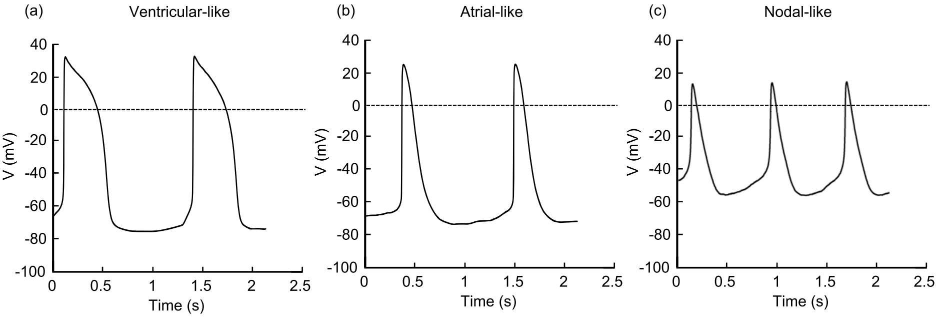

Figure 1.4: The hESC-CM and hiPSC-CM APs classes: (a) ventricular-like, (b) atrial-like and (c) nodal-like. All the panels refer to spontaneous APs. Experimental traces from [30].

1.3 The Hodgking & Huxley approach to the action potential modelling

In this final section a brief summary of the Hodgkin & Huxley formalism, we used in chapters 2 and 3, is reported. The Hodgkin & Huxley model is a mathematical model reproducing a neuronal AP, its initiation and its propagation [31]. Although the original Hodgkin & Huxley model deals just with one cellular species, it created a well assessed formalism to describe the AP, applied also to the cardiac AP [32–36]. The AP expression as function of time ($V_m(t)$) is obtained by integrating the fundamental equation

$$\frac{dV_m}{dt} = -\frac{I_{ion}}{C_m} \tag{1.1}$$

where C_m represents the membrane capacitance and I_{ion} the sum of all the ionic currents. The generic ionic current flowing through the membrane is represented as

$$I = x^a \cdot y^b \cdot G_{max} \cdot (V_m - E_r) \tag{1.2}$$

where $x(t, V_m)$ and $y(t, V_m)$ represent the activation and inactivation gating variables respectively, G_{max} is the maximum conductance and E_r the resting potential for the specific ionic specie computed as the Nernst potential

$$E_r = \frac{RT}{zF} \cdot ln\frac{[ion]_o}{[ion]_i} \tag{1.3}$$

The generic gating variable $x(V_m, t)$ can be expressed in 2 equivalent forms (Eqs. 1.4 and 1.7). The first formulation

$$\frac{dx}{dt} = \alpha_x(1 - x) - \beta_x x \tag{1.4}$$

highlights the meaning of x and $1-x$ as the fractions of open and closed channels respectively, in order to reproduce the transitions from the closed state to the open state and vice-versa. If the values of either α_x or β_x depend on V_m, then the state of the gate is voltage-dependent as well as time-dependent. By imposing

$$\alpha_x = \frac{x_\infty}{\tau_x} \tag{1.5}$$

and

$$\beta_x = \frac{1 - x_\infty}{\tau_x} \tag{1.6}$$

equation 1.4 can be reformulated as

$$\frac{dx}{dt} = \frac{x_\infty - x}{\tau_x} \tag{1.7}$$

in order to highlight the dynamic sense of the gating variable $x(V_m, t)$. The steady-state

$$x_\infty = \frac{\alpha_x}{\alpha_x + \beta_x} \tag{1.8}$$

represents the value to which x tends at a certain voltage and it is usually obtained by fitting the experimental data using a sigmoid function

$$x_\infty = \frac{1}{1 + e^{\frac{V_m - V_h}{K}}} \tag{1.9}$$

where V_h is the voltage of half activation and K is the gradient of activation. Figure 1.5 shows how the steady-state gating variable is sensitive to V_h and K. The time constant

$$\tau_x = \frac{1}{\alpha_x + \beta_x} \tag{1.10}$$

means how fast the gating variable x reaches its steady state x_∞.

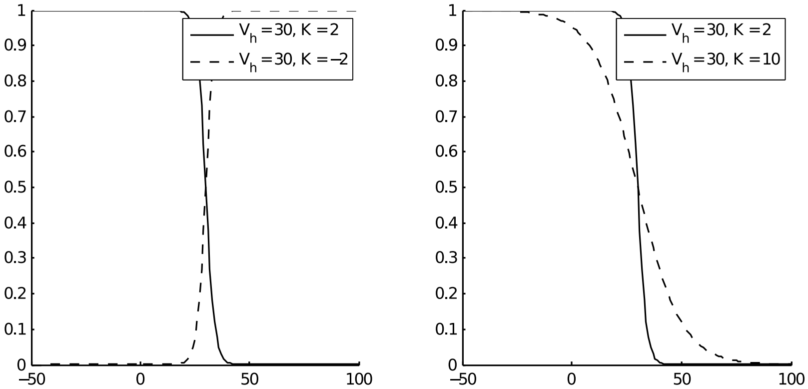

Figure 1.5: Illustrative examples of a generic steady-state gating variable with diverse values of the voltage of half activation V_h and the gradient of activation K.

Bibliography

[1] Smith A. A glossary for stem-cell biology. Nature 2006;441(7097):1060.

[2] Schöler RH. The Potential of Stem Cells: An Inventory. In Knoepffler N, Schipanski D, Sorgner SL (eds.), Humanbiotechnology as Social Challenge. Ashgate Publishing, Ltd., 2007; 28.

[3] Sartiani L, Bettiol E, Stillitano F, Mugelli A, Cerbai E, Jaconi ME. Developmental changes in cardiomyocytes differentiated from human embryonic stem cells: a molecular and electrophysiological approach. Stem Cells 2007; 25(5):1136–1144.

[4] Thomson JA. Embryonic Stem Cell Lines Derived from Human Blastocysts. Science 1998;282:1145–1147.

[5] Takahashi K, Tanabe K, Ohnuki M, Narita M, Ichisaka T, Tomoda K, Yamanaka S. Induction of pluripotent stem cells from adult human fibroblasts by defined factors. Cell November 2007;131(5):861–872.

[6] Yu J, Vodyanik MA, Smuga-Otto K, Antosiewicz-Bourget J, Frane JL, Tian S, Nie J, Jonsdottir GA, Ruotti V, Stewart R, Slukvin II, Thomson JA. Induced Pluripotent Stem Cell Lines Derived from Human Somatic Cells. Science 2007;318(5858):1917–1920.

[7] Takahashi K, Yamanaka S. Induction of Pluripotent Stem Cells from Mouse Embryonic and Adult Fibroblast Cultures by Defined Factors. Cell August 2006;126(4):663–676. ISSN 00928674.

[8] Niwa H, Miyazaki J, Smith aG. Quantitative expression of Oct-3/4 defines differentiation, dedifferentiation or self-renewal of ES cells. Nature genetics April 2000;24(4):372–376. ISSN 1061-4036.

[9] Fong H, Hohenstein Ka, Donovan PJ. Regulation of self-renewal and pluripotency by Sox2 in human embryonic stem cells. Stem Cells August 2008; 26(8):1931–1938. ISSN 1549-4918.

[10] Zhang P, Andrianakos R, Yang Y, Liu C, Lu W. Kruppel-like factor 4 (Klf4) prevents embryonic stem (ES) cell differentiation by regulating Nanog gene expression. The Journal of biological chemistry March 2010;285(12):9180–9189. ISSN 1083-351X.

[11] Nakagawa M, Koyanagi M, Tanabe K, Takahashi K, Ichisaka T, Aoi T, Okita K, Mochiduki Y, Takizawa N, Yamanaka S. Generation of induced pluripotent stem cells without Myc from mouse and human fibroblasts. Nature biotechnology January 2008;26(1):101–106. ISSN 1546-1696.

[12] Okita K, Ichisaka T, Yamanaka S. Generation of germline-competent induced pluripotent stem cells. Nature July 2007;448(7151):313–7. ISSN 1476-4687.

[13] Lahti AL, Kujala VJ, Chapman H, Koivisto AP, Pekkanen-Mattila M, Kerkela E, Hyttinen J, Kontula K, Swan H, Conklin BR, Yamanaka S, Silvennoinen O, Aalto-Setala K. Model for long QT syndrome type 2 using human iPS cells demonstrates arrhythmogenic characteristics in cell culture. Dis Model Mech November 2011;5(2):220–230. ISSN 1754-8403.

[14] Matsa E, Rajamohan D, Dick E, Young L, Mellor I, Staniforth A, Denning C. Drug evaluation in cardiomyocytes derived from human induced pluripotent

stem cells carrying a long QT syndrome type 2 mutation. Eur Heart J April 2011;32(8):952–962.

[15] Moretti A, Bellin M, Welling A, Jung CB, Lam JT, Bott-Flügel L, Dorn T, Goedel A, Höhnke C, Hofmann F, Seyfarth M, Sinnecker D, Schömig A, Laugwitz KL. Patient-specific induced pluripotent stem-cell models for long-QT syndrome. N Engl J Med 2010;363(15):1397–1409.

[16] Pekkanen-Mattila M. Cardiomyocyte Differentiation from Human Pluripotent Stem Cells. Tampere: Tampere University Press, 2010. ISBN 978-951-44-8234-2.

[17] Kurosawa H. Methods for inducing embryoid body formation: in vitro differentiation system of embryonic stem cells. Journal of bioscience and bioengineering May 2007;103(5):389–398. ISSN 1389-1723.

[18] Doetschman TC, Eistetter H, Katz M, Schmidt W, Kemler R. The in vitro development of blastocyst-derived embryonic stem cell lines: formation of visceral yolk sac, blood islands and myocardium. Journal of embryology and experimental morphology June 1985;87:27–45. ISSN 0022-0752.

[19] Takahashi T, Lord B, Schulze PC, Fryer RM, Sarang SS, Gullans SR, Lee RT. Ascorbic acid enhances differentiation of embryonic stem cells into cardiac myocytes. Circulation April 2003;107(14):1912–1916. ISSN 1524-4539.

[20] Ng ES, Davis RP, Azzola L, Stanley EG, Elefanty AG. Forced aggregation of defined numbers of human embryonic stem cells into embryoid bodies fosters robust, reproducible hematopoietic differentiation. Blood September 2005; 106(5):1601–3. ISSN 0006-4971.

[21] Kehat I, Kenyagin-karsenti D, Snir M, Segev H, Amit M, Gepstein A, Livne E, Binah O, Itskovitz-eldor J, Gepstein L. Human embryonic stem cells can differentiate into myocytes with structural and functional properties of cardiomyocytes. The Journal of clinical investigation 2001;108(3):407–414.

[22] Mummery C, Ward-van Oostwaard D, Doevendans P, Spijker R, van den Brink S, Hassink R, van der Heyden M, Opthof T, Pera M, de la Riviere AB, Passier R, Tertoolen L. Differentiation of human embryonic stem cells to cardiomyocytes: role of coculture with visceral endoderm-like cells. Circulation June 2003;107(21):2733–2740. ISSN 1524-4539.

[23] Morita H, Wu J, Zipes DP. The qt syndromes: long and short. The Lancet 2008;372(9640):750 – 763. ISSN 0140-6736.

[24] Yazawa M, Hsueh B, Jia X, Pasca AM, Bernstein JA, Hallmayer J, Dolmetsch RE. Using induced pluripotent stem cells to investigate cardiac phenotypes in Timothy syndrome. Nature March 2011;471(7337):230–234.

[25] Walker CA, Spinale F. The structure and function of the cardiac myocyte: a review of fundamental concepts. The Journal of Thoracic and Cardiovascular Surgery 1999;118(2):375–382.

[26] Woodcock Ea, Matkovich SJ. Cardiomyocytes structure, function and associated pathologies. The international journal of biochemistry cell biology September 2005;37(9):1746–1751. ISSN 1357-2725.

[27] Malmivuo J, Plonsey R. Bioelectromagnetism - Principles and Applications of Bioelectric and Biomagnetic Fields. Oxford University Press, New York, 1995. ISBN 978-019-505-823-9.

[28] Bers DM. Excitation-Contraction Coupling and Cardiac Contractile Force. 2nd edition. Kluwer Academic Press; Dordrecht, Netherlands, 2001.

[29] Bettiol E, Sartiani L, Chicha L, Krause KH, Cerbai E, Jaconi ME. Fetal bovine serum enables cardiac differentiation of human embryonic stem cells. Differentiation research in biological diversity October 2007;75(8):669–81. ISSN 0301-4681.

[30] Ma J, Guo L, Fiene S, Anson B, Thomson J, Kamp T, Kolaja K, Swanson B, January C. High purity human-induced pluripotent stem cell-derived cardiomyocytes: electrophysiological properties of action potentials and ionic currents. Am J Physiol Heart Circ Physiol November 2011;301(5):H2006–H2017.

[31] Hodgkin A, Huxley A. A quantitative description of membrane current and its application to conduction and excitation in nerve. J Physiol Lond 1952; 117(4):500–544.

[32] Pandit SV, Clark RB, Giles WR, Demir SS. A mathematical model of action potential heterogeneity in adult rat left ventricular myocytes. Biophysical journal December 2001;81(6):3029–51. ISSN 0006-3495.

[33] Priebe L, Beuckelmann DJ. Simulation Study of Cellular Electric Properties in Heart Failure. Circulation Research June 1998;82(11):1206–1223. ISSN 0009-7330.

[34] Shannon T, Wang F, Puglisi J, Weber C, Bers DM. A mathematical treatment of integrated Ca dynamics within the ventricular myocyte. Biophys J November 2004;87(5):3351–3371. ISSN 0006-3495.

[35] Bondarenko VE, Szigeti GP, Bett GCL, Kim SJ, Rasmusson RL. Computer model of action potential of mouse ventricular myocytes. American journal of physiology Heart and circulatory physiology September 2004;287(3):H1378–403. ISSN 0363-6135.

[36] ten Tusscher KHWJ, Noble D, Noble PJ, Panfilov AV. A model for human ventricular tissue. Am J Physiol Heart Circ Physiol April 2004; 286(4):H1573–1589.

CHAPTER

TWO

MATHEMATICAL MODELLING OF THE ACTION POTENTIAL OF HUMAN EMBRYONIC STEM CELL DERIVED CARDIOMYOCYTES

Michelangelo Paci[1]*, Laura Sartiani[2]*, Martina Del Lungo[2], Marisa Jaconi[3], Alessandro Mugelli[2], Elisabetta Cerbai[2]**, Stefano Severi[1]**

[1] *Biomedical Engineering Laboratory – D.E.I.S., University of Bologna, Via Venezia 52, 47521 Cesena, Italy*

[2] *Center of Molecular Medicine (C.I.M.M.B.A.), University of Firenze, Viale Pieraccini 6, 50139 Firenze, Italy*

[3] *Department of Pathology and Immunology, University of Geneva, Rue Michel-Servet 1, 1211 Geneva 4, Switzerland*

*, ** *equal contribution*

The content of this chapter was published in *Biomedical Engineering OnLine* 2012:11-61.

Abstract

Background
Human embryonic stem cell-derived cardiomyocytes (hESC-CMs) hold high potential for basic and applied cardiovascular research. The development of a reliable simulation platform able to mimic the functional properties of hESC-CMs would be of considerable value to perform preliminary test complementing in vitro experimentations.
Methods
We developed the first computational model of hESC-CM AP by integrating our original electrophysiological recordings of transient-outward, funny, and sodium-calcium exchanger currents and data derived from literature on sodium, calcium and potassium currents in hESC-CMs.
Results
The model is able to reproduce basal electrophysiological properties of hESC-CMs at 15-40 days of differentiation (Early stage). Moreover, the model reproduces the modifications occurring through the transition from Early to Late developmental stage (50-110, days of differentiation). After simulated blockade of ionic channels and pumps of the sarcoplasmic reticulum, Ca^{2+} transient amplitude was decreased by 12% and 33% in Early and Late stage, respectively, suggesting a growing contribution of a functional reticulum during maturation. Finally, as a proof of concept, we tested the effects induced by prototypical channel blockers, namely E4031 and nickel, and their qualitative reproduction by the model.
Conclusions
This study provides a novel modelling tool that may serve useful to investigate physiological properties of hESC-CMs.

Keywords

Embryonic Stem Cells, Computer Simulation, Action Potential, Pharmacology.

2.1 Background

Human embryonic stem cell-derived cardiomyocytes (hESC-CMs) are pluripotent cells derived from the blastocyst stadium of human embryos, having the potential to differentiate in all the three embryonic germ layers [1]. Many studies have been carried out to identify the most advantageous strategies to drive the differentiation towards the desired cell phenotypes thus allowing valuable investigations in basic research and suggesting useful perspectives for regenerative purposes. In the cardiovascular field, hESCs provide a powerful tool to clarify key developmental steps of cardiac embryogenesis [2], to develop reliable in vitro models for drug toxicity screening [3] and are considered a promising source for cell-based therapies in pathologies such as myocardial infarction or pace-maker center dysfunction [4]. Studies involving hESCs differentiated toward the cardiac phenotype are rather demanding due to difficulties such as i) low efficiency process of differentiation [5]; ii) dishomogeneity of cell phenotypes; iii) laborious phenotypic characterization, e.g. via patch-clamp or multicellular and multi-electrode array recordings [6–8]. Another complication arises from the observation that hESCs, like fetal CMs, are electrophysiologically immature [6]; their properties evolve during in vitro culturing [6], a phenomenon which appears to be regulated by interactions with non-cardiomyocytes in embryoid bodies (EBs) [9].

To date extensive information is available mostly as unsystematic mass of basic electrophysiological properties of different hESC lines differentiated toward the cardiac lineage and on the modifications occurring during maturation or upon exposure to different drugs or chemicals. Nonetheless, no attempt was done to systematize current knowledge to fully evaluate the impact of individual key ionic currents and of excitation-contraction coupling mechanisms on basic physiology in hESC-CMs [10–13].

Computational modelling represents a consolidated approach in cardiac research to simulate the electrophysiology of single cell or cell-made tissue [14] and the modifications induced by chemicals and drugs. This approach usually complements *in-vitro* and *in-vivo* experimentation to create a compelling tool able to predict physiological responses, abnormal reactions to drug application and to formulate new hypotheses.

The aim of this work is to develop a computational model of AP of H1-hESC-CMs allowing to follow the maturation process. Due to the shortage of measurements, especially at advanced developmental stages, this model can help to infer developmental mechanisms not obvious from the bare measurements.

Data on membrane ionic currents for this cell line coming from our original measurements of transient outward potassium, funny, sodium-calcium exchanger currents, and data from literature on sodium, calcium and potassium currents in hESC-CMs were integrated into the model. To take into account the presence of non-cardiac cells in intact EBs, a further model assessment is proposed by coupling the hESC-CM model with modelled fibroblasts and evaluating their impact on the AP. The formulated model simulates i) the main basic AP features and ii) the developmental changes documented during in vitro maturation.

2.2 Methods

Methods for hESC-CM culture, differentiation and electrophysiological recording are described in Supplementary Methods on page 163. hESC-CM were included in the Early or Late group according to differentiation time, i.e. from 15-40 and 50-110 days, respectively [6].

2.2.1 The hESC-CM AP model and its transition from Early to Late stage of development

The starting point in developing the hESC-CM model was a modified version [15] of the TenTusscher model of human adult ventricular CM [16], this parent model was then largely modified by changing the formulation of almost all the currents to incorporate all the available data on hESC-CMs and by adding two currents ($\mathrm{I_f}$ and $\mathrm{I_{CaT}}$) that are not present in the adult ventricle. Following the classical Hodgkin-Huxley formulation [17], the cell electrophysiological behaviour is described by Eq. 2.1:

$$\frac{dV}{dt} = -\frac{I_{ion}}{C_m}, \tag{2.1}$$

where V is the membrane potential, C_m the membrane capacitance and I_{ion} the sum of all the membrane currents. Details on each current are in the following subsections.

Properties of ion currents based on our recordings or derived from literature data on hESC-CMs were integrated into the model to reproduce Early and Late hESC-CM APs. Where data from hESC-CMs were not available, observations in ESC-derived or embryonic CMs from different species were considered. Although ionic channels undergo complex regulation at a transcript level, the I/V relationship of most currents does not change among different developmental stages [18–22]. Hence, we assumed that developmental changes in each current, $\mathrm{I_{xx}}$, are determined mainly by its quantitative change, which can be represented by setting a variable fraction (ratio, $\mathrm{RaI_{xx}}$) of the current maximal conductance in the adult model. Table 2.1 summarizes the maximal conductance values for the main currents in the model.

2.2.2 Sodium current (I_{Na})

Our I_{Na} formulation slightly changes the original adult model (Eqs. S3, S6 and S8, in Supplementary Methods on page 163). The steady-state inactivation was changed according to Satin et al. data on inactivation dynamics of H9.2-hESC-CMs at the Early stage of differentiation (Fig. 2.1a) [27].
As also reported in [23] for rodent ESC-CMs we considered a small expression of I_{Na} at the Early stage and full expression at the Late one; the expression at the Early stage was further reduced with respect to [23] (from 0.08 to 0.038) in order to fit properly our experimental V_{max} and the Action Potential Duration (APD).
$RaI_{Na} = 0.038$ (Early); $RaI_{Na} = 1$ (Late)

2.2.3 L-type calcium current (I_{CaL})

Due to lack of specific data on I_{CaL} at the Early stage, we tuned the permeability, the Ca^{2+} dependent inactivation gate, f_{Ca} (Eqs. S25-S31), the time constant of the voltage dependent inactivation gate, τ_f (Eq. S33), and the steady-state activation gate, d_{inf} (Eq. S19) to reproduce the experimental features of AP, in particular APD.
We then slightly modified d_{inf} in order to fit our experimental recordings of I_{CaL} at Late developmental stage (Fig. 2.1b, Late stage, n=1), whereas inactivation parameters became equal to those of adult CMs in the Late stage formulation. We maintained the ratio between Late and Early conductances proposed in [23] based on data in mice and guinea pigs:
$RaI_{CaL}= 0.25$ (Early); $RaI_{CaL} = 0.422$ (Late)

2.2.4 T-type calcium current (I_{CaT})

At variance with the adult model, we included I_{CaT}, on the basis of different experimental evidence. First, I_{CaT} was reported to be highly expressed during fetal heart development and gradually decline after birth, becoming restricted to the conduction and pacemaker cells [28]. Secondly, I_{CaT} is functionally expressed

Table 2.1: Main developmental changes of ionic currents. Maximum conductances, currents and fluxes for Early and Late human embryonic stem cell-derived and adult ventricular cardiomyocyte models. The species considered for the Early and Late date are reported. Adult data refers to the TenTusscher model [16]. †new measurements and data; §values chosen to reproduce at best the AP shape; * not only the maximal conductance/current was changed but also the current formulation (see Supplementary Methods on page 163). EXP: experimental data; MOD: used for modelling.

	Parameter (units)	Early	Late	Adult [16]	Species [Ref.]
I_{to}	G_{to} (S/F) max conductance	19.2929	48.702	294	human, EXP, †; human, MOD, [16]
I_{Kr}	G_{Kr} (S/F) max conductance	288.0	134.4	96	rat, guinea pig, EXP, [23] human, MOD, [16]
I_f*	G_f (S/F) max conductance	49	20.913	-	human, EXP, [6]
I_{K1}*	G_{K1} (S/F) max conductance	240.523	1154.508	5405	human, EXP, [6] human, MOD, [16]
I_{CaL}*	G_{CaL} ($dm^3/(F{\cdot}s)$) permeability	0.0438	0.0739	0.175	mouse, EXP, [23] human, EXP. [6] human, MOD, [16]
I_{CaT}	G_{CaT} (S/F) max conductance	45.8	9.16	-	human, EXP, † rabbit, MOD, [24]
I_{NaCa}*	$I_{maxNaCa}$ (A/F) max current	17500	18240	1000	human, EXP, † human, MOD, [16]
I_{Na}	G_{Na} (S/F) max conductance	563.844	14838	14838	mouse, EXP, [23] human, MOD, [16]
I_{Ks}	G_{Ks} (S/F) max conductance	15.7	15.7	157	human, EXP, [25] human, MOD, [16]
I_{NaK}	I_{maxNaK} (A/F) max current	0.9534	1.1305	1.362	mouse, EXP, [26] human, MOD, [16]
I_{pCa}	G_{pCa} (S/F) max conductance	0.825, §	0.825, §	25	human, MOD, [16]
I_{up}	I_{maxUp} (mM/s) max flux	0.0565	0.1403	0.425	mouse, EXP, [23] human, MOD, [16]
I_{rel}	I_{maxRel} (mM/s) max flux	0.274	9.88	24.7	mouse, EXP, [23] human, MOD, [16]
I_{leak}	$I_{maxLeak}$ (1/s) max rate	0.0004	0.024	0.08	mouse, EXP, [23] human, MOD, [16]
I_{bCa}	G_{bCa} (S/F) max conductance	0.118, §	0.592, §	0.592	human, MOD, [16]

in mouse ESC and is downregulated during cardiac differentiation: I_{CaT} channel subunits Cav3.1 and Cav3.2 expression decreased to approximately 46% and 24%, respectively, at 23.5 days of differentiation with respect to 9.5 days [29]. Finally, our qualitative RT-PCR measurements in H1-hESC-CMs show a clear expression of Cav3.1 and Cav3.2 at both stages (Fig. 2.1c). We used the I_{CaT} formulation proposed in [24] in their sinoatrial node cell model, with progressively decreasing scaling factors for the maximal conductance:

RaI_{CaT}= 0.25 (Early); RaI_{CaT} = 0.05 (Late)

2.2.5 Transient outward (I_{to}), rapid and slow delayed rectifier (I_{Kr}, I_{Ks}) K^+ currents

I_{to} properties were based on original data obtained in H1-hESC-CMs. Fig. 2.1d shows the I/V relationship for peak K^+currents evoked by depolarizing steps in Early and Late CMs (median data and interquartile, n=10 Early stage and n=9 Late stage). A 10 mV positive shift was applied to experimental data to account for the use of Cd^{2+} to block I_{CaL}, as done by [30]. According to our previous observations [6], I_{to} activation properties are similar to those described in native cardiac cells. Maximum conductances and steady-state activation were calculated by fitting experimental data (Fig. 2.1d and Eq. S43):

RaI_{to}= 0.065622 (Early); RaI_{to} = 0.165653 (Late)

In accordance with various in vivo and in vitro experimental data in fetal guinea pigs [20], rats [31, 32], and mice [33], I_{Kr} maximal conductance was greater than in the adult CMs and it decreased during maturation, we chose the specific expression ratios in order to mimick MDP and the APD at the different developmental stages:

RaI_{Kr}= 3 (Early); RaI_{Kr} = 1.4 (Late)

I_{Ks} conductance in the Early developmental stage was set in order to achieve a good fitting of the I/V curve (Fig. S1) obtained by [25] on Early hESC-CMs. On the basis of data on embryonic murine heart [19, 23], where Early and Late developmental stages seem to share the same I_{Ks} conductance, a single value of $\mathrm{RaI}_{\mathrm{Ks}}$ was used:

RaI_{Ks} = 0.1 (Early and Late);

2.2.6 Inward rectifier K^+ current (I_{K1})

In hESC-CMs I_{K1} is very small but not absent at the Early stage, then it increases during the development, as also reported for rat and guinea pig [23]. Conductances were identified according to our previous data [6], showing a ratio between Late and Early current density at -90 mV of 5.42. In order to reduce the MDP we set in our model a ratio of 4.8, within the variability of our data and introduced a shift of the voltage dependence for the inward rectification factor, $x_{k1\,\mathrm{inf}}$ (Eqs. S67-S69), without modifying the current reversal potential.
RaI$_{K1}$= 0.0445 (Early); *RaI$_{K1}$* = 0.2136 (Late)

2.2.7 Funny current (I_f)

A key step of the formulation of a specific hESC-CM model consisted in integrating the hyperpolarization-activated cyclic nucleotide-gated or funny current, that is reported to be one of the main contributor for the spontaneous beating of pacemaker cells [34] and hESC-CMs [6]. I_f formulation (Eqs. S71-S73) and conductance were obtained by fitting recordings performed on Early H1-hESC-CMs (Fig. 2.1e, Early stage, n=4). For the Late stage, in accordance to our previous data [6], we assumed that current density decreased over maturation to an extent equal to the drop of cumulative HCN transcript expression (Fig. 2.1e, inner panel): the estimated ratio between Early and Late stage was 2.34.
RaI= 0.5389 (Early); *RaI$_f$*= 0.23 (Late)

2.2.8 Sodium-potassium pump (I_{NaK}) and sodium-calcium exchanger (I_{NaCa})

Since data on hESC-CM I_{NaK} were not available, maximal current density was set taking into account its influence on the *diastolic depolarization rate* (DDR) and *frequency of spontaneous beating* (F) and reflecting the maturation related growth of I_{NaK} expression according to experiments by [26] on mouse ESC-CMs:
RaI$_{NaK}$ = 0.7 (Early); *RaI$_{NaK}$* = 0.83 (Late)
As far as I_{NaCa} is concerned, we used original experimental data from H1-hESC-CMs. Voltage ramp (from 120 to +50 mV) protocols elicited an almost linear I_{NaCa} I/V relationship (Fig. 2.1f, n= 6) that showed an inward and outward mode at both developmental stages. Fitting of experimental data led to modify the original maximal current density and the extra factor α in the I_{NaCa} expression [16]:

RaI_{NaCa} = 17.50 (Early); RaI_{NaCa} = 18.24 (Late)
α=0.8 (Early), α=0.38 (Late)

2.2.9 SR currents

The maximal values for the uptake ($\mathrm{I_{up}}$), release ($\mathrm{I_{rel}}$) and leakage ($\mathrm{I_{leak}}$) currents were tuned to simulate the ryanodine induced reduction of $\mathrm{Ca^{2+}}$ transient amplitude reported in [11] at the Early and in [12] at the Late stage. Increases in maximal current densities at the Late stage were based on the rodent ESC-CM model [23].
RaI_{Up} = 0.133 (Early); RaI_{Up} = 0.33 (Late)
RaI_{Rel} = 0.0111 (Early); RaI_{Rel} = 0.4 (Late)
RaI_{leak} = 0.005556 (Early); RaI_{leak} = 0.3 (Late)

2.2.10 Sarcolemmal calcium pump, $\mathbf{I_{pCa}}$, and background current, $\mathbf{I_{bCa}}$

Since data about these currents are not available, we chose the following values to reproduce at best the AP shape:
RaI_{Cap}=0.033 (Early and Late);
RaI_{bCa}=0.2 (Early); RaI_{bCa}=1 (Late);

2.2.11 Cell capacitance and dimensions

Median values of measured cell membrane capacitance were used to set cell dimensions (see Supplementary Methods on page 163).

2.2.12 Sensitivity analysis

A sensitivity analysis was performed according to the procedure reported in [35, 36], opportunely adapted to our model. The main differences with respect to [35] are: (i) our hESC-CM model is not stimulated by an external source and (ii) we concentrate our analysis on the impact of the ratios RaI_{xx} on the AP shape. One ratio was varied at time by -20%, -10%, +10% and +20% respectively.
Considering the following ratios (parametrs) “p”
p={$\mathrm{RaI_{Na}}$, $\mathrm{RaI_{CaL}}$, $\mathrm{RaI_{f}}$, $\mathrm{RaI_{to}}$, $\mathrm{RaI_{K1}}$, $\mathrm{RaI_{Kr}}$, $\mathrm{RaI_{Ks}}$, $\mathrm{RaI_{NaK}}$, $\mathrm{RaI_{NaCa}}$}
and the AP features (characteristics) “c”

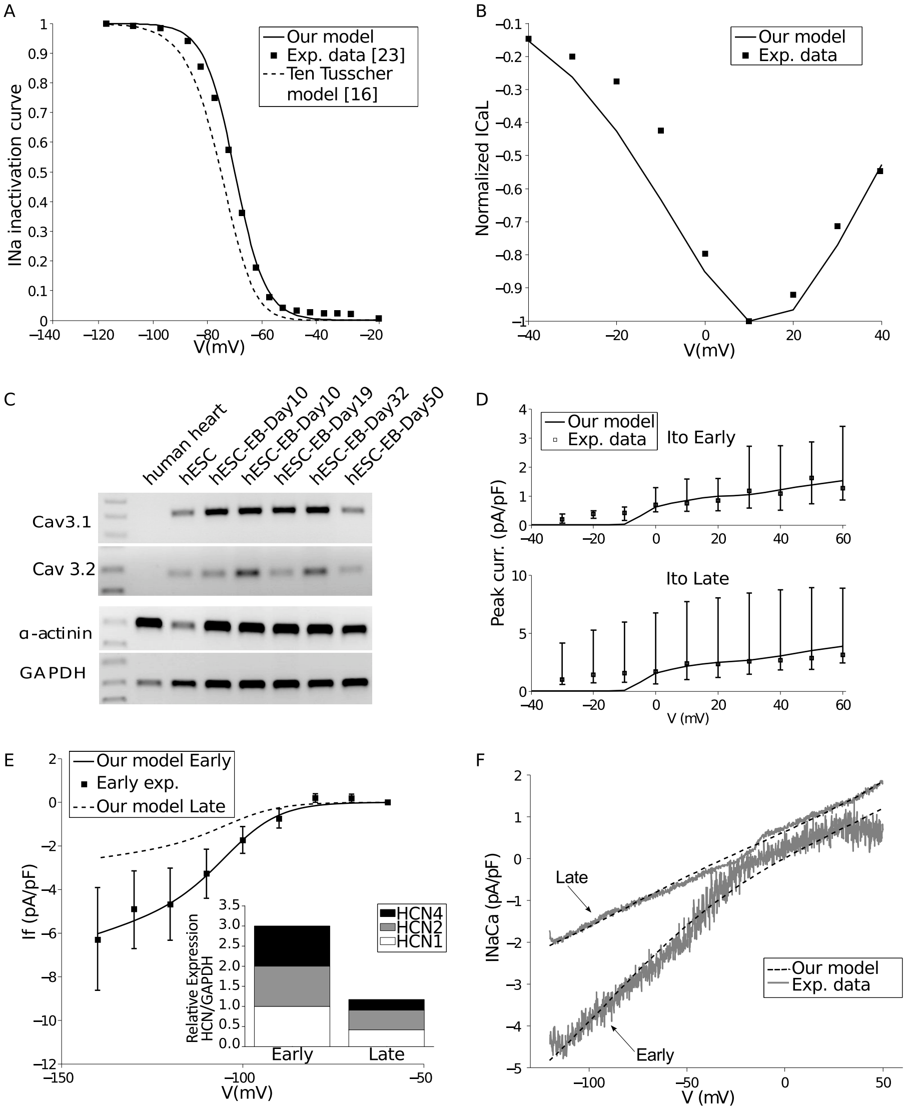

Figure 2.1: Currents: experimental data and model fitting. (a) I_{Na} inactivation for Early hESC-CMs. (b) I_{CaL} normalized current-voltage (I/V) curve (Late stage). (c) Cav3.1, Cav3.2 and GADPH expression (I_{CaT}) for H1-hESC-CMs. (d) I_{to} I/V curves. (e) I_f I/V curves and HCN quantitative expression (inset). (f) I_{NaCa} elicited by a voltage ramp protocol.

c={MDP, $V_{\max}$, APD_{30}, APD_{50}, APD_{70}, APD_{90} , DDR, F},
computed after 300 seconds of simulation (assuming the steady state condition) the indexes percentage of change ($D_{c,p,a}$), sensitivities ($S_{c,p,+20\%}$and $S_{c,p,-20\%}$) and relative sensitivities ($r_{c,p,+20\%}$ and $r_{c,p,-20\%}$) were calculated as follows:

$$D_{c,p,a} = \frac{(C_{p,a} + C_{control})}{C_{control}} \cdot 100 \tag{2.2}$$

$$S_{c,p,+20\%} = \frac{D_{c,p,+20\%}}{0.2}, S_{c,p,-20\%} = -\frac{D_{c,p,-20\%}}{0.2} \tag{2.3}$$

$$r_{c,p,+20\%} = \frac{S_{c,p,+20\%}}{\left|S_{c,p,+20\%}\right|_{\max,c}}, r_{c,p,-20\%} = \frac{S_{c,p,-20\%}}{\left|S_{c,p,-20\%}\right|_{\max,c}} \tag{2.4}$$

Splitting the original $S_{c,p}$ and $r_{c,p}$ [35] was necessary since several tests resulted in no spontaneous APs, thus making impossible calculating the AP features and all their $D_{c,p,a}$. However, for each ratio at least one $D_{c,p,a}$ ($D_{c,p,+20\% or}D_{c,p,-20\%}$) was available thus allowing to get the asymmetrical sensitivities.

2.2.13 Interaction with *in-silico* fibroblasts

In order to preserve intracellular milieu and cell-to-cell communication, AP recordings were not performed on single cells but on EBs, aggregates containing different cell phenotypes among which hESC-CMs and fibroblasts. To test the interaction between these kinds of cells and assess the effect on AP simulation, an additional mammalian fibroblast model, resistively coupled to the hESC-CM, was developed according to [37–39]. To this aim, the hESC-CM membrane potential equation was modified as follows:

$$\frac{dV}{dt} = -\frac{C_m \cdot I_{ion} + N_f \cdot I_{gap}}{C_m}, \tag{2.5}$$

$$I_{gap} = G_{gap}(V - V_{fibro}), \tag{2.6}$$

where V_{fibro} is the fibroblast potential, G_{gap} is the conductance of the hESC-CM-fibroblast coupling ($G_{gap} = 1\ nS$ [37]) and N_f is the number of coupled fibroblasts. Details on the fibroblast model are reported in the Supplementary Methods on page 163 (Eqs. S92-S94).

2.2.14 Drug simulations

To reproduce the inhibition of SR Ca^{2+} release and the consequent Ca^{2+} transient reduction in ryanodine experiments the simulation was performed zeroing I_{up} and I_{rel} . To simulate E4031 (I_{Kr} blocker) and nickel (I_{CaT}, I_{Kr} and I_{NaCa} blocker) effects, in steady state conditions, a step reduction of conductance for the targeted currents was implemented in the model. The amount of conductance reduction for each current, which is reported in the Results Section, was chosen within the range of blocking action of the drug in order to better reproduce the specific experimental result obtained on a single cluster of hESC-CMs.

2.2.15 Numerical implementation

Differential equations were implemented in MATLAB (The MathWorks, Natick, MA) and solved using ode15s.

2.3 Results

2.3.1 The hESC-CM model

Fig. 2.2a shows simulated AP profiles for Early hESC-CMs obtained using our model: the modifications introduced with respect to the adult ventricular model were sufficient to elicit spontaneous beating. A comparison with experimental Early AP profiles obtained on intact EBs by multicellar recordings is provided in Table 2.2: a global comparison was done by calculating typical morphological parameters (AP features) for both experimental and simulated APs. This analysis demonstrated that our hESC-CM model was able to reproduce most of the experimental AP features, including Action Potential Duration (APD) at 30 (APD_{30}), 50 (APD_{50}), 70 (APD_{70}) and 90% (APD_{90}) of repolarization, V_{max}, F and the DDR. Simulated and experimental data differed for the MDP, which is more negative in the simulation.

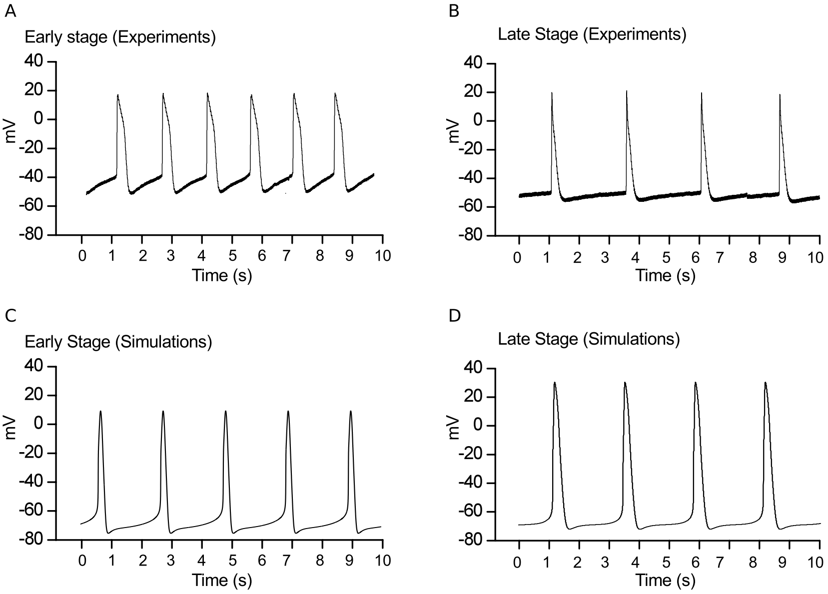

Figure 2.2: Simulated action potentials for (a) Early and (b) Late hESC-CMs clusters.

Table 2.2: Action potential features of experimental and simulated action potentials. Delta %, Late VS Early; APD, action potential duration; V$_{max}$ maximum upstroke velocity; MDP maximum diastolic potential; DDR diastolic depolarization rate; F frequency. Data reported as median and interquartile. All the experimental action potential features were measured on hESC-CM AP at the Early and Late stage [40].

	Early		Late		Delta %	
	Exp	Sim	Exp	Sim		
APD$_{30}$% (ms)	117 (107÷132)	121	163 (84÷256)	165	+ 40	+ 36
APD$_{50}$% (ms)	169 (149÷184)	163	258 (148÷374)	224	+ 53	+ 37
APD$_{70}$% (ms)	205 (181÷219)	191	325 (179÷465)	283	+ 59	+ 48
APD$_{90}$% (ms)	229 (216÷241)	225	419 (223÷506)	350	+ 83	+ 56
Vmax (mV/s)	4610 (3308÷5612)	4123	5566 (5198÷7047)	5620	+ 42	+ 36
MDP (mV)	-55 (-62÷-37)	-76	-51 (-62÷-42)	-73	-7	- 4
DDR (mV/s)	14.4 (11.1÷28.4)	9.7	9.9 (8.0÷11.1)	7.1	- 31	- 27
F (bpm)	27 (23÷53)	29	22 (20÷29)	24	- 17	- 17

2.3.2 Transition from Early to Late stage of development: effects of maturation

The simulated AP profile at the Late stage and the comparison with experimental APs obtained on intact EBs by multicellular recordings are reported in Fig. 2.2b and Table 2.1, respectively. These results show that the changes introduced in the model parameters between the Early and Late stage allow to reproduce the documented [6] maturation effects on AP shape. In particular, during the transition from the Early to the Late stage, APD and V_{max} increase while spontaneous rate and slope of diastolic depolarization decrease.

2.3.3 Spontaneous firing and action potential shape dependence on current conductances

The sensitivity analysis performed on the Early and Late models was aimed to assess how variations in the maximum conductances of the most important membrane currents affect (i) the phenomenon of spontaneous beating and (ii) the AP shape. The spontaneous firing activity was not triggered at the Early stage in 2 tests only: RaI_{CaL}-20% and RaI_{NaCa}+20%. At the Late stage the spontaneous activity showed to be sensitive to more currents: the firing activity was triggered but stop after few dozens of seconds of simulations for RaI_{Na}+20%, RaI_{CaL}-20%, RaI_{f}-20%, RaI_{K1}+20%, RaI_{Kr}+20%, RaI_{NaK}+20% and RaI_{NaCa}+20%. When the spontaneous beating allowed to reach a steady state condition, the AP features absolute/relative sensitivities were computed (Fig. 2.3) as reported in the Methods section. At the Early stage MDP is affected by the inward I_{CaL}, I_{NaCa} (inward during the late-repolarization) and the outward I_{Kr}. The effect of I_f is extremely small, since at the MDP potential it is not activated yet, due to its high time constant. Also the I_{K1} effect is small since at this developmental stage the I_{K1} expression is low. The Late stage shows a more stable MDP (maximum variations: 7-8 %), but the I_{K1} effect is stronger, as consequence of a maturation-related increment in I_{K1} expression. As expected, V_{max} is mainly affected at both stages by the inward currents mainly acting during the upstroke: I_{Na} and I_{CaL} while the rate of spontaneous beating resulted to be more sensitive to I_{CaL}, I_{NaK}, I_{NaCa}, I_f (Early stage) and I_{K1} (Late stage). I_{CaL}, I_{NaK} and I_{K1} had the most strong effect on DDR and F at both stages; these AP features show also an important sensitivity to I_f increments at the Early stage. It is interesting to note

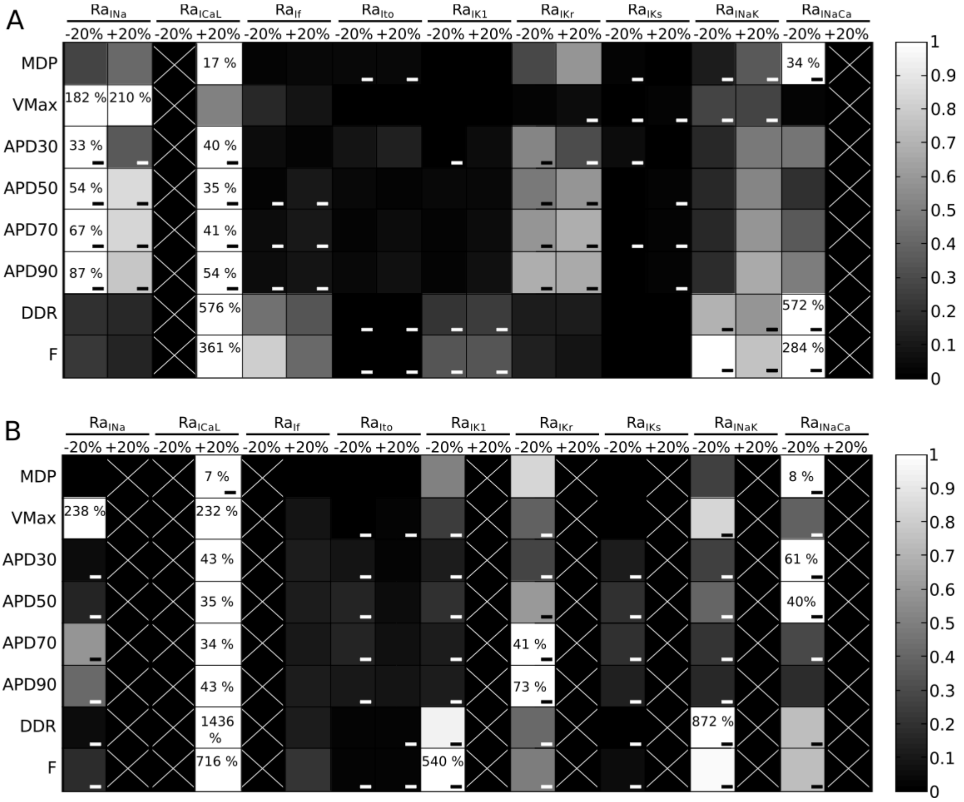

Figure 2.3: Relative sensitivity maps for the Early (a) and Late (b) models. AP features (rows) VS ratios RaI_{xx} (columns) used to rescale the maximum conductances/currents/fluxes were considered. For each RaI_{xx} the relative sensibilities at -20% and + 20% were taken into account. White color indicates maximum relative sensitivity of a particular AP feature among all ratios, whereas black indicates AP feature and ratio are independent. White X indicates the absence of spontaneous firing during a particular test. Percentages in each white box indicate the maximum absolute sensitivity of the AP feature correspondent to that row for all ratios. Negative sign indicates that AP feature and ratio vary inversely.

that also I_{NaCa} reduction increase DDR and F at both stages but particularly at the Early one: a smaller I_{NaCa} (inward during late-repolarization) makes MDP more negative (-81 mV vs -76 mV, RaI_{NaCa}-20% and control respectively) allowing a greater activation of I_f and thus increasing both DDR and F. Variations of the outward currents I_{K1} and I_{NaK} show the role of these currents in stabilizing the diastolic potential and, at the Late stage, increments block the spontaneous beating. APD is mainly affected by the inward currents I_{CaL} and I_{Na}, by I_{NaCa} (outward during the upstroke), I_{NaK} (Late only) and the outward I_{Kr}, especially during the late-repolarization. At the Early stage, the APD decreases after I_{CaL} increments: this counterintuitive result can be explained by using the model. In fact, it is due to a higher AP peak (20 mV vs 8.3 mV, RaI_{CaL}+20% vs control): the higher reached membrane potential allows a stronger I_{Kr} activation thus reducing APD. At the Late stage this phenomenon is not present, since in the AP peak increment is smaller (34.2 mV vs 30.2 mV, RaI_{CaL}+20% vs control), and I_{Kr} itself is smaller due to maturation. This different contribution of inward/outward currents to APD likely underlies the diverse APD rate-dependence (Fig. S2).

2.3.4 Coupling with fibroblasts

In order to partially overcome the discrepancy in MDP between the model and the experimental measurements, we introduced the contribution of fibroblasts, which are an essential component of EBs also for CM maturation. To assess the relevance of this issue in our model, we considered a simple system composed of a single hESC-CM coupled with 1 and 2 fibroblasts for each stage. Changes in basal AP due to fibroblast coupling are reported in Fig. 2.4a and 2.4c, for the Early and Late phase, respectively, while a quantification of these changes is summarized in Fig. 2.4b and 2.4d. Changes in most of the AP features as a function of fibroblast number were similar between the two stages. In particular, we observed an increment in DDR and rate while APA decreased. The effect on APD was different in the two stages. In the Early hESC-CM, lacking the plateau phase, the major effect is an inward current flowing from the coupled fibroblasts into the hESC-CM during the late repolarization phase, when hESC-CM membrane potential is negative to the fibroblast resting potential, promoting slowing of repolarization and APD increase. In the Late hESC-CM, showing significantly longer AP with respect to Early, the effect of an outward current, flowing towards coupled fibroblasts at depolarized potential and promoting hESC-CM repolarization and APD decrease, is also important. The overall result in Late hESC-CM is a decrease of APD_{30} and APD_{50} whereas APD_{70} and APD_{90} were almost not affected by coupling with fibroblasts. Importantly, as the number of coupled fibroblast increases from 0 to 2, a small rising of MDP occurred both at Early (-76 to -73 mV) and Late stage (-73 to -72mV). This effect was accompanied by a reduction of V_{max} at Early (4123 to 3443 mV/s) and Late stage (5620 to 2554 mV/s). At the same time, the membrane potential of coupled fibroblasts mimics the hESC-CM AP (data not shown), oscillating between -74 and 4 mV at the Early and between -72 and 26 mV at the Late stage.

2.3.5 Intracellular calcium

To assess the relevance of RyR-mediated SR Ca^{2+} release in our model, we simulated cytoplasmic Ca^{2+} oscillations in control conditions and after blockade of Ca^{2+} release. In control conditions, the Early model showed intracellular Ca^{2+} diastolic and systolic concentrations of 0.026 μM and 0.141 μM, respectively, with an amplitude of the transient of 0.115 μM. The mean rate of decay was 0.123 μM/s while the maximum upstroke velocity ($V_{maxCa,upstroke}$) was 1 μM/s and the maximum decay velocity ($V_{maxCa,decay}$) was 0.52 μM/s. Control values for the Late model were 0.063 μM and 0.506 μM for diastolic and systolic concentrations, 0.443 μM and 0.340 μM/s for amplitude and mean rate of decay. $V_{maxCa,upstroke}$ was 13 μM/s and $V_{maxCa,decay}$ was 1.4 μM/s. The blockade of the SR channels and pumps reduced the Ca^{2+} oscillation amplitude by only 12% at the Early stage, whereas the RyR-induced reduction was larger, 33%, at the Late stage (Fig. 2.5a and 2.5b). These results are similar to those reported experimentally in H1-CMs by [11] after 18-24 days and by [12] in cells assessed 30-40 days "post-beating", likely corresponding to 50 days of total time of differentiation. A more detailed comparison was performed between the data reported in [11] on caffeine-sensitive H1-CMs and our Early stage, also considering the transient elicited in [11] in stimulation condition. In order to compare the experimental and simulated $V_{maxCa,upstroke}$ and $V_{maxCa,decay}$ in control conditions we normalized them using the amplitude of the transient, since experimental data were reported in terms of fluorescence while ours as concentration values. Estimating from [11] transient amplitude 0.16 F340/380 and $V_{maxCa,upstroke}$ 1.5 F340/380/s we got a normalized $V_{maxCa,upstroke}$ of 9.3 1/s. Normalizing our Early $V_{maxCa,upstroke}$, our model reproduced 8.7 1/s. Comparing in the same manner the$V_{maxCa,decay}$

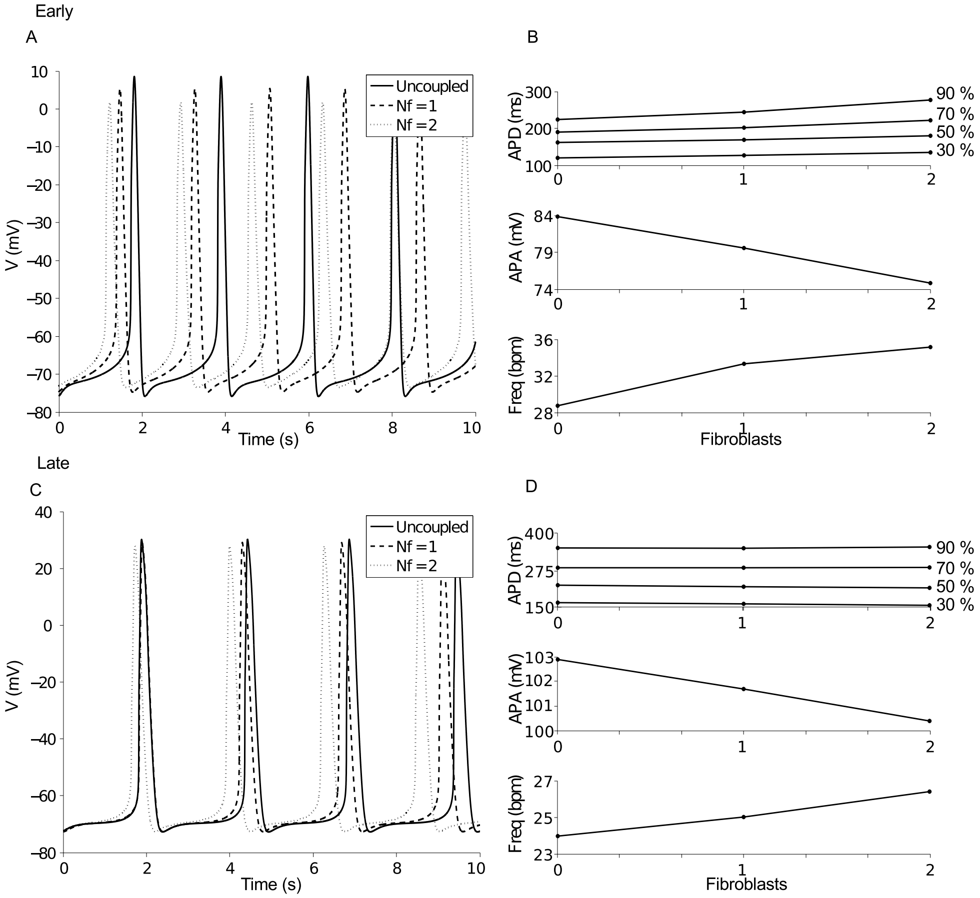

Figure 2.4: Electrical coupling between human embryonic stem cell-derived cardiomyocyte and fibroblasts. (a, c) Effects on APs, Early and Late stage respectively, of a variable number (N_f,) of fibroblasts. (b, d) Consequent changes of AP features, Early and Late stage respectively: both stages show an increment of the rate of spontaneous beating and an APA reduction. APD is slightly prolonged at the Early stage (especially APD$_{70}$ and APD$_{90}$) while at the Late stage the fibroblast effects are minor, showing only a slight reduction of APD$_{30}$.

(estimated experimental $V_{maxCa,decay}$ 0.3 F340/380/s) we got 1.9 1/s vs 4.5 1/s, respectively experimental [11] and simulated. The last comparison regards the reduced $V_{maxCa,decay}$ value after RyR application: in [11] an experimental value of 70% was reported, while our model simulated 78%.

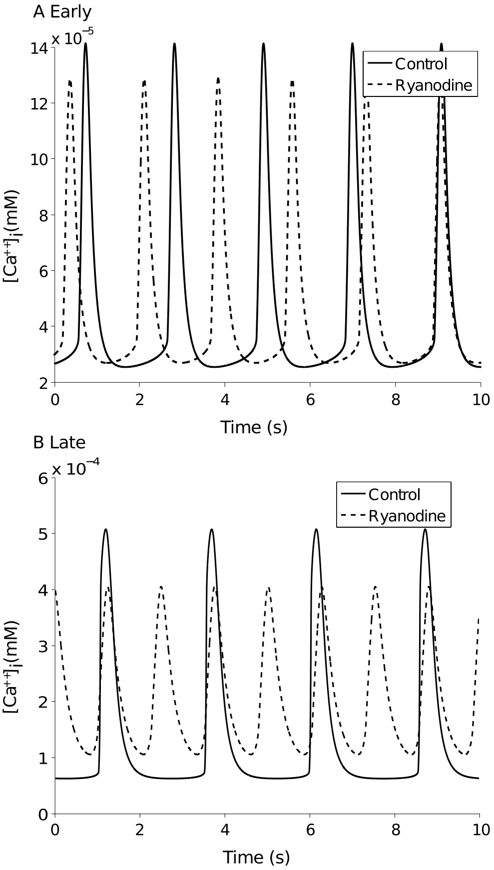

Figure 2.5: Simulation of the reduction of calcium transient amplitude under the effect of Ryanodine at Early (a) and Late (b) stages.

2.3.6 Drug simulations

Finally, we performed a preliminary test of the qualitative reproduction of the main effects on AP of well-established channel blockers. E4031 is known to prolong cardiac AP through I_{Kr} selective blockade. We tested the effect of E4031 on a single spontaneously beating cluster of hESC-CMs at Early stage and observed a progressive decrease of the pacing frequency, a depolarization of MDP and an increase of APD involving all phases of repolarization (Fig. 2.6a, left). These effects were fast on our experimental system and after 60 s from drug application the cluster showed a complete stop of its spontaneous electrical activity and beating [6]. To simulate this effect in our model, G_{Kr} was decreased by 50% of its Early value and this resulted in AP prolongation (Fig. 2.6a, right). In fact the AP lengthening measured at different values of repolarization were 12% (APD_{30}), 18% (APD_{50}), 47% (APD_{70}) and 110% (APD_{90}). In the simulation MDP was also depolarized by 4%, in accordance with a weaker contribution of repolarizing current, and frequency was reduced by 27%. In our model a decrease of I_{Kr} current larger than 50% produced a block of spontaneous beating, similarly to what observed experimentally [6].

In a single cluster of hESC-CMs at the Late stage, application of E4031 produced a fast depolarization of MDP and a remarkable increase in spontaneous rate with characteristic small amplitude oscillations of membrane potential (Fig. 2.6b, left). At this stage, simulation was obtained by 60% reduction of G_{Kr} that resulted in AP modifications qualitatively similar, even if smaller, to those observed experimentally. In particular, rate was increased by 97%, APD_{70} by 19%, APD_{90} by 65%, MDP was depolarized by 17% (Fig. 2.6b, right).

At millimolar concentration nickel is well known to largely block I_{NaCa} and I_{CaT}. Furthermore, it has also been reported to block at a very high extent I_{Kr} in sinoatrial node cells [41]. All these currents are involved in different phases of spontaneous beating generation and AP. In the Early stage, application of nickel produced a marked MDP depolarization, a sustained Action Potential Amplitude (APA) reduction and an increase of spontaneous rate, which lasted unaltered over time (Fig. 2.6c, left). Conversely, at the Late stage, nickel first slowed down and then blocked completely electrical activity (Fig. 2.6d, left). At both stages, simulations were performed reducing I_{CaT} and I_{Kr} by 90% and I_{NaCa} by 75% of their initial values. The effects on APA, MDP and beating rate detected at the Early stage were well reproduced (Fig. 2.6c, right). Blockade of spontaneous activity observed at the Late stage was also clearly mimicked in our model (Fig. 2.6d, right).

2.4 Discussion

The major aim of this work was to develop a mathematical model able to reproduce the basal electrophysiological properties of hESC-CMs and the modifications induced by in vitro maturation. This approach, has been applied for the first time to hESC-CMs and the model represents the first computational tool for studying the fundamental physiology of hESC-CMs, in particular those derived from the H1 cell line. Moreover, introducing the contribution of fibroblasts we approached the simulation of the properties of beating intact EBs, which represent the elementary functional unit able to promote electrophysiological maturation of hESC-CMs and therefore suitable for screening ion channel blockers and assessing the cardiac safety of drugs.

We reached the goal of reproducing the spontaneous AP profile of hESC-CMs, strongly focusing on the modifications occurring during the transition of intact EBs from the Early to the Late developmental stage. Specifically, we reproduced key modifications documented experimentally on intact EBs by multicellular recordings, including the decrease of spontaneous AP frequency in association with a reduced DDR, meaning that the automaticity was slowed down during simulated maturation, similarly to experimental observations. The maturation-related increase of APD was also satisfactorily mimicked by our model, thus reflecting the modifications identified for many ionic currents occurring during in vitro maturation. Of note, we chose this specific electrophysiological approach on intact EBs due to several advantages, including the preservation of tissue architecture that allows the detection of single cell transmembrane voltage resulting also from the contribution of neighbouring cells. The latter, beside non myocytic cells, may be represented by CMs with similar or different phenotypes, with a relative composition of different phenotypes depending mainly from the developmental stage under evaluation. In fact Early hESC-CMs have a rather homogeneous phenotype (mostly sinus nodal like) that progresses into different phenotypes in the Late phase (atrial, ventricular and sinus nodal). Therefore, our experimental and simulation data readily reflect the degree of phenotype dishomogeneity in most of AP parameters, resulting from the contribution of individual CMs at different stages (throughout the developmental process) and the

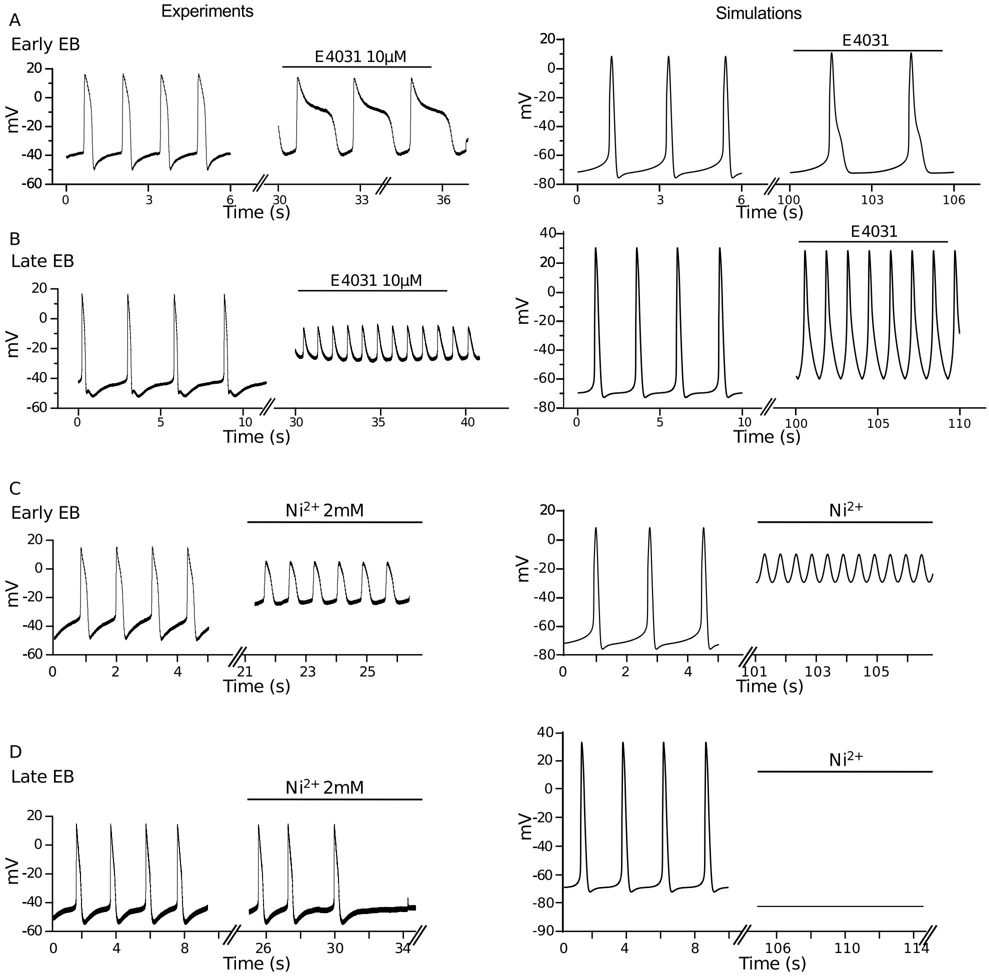

Figure 2.6: Effects of current blocking with E4031 and Nickel. Single experiments (left) and simulations (right) on the effect of 10 μM E4031 (I_{Kr} blocker) and of 2 mM Nickel (I_{NaCa}, I_{CaT}, I_{Kr} blocker) at Early (a, c) and Late (b, d) stages.

fate (ventricular, atrial or nodal). To further confirm this statement, the median measurements of AP duration at different percentage of repolarization have a lower interquartile range in the Early phase compared to the Late (see table 2.2).

Based on the integration into our model of original and literature data on different ionic currents, some considerations can be drawn on their role in the hESC-CM development.

I_{to} is known to play a key role during the early repolarization phase leading to the notched shape and plateau phase present in human adult ventricular and atrial cells [42]. In our experimental conditions we found that I_{to} density increased from the Early to the Late phase. This result is in line with our previous data demonstrating a functional and molecular up-regulation of I_{to} during hESC-CMs maturation. It further confirms that this channel is a fundamental marker of functional CM maturation among mammalians [6]. These modifications were favourably integrated in our model, thus demonstrating their positive contribution to its final formulation. However, our measurements of I_{to} showed substantial current density also for negative potentials. For this reason I_{to} half-maximal activation was shifted from 20 to -5 mV (Fig. 2.1d) whereas the steepness of the model curve was kept slightly greater than the experimental one, as already done and discussed in the adult model [16].

A different set of original data integrated in our model is related to I_f. It is an inward current involved in the generation of spontaneous electrical activity, identified and characterized in our previous study on H1-hESC-CMs [6]. In the present study we further characterized this current identifying its functional relevance over an extended period of time. We calculated maximal conductance for the Early stage and extrapolated its value at the Late one on the basis of a cumulative reduction of HCN total transcript. Although functional properties of currents do not uniquely depend on the amount of channel transcript/s, we hypothesised that I_f density is likely to decrease during hESC maturation on the basis of different experimental evidences. First, the rate of spontaneous beating and the slope of the diastolic depolarization decrease with maturation (Table 2.2); secondly, I_f downregulation is a well established marker of functional maturation of native CMs [43, 44]. These observations led us to integrate in our model a I_f contribution declining over maturation time. As observed for I_{to}, this implementation had a positive effect on the model mimicking properties. As shown in Fig. 2.3, modulation of I_f mainly affects in the model the rate of spontaneous beating and the DDR at both stages but especially at the Early one. The Late stage represented a scenario characterized by a smaller I_f and which evolves towards cells with no automaticity, so the 20% reduction of RaI_f led to no spontaneous activity.

Experimental evidence documents the occurrence of developmental changes of I_{NaCa} in different animal models, with maximal current density lowering throughout maturation [23]. In humans, I_{NaCa} expression peaks at mid-gestation, overcoming that of the adult heart [45]. In hESC-CMs, [11] reported that I_{NaCa} expression in the Early phase is higher with respect to that found in human fetal and adult ventricular CMs. This evidence is in line with our experimental results (see Fig. 2.1f), showing larger current density both in Ca^{2+} outward and inward modes, at the Early stage with respect to the Late one. By contrast, a recent study [46] performed on a similar model led to opposite results, *i.e.* maximal current occurring in the Late stage. The explanation for such a difference is not obvious; diverse developmental window and/or cell phenotypes (ventricular and atrial vs ventricular) may account for these discrepancies. Model-based analysis showed that at both stages I_{NaCa} (Fig. 2.3) modulation affects basically all the AP features (tests with RaI_{NaCa}-20%) and the occurrence of spontaneous beating (tests with RaI_{NaCa}+20%).

Other relevant maturation-related current modifications introduced in our model are consistent with previous observations in rodent ESC-CMs. In particular I_{Kr} decrease and I_{Na} increase confirmed to be important to achieve AP changes such as AP prolongation and increase in V_{max} observed with hESC-CM development. As expected I_{Na} had the strongest influence on V_{max} while I_{Kr} had a considerable effect on the APD, especially in the latest phases of the repolarization (see Fig. 2.3).

The sensitivity analysis summarized in Fig. 2.3 helps in assessing the maturation-related effects on the spontaneous contractile activity of hESC-CMs, in particular showing that at the Late stage it is more sensitive to current variations that at the Early stage. At the Early stage the reduction of the depolarizing I_{CaL} (necessary for the upstroke) and the increment of I_{NaCa} (inward current during the late-repolarization) caused the spontaneous beating stop. In addition to the reduced I_{CaL} and increased I_{NaCa} tests, the Late stage showed no spontaneous beating also for increments of the main repolarizing currents I_{Kr}, I_{K1}, I_{Ks} and I_{NaK}, thus supporting the hypothesis of a weakening of the spontaneous depolarization during maturation. Moreover, also the effect of the 20% I_f reduction at the Late stage is indicative of this mechanism since I_f was already reduced during the transition from the Early to the Late stage.

We also tested coupling of fibroblasts with the hESC-CM model. Our hypothesis was that such approach could improve the quality of simulated APs that are generated by a complex system comprising CMs embedded in a cluster of different cells, such as fibroblasts. Indeed, one specific AP feature predicted by our model (MDP) differed substantially with respect to the experimental data. At both developmental stages, effects of coupling were small and consisted of MDP depolarization and increase of DDR and frequency. These effects can be explained by observing that during diastole fibroblast membrane potential is less negative with respect to that of CMs, causing a small depolarizing current flowing into CMs. Although limited, these modifications collectively move our simulation towards the experimental measurements, therefore improving the mimicking potential of our model. On this basis, it would be interesting to explore the possibility to enlarge the cell network by including different cell phenotypes (e.g. endothelial cells) possibly present in vivo. Globally, our results are in line with similar studies [37], where coupling of the TenTusscher model to fibroblasts led to a slightly depolarized resting potential, reduced APA and to the electrotonic modulation of the fibroblast potential by the coupled CM.

Recently, increasing attention has been focused on the development and maturation of the SR activity in hESC-CMs. Accumulated evidence points to a significant activity of Ca^{2+} release from SR [11, 12], even if less organized and regulated than in mature CMs. In fact, while in the Early phase H1-hESC-CMs express SERCA2a, other proteins such as calsequestrin, triadin and junctin are almost absent [47]. Moreover, at 40-50 days of differentiation, T-tubules remain undetected on the sarcolemma, suggesting a topological environment different from mature, where Ca^{2+} influx through Ca^{2+} channels in the T-tubule is tightly associated with sarcoplasmic RyR channels [10]. Overexpression of calsequestrin in H1-hESC-CMs failed to induce the growth of T-tubules even though SR load and Ca^{2+} transient amplitude became more similar to those of mature CMs [48]. Simulations of Ca^{2+} transients using our model led to results fully consistent with the experimental data reported above. In fact, upon blockade of Ca^{2+} release from SR we found a decreased Ca^{2+} transient amplitude by 12% in the Early, and by 33% in the Late phase, similarly to the results reported experimentally [11, 12]. Overall, these results indicate that in the Early stage Ca^{2+} cycling is mainly governed by sarcolemmal fluxes, while upon maturation Ca^{2+} release from SR increases its contribution moving toward a functional integration with sarcolemma to generate rhythmic activity. This evidence is in line with recent data obtained in late-stage mouse ESC [47] and further extends the predictive potential of our model to intracellular Ca^{2+} handling processes. Simulated block of Ca^{2+} release also increased the oscillation frequency (see Fig. 2.5); we are not aware of experimental reports on this specific aspect in hESC-CMs which, on the other hand, seems in contrast with the effect of RyR knock out in ESC-CMs [49]. However, in the same conditions, a consistent increase in the frequency of AP-induced Ca^{2+} transients is apparent also in [12] (Fig. 2.6), thus suggesting that further investigation supported also by model based analysis might provide mechanistic insights on this issue.

In our model, simulations of channel blockers were aimed to test, as a proof of concept, a qualitative reproduction of the main experimentally AP modifications observed in preliminar experiments. In the case of I_{Kr}, a reduction in the maximal conductance simulated the application of E4031. This operation altered AP shapes quite similarly to what observed in the experiment, despite the fact that simulated AP prolongation was far less pronounced at the Early stage while at the Late stage MDP was more negative with respect to the experimental trace. Importantly, our model replicates the effect of E4031 on the frequency of spontaneous beating, which decreases in the Early stage and markedly increases in the Late one.

Our experiments using 2 mM nickel were simulated by a relevant blockade of I_{NaCa}, I_{CaT} and I_{Kr} in the model, in accordance with the lack of selectivity of nickel at this concentration and the high levels of block reported for these currents. At the Early stage simulations and experimental recording similarly show a residual electrical activity slightly different in frequency and amplitude (see Fig. 2.6c); nonetheless, both results suggest that residual currents are sufficient to drive a repetitive potential oscillation of small amplitude occurring at depolarized potentials. For the Late stage experimental traces and simulations show a complete block of spontaneous activity (see Fig. 2.6d) occurring at negative potential values, opening the hypothesis that in this phase, where other depolarizing currents such as I_f are downregulated, I_{NaCa} plays a key role in sustaining the spontaneous activity. Our results are consistent with those of similar experiments [46] performed with 5 mM nickel, a concentration expected to exert a higher level of channel blockade. In fact, with this higher nickel concentration no Ca^{2+} transients due to spontaneous activity were recorded at any developmental stage.

2.4.1 Limitations

The main limitations of our work are related to i) the shortage of data and ii) the variability of phenotypes. We built an AP model for human embryonic stem cells derived cardiomyocytes. However, many data to build the model are taken from published experimental work on different animal species. The crossbreeding process of data from human and animal CMs represented a compulsory choice for our model, since some current properties expressed in the adult ventricular cells were unknown or not sufficiently characterized in hESC-CMs. A more accurate numerical model of "human" embryonic stem cells derived cardiomyocytes would require further experimental investigations. This should be considered as a first step in the effort of mathematically describing the ESC-CM electrophysiology aimed at capturing the qualitative mechanisms.

The choice of a specific human adult ventricular AP model as the basis for the hESC-CM model could be perceived as a limitation of the present work. We chose as the "starting point" for the development of our model a modified version of the TenTusscher model [15], in which I_{Kr}, I_{Ks} and I_{CaL} were changed with respect to their original formulation. From this starting point, in order to reproduce developmental changes in each current we modulated (through the RaI_{xx} ratios) the current maximal conductances. But at the same time the kinetic of several currents were changed based on data from ESC-CMs: I_{Na}, I_{CaL}, I_{to},I_{K1}, I_{NaCa}. Moreover, two relevant membrane currents that were not present in the adult ventricular model (I_{CaT} and I_f) were incorporated in our model. All these modifications reduced the actual impact on the final results of the initial choice of the starting point. A sensitivity analysis with respect to the choice of the parent model was far beyond the scope of the present work. It is also worth noting that the modification of the Ten Tusscher model allowed the correct prediction of APD shortening at higher $[Ca^{2+}]_o$ [15]. All the more recent models (e.g. [50]) show unrealistic APD prolongation upon increase of extracellular calcium. This aspect is particularly relevant for our study, in which we had to reproduce intracellular AP recordings obtained with 2.7 mM Ca^{2+} in the external solution [40].

The difference in MDP between experiments and simulations is a limitation, possibly related to an incomplete description of the complex interconnection within the EBs. For example, in simulating AP recorded from EBs, only CM to fibroblast coupling has been considered. Other variables, such as CM to CM gap junctions likely contribute to the AP properties of EBs. However, such a term would dramatically complicate the system of differential equations and goes beyond the scope of the present work.

2.5 Conclusions

In conclusion, this study provides the first modelling tool able to simulate the membrane AP, the associated intracellular Ca^{2+} handling properties and the modification occurring over the maturation process of hESC-CMs. The simulation of the transition from Early to Late developmental stage involved: increasing I_{to} density, declining I_f contribution, decreasing I_{NaCa} current density, I_{Kr} decrease and I_{Na} increase. Moreover, an increasing contribution to Ca^{2+} cycling of the Ca^{2+} release from SR was pointed out.

We expect to overcome inherent limitations present in the model by further experimental investigations exploring unknown properties of basic physiology of hESC-CMs, possibly including different stem cell lines. Also, the combined use of novel pharmacological/simulated challenges will be useful to implement and validate the predictive potential of the model. Finally, novel challenges come from studies (including drug testing) in CMs from induced pluripotent stem cells carrying genetic mutations [51, 52]; the development of disease-specific cell lines for genetic cardiac disorders prompts toward the refinement of this mathematical modelling to address future directions in this field.

Bibliography

[1] Thomson JA. Embryonic Stem Cell Lines Derived from Human Blastocysts. Science 1998;282:1145–1147.

[2] Rao TP, Kühl M. An updated overview on Wnt signaling pathways: a prelude for more. Circ Res 2010;106(12):1798–1806.

[3] Phillips BW, Crook JM. Pluripotent human stem cells: A novel tool in drug discovery. BioDrugs April 2010;24(2):99–108.

[4] Bel A, Planat-Bernard V, Saito A, Bonnevie L, Bellamy V, Sabbah L, Bellabas L, Brinon B, Vanneaux V, Pradeau P, Peyrard S, Larghero J, Pouly J, Binder P, Garcia S, Shimizu T, Sawa Y, Okano T, Bruneval P, Desnos M, Hagège AA, Casteilla L, Pucéat M, Menasché P. Composite cell

sheets: a further step toward safe and effective myocardial regeneration by cardiac progenitors derived from embryonic stem cells. Circulation 2010; 122(11 Suppl):S118–123.

[5] Pekkanen-Mattila M, Kerkelä E, Tanskanen JMA, Pietilä M, Pelto-Huikko M, Hyttinen J, Skottman H, Suuronen R, Aalto-Setälä K. Substantial variation in the cardiac differentiation of human embryonic stem cell lines derived and propagated under the same conditions–a comparison of multiple cell lines. Ann Med January 2009;41(5):360–370. ISSN 1365-2060.

[6] Sartiani L, Bettiol E, Stillitano F, Mugelli A, Cerbai E, Jaconi ME. Developmental changes in cardiomyocytes differentiated from human embryonic stem cells: a molecular and electrophysiological approach. Stem Cells 2007; 25(5):1136–1144.

[7] Zeevi-Levin N, Itskovitz-Eldor J, Binah O. Functional properties of human embryonic stem cell-derived cardiomyocytes. Crit Rev Eukaryot Gene Expr January 2010;20(1):51–59.

[8] Asai Y, Tada M, Otsuji TG, Nakatsuji N. Combination of functional cardiomyocytes derived from human stem cells and a highly-efficient microelectrode array system: an ideal hybrid model assay for drug development. Curr Stem Cell Res Ther 2010;5(3):227–232.

[9] Kim C, Majdi M, Xia P, Wei KA, Talantova M, Spiering S, Nelson B, Mercola M, Chen HSV. Non-cardiomyocytes influence the electrophysiological maturation of human embryonic stem cell-derived cardiomyocytes during differentiation. Stem Cells Dev June 2010;19(6):783–795. ISSN 1557-8534.

[10] Lieu DK, Liu J, Siu CW, Mcnerney GP, Tse HF, Abu-Khalil A, Huser T, Li RA. Absence of Transverse Tubules Contributes to Non-Uniform Ca2+Wavefronts in Mouse and Human Embryonic Stem Cell–Derived Cardiomyocytes. Stem Cells Dev 2009;18(10):1493–1500.

[11] Liu J, Fu JD, Siu CW, Li RA. Functional Sarcoplasmic Reticulum for Calcium Handling of Human Embryonic Stem Cell-Derived Cardiomyocytes: Insights for Driven Maturation. Stem Cells 2007;25(12):3038–3044.

[12] Satin J, Itzhaki I, Rapoport S, Schroder EA, Izu L, Arbel G, Beyar R, Balke CW, Schiller J, Gepstein L. Calcium handling in human embryonic stem cell-derived cardiomyocytes. Stem Cells 2008;26(8):1961–1972.

[13] Itzhaki I, Schiller J, Beyar R, Satin J, Gepstein L. Calcium handling in embryonic stem cell-derived cardiac myocytes: of mice and men. Ann N Y Acad Sci October 2006;1080:207–215. ISSN 0077-8923.

[14] Noble D. Computational Models of the Heart and Their Use in Assessing the Actions of Drugs. J Pharmacol Sci 2008;107(2):107–117. ISSN 1347-8613.

[15] Grandi E, Pasqualini FS, Pes C, Corsi C, Zaza A, Severi S. Theoretical investigation of action potential duration dependence on extracellular Ca2+ in human cardiomyocytes. J Mol Cell Cardiol March 2009;46(3):332–342.

[16] ten Tusscher KHWJ, Noble D, Noble PJ, Panfilov AV. A model for human ventricular tissue. Am J Physiol Heart Circ Physiol April 2004; 286(4):H1573–1589.

[17] Hodgkin A, Huxley A. A quantitative description of membrane current and its application to conduction and excitation in nerve. J Physiol Lond 1952; 117(4):500–544.

[18] Ferron L, Capuano V, Deroubaix E, Coulombe A, Renaud JF. Functional and molecular characterization of a T-type Ca(2+) channel during fetal and postnatal rat heart development. J Mol Cell Cardiol May 2002;34(5):533–546. ISSN 0022-2828.

[19] Davies MP, An RH, Doevendans P, Kubalak S, Chien KR, Kass RS. Developmental changes in ionic channel activity in the embryonic murine heart. Circ Res January 1996;78(1):15–25.

[20] Kato Y, Masumiya H, Agata N, Tanaka H, Shigenobu K. Developmental changes in action potential and membrane currents in fetal, neonatal and adult guinea-pig ventricular myocytes. J Mol Cell Cardiol July 1996; 28(7):1515–1522.

[21] Liu W, Yasui K, Opthof T, Ishiki R, Lee JK, Kamiya K, Yokota M, Kodama I. Developmental changes of Ca(2+) handling in mouse ventricular cells from early embryo to adulthood. Life Sci August 2002;71(11):1279–1292.

[22] Masuda H, Sperelakis N. Inwardly rectifying potassium current in rat fetal and neonatal ventricular cardiomyocytes. Am J Physiol October 1993;265(4 Pt 2):H1107–1111.

[23] Itoh H, Naito Y, Tomita M. Simulation of developmental changes in action potentials with ventricular cell models. Syst Synth Biol March 2007;1(1):11–23.

[24] Maltsev Va, Lakatta EG. Synergism of coupled subsarcolemmal Ca2+ clocks and sarcolemmal voltage clocks confers robust and flexible pacemaker function in a novel pacemaker cell model. Am J Physiol Heart Circ Physiol March 2009;296(3):H594–615. ISSN 0363-6135.

[25] Wang K, Terrenoire C, Sampson KJ, Iyer V, Osteen JD, Lu J, Keller G, Kotton DN, Kass RS. Biophysical properties of slow potassium channels in human embryonic stem cell derived cardiomyocytes implicate subunit stoichiometry. The Journal of physiology December 2011;589(Pt 24):6093–6104. ISSN 1469-7793.

[26] Otsu K, Kuruma A, Yanagida E, Shoji S, Inoue T, Hirayama Y, Uematsu H, Hara Y, Kawano S. Na+/K+ ATPase and its functional coupling with Na+/Ca2+ exchanger in mouse embryonic stem cells during differentiation into cardiomyocytes. Cell calcium February 2005;37(2):137–151.

[27] Satin J, Kehat I, Caspi O, Huber I, Arbel G, Itzhaki I, Magyar J, Schroder EA, Perlman I, Gepstein L. Mechanism of spontaneous excitability in human embryonic stem cell derived cardiomyocytes. J Physiol Lond 2004;559(Pt 2):479–496.

[28] Ono K, Iijima T. Cardiac T-type Ca(2+) channels in the heart. J Mol Cell Cardiol January 2010;48(1):65–70. ISSN 1095-8584.

[29] Yanagi K, Takano M, Narazaki G, Uosaki H, Hoshino T, Ishii T, Misaki T, Yamashita JK. Hyperpolarization-activated cyclic nucleotide-gated channels and T-type calcium channels confer automaticity of embryonic stem cell-derived cardiomyocytes. Stem Cells November 2007;25(11):2712–2719. ISSN 1549-4918.

[30] Courtemanche M, Ramirez RJ, Nattel S. Ionic mechanisms underlying human atrial action potential properties: insights from a mathematical model. Am J Physiol July 1998;275(1 Pt 2):H301–321.

[31] Spence SG, Vetter C, Hoe CM. Effects of the class III antiarrhythmic, dofetilide (UK-68,798) on the heart rate of midgestation rat embryos, in vitro. Teratology April 1994;49(4):282–292.

[32] Chun KR, Koenen M, Katus HA, Zehelein J. Expression of the IKr components KCNH2 (rERG) and KCNE2 (rMiRP1) during late rat heart development. Exp Mol Med August 2004;36(4):367–371.

[33] Wang L, Feng ZP, Kondo CS, Sheldon RS, Duff HJ. Developmental changes in the delayed rectifier K+ channels in mouse heart. Circ Res July 1996; 79(1):79–85.

[34] DiFrancesco D. A new interpretation of the pace-maker current in calf Purkinje fibres. J Physiol Lond 1981;314:359–376.

[35] Romero L, Pueyo E, Fink M, Rodriguez B. Impact of ionic current variability on human ventricular cellular electrophysiology. AJP Heart and Circulatory Physiology October 2009;297(4):H1436–H1445. ISSN 1522-1539.

[36] Romero L, Carbonell B, Trenor B, Rodríguez B, Saiz J, Ferrero JM. Systematic characterization of the ionic basis of rabbit cellular electrophysiology using two ventricular models. Progress in Biophysics and Molecular Biology October 2011;107(1):60–73. ISSN 0079-6107.

[37] MacCannell KA, Bazzazi H, Chilton L, Shibukawa Y, Clark RB, Giles WR. A mathematical model of electrotonic interactions between ventricular myocytes and fibroblasts. Biophys J June 2007;92(11):4121–4132. ISSN 0006-3495.

[38] Kohl P, Kamkin AG, Kiseleva IS, Noble D. Mechanosensitive fibroblasts in the sino-atrial node region of rat heart: interaction with cardiomyocytes and possible role. Exp Physiol November 1994;79(6):943–956. ISSN 0958-0670.

[39] Jacquemet V, Henriquez CS. Modelling cardiac fibroblasts: interactions with myocytes and their impact on impulse propagation. Europace November 2007;9(Suppl. 6:vi29–37. ISSN 1532-2092.

[40] Bettiol E, Sartiani L, Chicha L, Krause KH, Cerbai E, Jaconi ME. Fetal bovine serum enables cardiac differentiation of human embryonic stem cells. Differentiation research in biological diversity October 2007;75(8):669–81. ISSN 0301-4681.

[41] Song DK, Earm YE, Ho WK. Blockade of the delayed rectifier K+ currents, IKr, in rabbit sinoatrial node cells by external divalent cations. Pflugers Arch 1999;438(2):147–153.

[42] Oudit GY, Kassiri Z, Sah R, Ramirez RJ, Zobel C, Backx PH. The molecular physiology of the cardiac transient outward potassium current (I(to)) in normal and diseased myocardium. J Mol Cell Cardiol May 2001;33(5):851–872. ISSN 0022-2828.

[43] Cerbai E, Pino R, Sartiani L, Mugelli A. Influence of postnatal-development on I(f) occurrence and properties in neonatal rat ventricular myocytes. Cardiovasc Res May 1999;42(2):416–423. ISSN 0008-6363.

[44] Yasui K, Liu W, Opthof T, Kada K, Lee JK, Kamiya K, Kodama I. I(f) current and spontaneous activity in mouse embryonic ventricular myocytes. Circ Res March 2001;88(5):536–542. ISSN 1524-4571.

[45] Qu Y, Ghatpande A, El-Sherif N, Boutjdir M. Gene expression of Na+/Ca2+ exchanger during development in human heart. Cardiovasc Res March 2000; 45(4):866–873.

[46] Fu JD, Jiang P, Rushing S, Liu J, Chiamvimonvat N, Li RA. Na+/Ca2+ exchanger is a determinant of excitation-contraction coupling in human embryonic stem cell-derived ventricular cardiomyocytes. Stem Cells Dev 2010; 19(6):773–782.

[47] Zahanich I, Sirenko SG, Maltseva LA, Tarasova YS, Spurgeon HA, Boheler KR, Stern MD, Lakatta EG, Maltsev VA. Rhythmic beating of stem cell-derived cardiac cells requires dynamic coupling of electrophysiology and Ca cycling. J Mol Cell Cardiol January 2011;50(1):66–76.

[48] Liu J, Lieu DK, Siu CW, Fu JD, Tse HF, Li RA. Facilitated maturation of Ca2+ handling properties of human embryonic stem cell-derived cardiomyocytes by calsequestrin expression. Am J Physiol Cell Physiol 2009; 297(1):C152–159.

[49] Yang H, Tweedie D, Wang S, Guia A, Vinogradova T, Bogdanov K, Allen PD, Stern MD, Lakatta EG, Boheler KR. The ryanodine receptor modulates the spontaneous beating rate of cardiomyocytes during development. Proc Natl Acad Sci U S A July 2002;99(14):9225–9230.

[50] O'hara T, Virág L, Varró A, Rudy Y. Simulation of the Undiseased Human Cardiac Ventricular Action Potential: Model Formulation and Experimental Validation. PLoS Comput Biol May 2011;7(5):e1002061. ISSN 1553-7358.

[51] Yazawa M, Hsueh B, Jia X, Pasca AM, Bernstein JA, Hallmayer J, Dolmetsch RE. Using induced pluripotent stem cells to investigate cardiac phenotypes in Timothy syndrome. Nature March 2011;471(7337):230–234.

[52] Matsa E, Rajamohan D, Dick E, Young L, Mellor I, Staniforth A, Denning C. Drug evaluation in cardiomyocytes derived from human induced pluripotent stem cells carrying a long QT syndrome type 2 mutation. Eur Heart J April 2011;32(8):952–962.

CHAPTER

THREE

COMPUTATIONAL MODELS OF VENTRICULAR-LIKE AND ATRIAL-LIKE HUMAN INDUCED PLURIPOTENT STEM CELL DERIVED CARDIOMYOCYTES

Michelangelo Paci[1], Jari Hyttinen[2,3], Katriina Aalto-Setälä[3,4], Stefano Severi[1]

[1] *Biomedical Engineering Laboratory - D.E.I.S., University of Bologna, Italy*
[2]*BME, Tampere University of Technology, Tampere, Finland*
[3]*IBT, University of Tampere, Tampere, Finland*
[4]*Tampere University Hospital, Heart Center, Tampere, Finland*

The content of this chapter is under submission.

Abstract

The clear importance of human induced pluripotent stem cell derived cardiomyocytes (hiPSC-CMs) as an *in-vitro* model highlights the relevance of studying these cells and their function also *in-silico* . Moreover, the phenotypical differences between the hiPSC-CM and adult myocyte action potentials (APs) call for understanding of how hiPSC-CMs are maturing towards adult myocytes. Using recently published experimental data, we developed two computational models of the hiPSC-CM AP, distinguishing between the ventricular-like and atrial-like phenotypes, emerging during the differentiation process of hiPSC-CMs. Also, we used the computational approach to quantitatively assess the role of ionic mechanisms which are more likely responsible for the not completely mature phenotype of hiPSC-CMs. Our models reproduce the typical hiPSC-CM ventricular-like and atrial-like spontaneous APs and the response to prototypical current blockers, namely tetrodotoxine, nifedipine, E4041 and 3R4S-Chromanol 293B. Moreover, simulations using our ventricular-like model suggest that the interplay of immature $\mathrm{I_{Na}}$, $\mathrm{I_f}$ and $\mathrm{I_{K1}}$ currents is the main responsible for spontaneous beating in hiPSC-CM whereas a negative shift in $\mathrm{I_{CaL}}$ activation causes the observed long lasting AP. In conclusion, this work provides two novel tools useful in investigating the electrophysiological features of hiPSC-CMs, whose importance is growing fast as *in-vitro* models for pharmacological studies.

3.1 Introduction

The role of computational modelling in cardiac cell electrophysiology has become more and more important in recent years, enabling deeper understanding of the cardiomyocyte (CM) function. This, together with the growing available computing power, sparked the development of a large variety of mathematical models representing the *in-silico* versions of almost all the *in-vitro* models used in the experimental practice. Diverse animal models (rabbit [1], guinea pig [2], canine [3]) were produced, as well as human models deeply focusing on the characteristics of different cardiac phenotypes, e.g. ventricular [4–7] and atrial [8] cardiomyocytes. Recently, stem cell-derived cardiomyocytes appeared as a new promising *in-vitro* model [9, 10], especially in the perspective of regenerative medicine in order to restore the functionality and repair damaged or infarcted cardiac areas. Moreover, the role of specific human CMs as *in-vitro* drug models is increasing. Human embryonic stem cell-derived cardiomyocytes (hESC-CMs) seem to be a promising tool, anyway the ethical issues about using human embryos in scientific research slowed this research down.

Recent studies [11, 12] showed that it is possible inducing pluripotency, i.e. the power of differentiating into all the tissue composing the embryo but not into the extra-embryonic tissues, in somatic cells such as fibroblasts. The basic procedure consists in introducing genetic factors (such as OCT3/4, SOX2, KLF4 and c-Myc22 or OCT4, SOX2, NANOG and LIN2829) into the non-originally pluripotent cells: these cells were thus named induced pluripotent stem cells. Experiments on human somatic cells showed the feasibility in differentiating human induced pluripotent stem cells (hiPSCs) into cardiomyocytes (hiPSC-CMs) [13]. This procedure offers various advantages: (i) no ethical issues, (ii) patient-specificity [14] of the produced cells, valuable in terms of autologous transplantation without rejection issues, (iii) disease-specificity [15, 16] of the hiPSC-CMs. Even if hiPSC-CMs are not used in clinical practice yet, they are considered a very promising *in-vitro* model for pharmacological studies and drug tests [17, 18].

This new *in-vitro* model shows some relevant differences with respect to the adult myocytes such as the spontaneous electrical activity, i.e. APs firing without an external stimulus, or the shorter duration of the AP [17]: so models of adult cardiac AP result inadequate in describing the hiPSC-CM electrophysiology. A new, specific, *in-silico* model of hiPSC-CM AP would be extremely useful in order to investigate their physiological properties.

In order to fill this gap, we developed a novel model of hiPSC-CM, based on the experimental data, recently published in Ma *et al.* [17] , also discriminating among ventricular-like and atrial-like hiPSC-CMs. To test our model and its performance, we challenged our model by reproducing experimentally recorded changes in the AP shape due to specific current blockers. Finally, we used the computational approach to quantitatively assess the role of ionic mechanisms which are more likely responsible for the not completely mature phenotype of hiPSC-CMs. This was done by analysing several hybrid models built by inserting one “adult current” into the hiPSC-CM model.

3.2 Materials and Methods

3.2.1 Ventricular-like and atrial-like hiPSC-CM models

Our ventricular-like and atrial-like hiPSC-CM models follow the classical Hodgkin & Huxley scheme, taking into account the following currents:

$$C\frac{dV}{dt} = -(I_{Na}+I_{CaL}+I_{f}+I_{K1}+I_{Kr}+I_{Ks}+I_{to}+I_{NaCa}+I_{NaK}+I_{pCa}-I_{stim}) \tag{3.1}$$

where C is cell capacitance, V the membrane voltage and I_{stim} represents the stimulus current. Currents were formulated according to the framework reported in [7, 19], with the exception of $\mathrm{I_{CaL}}$, whose structure was taken from [21]; current parameters were then tuned to properly fit the hiPSC-CM experimental data.

Experimental data for $\mathrm{I_{Na}}$, $\mathrm{I_{CaL}}$, $\mathrm{I_{f}}$, $\mathrm{I_{to}}$, $\mathrm{I_{K1}}$, $\mathrm{I_{Kr}}$ and $\mathrm{I_{Ks}}$ were derived from Ma *et al.* [17], who recorded these currents on hiPSC-CMs cultured for 30 - 32 days and then cryopreserved; patch clamp recordings of APs and currents were performed on hiPSC-CMs 4 - 21 days post-thaw [17]. For each of these currents (i) we found a basic fitting for the available data by simulating the same voltage clamp protocols used during the experiments (Fig. 3.1 and 3.2) and (ii) since recordings were obtained from a mixture of ventricular-like, atrial-like and nodal-like hiPSC-CMs we scaled the basic fitting parameters to take into account the phenotypical heterogeneity affecting the voltage clamp data. Formulation for the remaining membrane and sarcoplasmic reticulum (SR) currents, as well as parameters not directly derivable from Ma *et al.* [17], were adapted from a previous model of hESC-CM [19] and scaled in case of known differences between ventricular and atrial cells. The differences in current formulations between ventricular-like and atrial-like models are detailed in the following subsections and summarized in Table 3.1. All model equations and parameter values are provided in the Appendix 2 on page 181.

In control conditions, ventricular-like and atrial-like APs were simulated with $\mathrm{I_{stim}}$=0, i.e. reproducing spontaneous firing activity, as reported in Ma *et al.* [17]. The comparison between experimental and simulated APs was performed by computing the following AP morphological features (AP features): rate of spontaneous beating (F), maximum diastolic potential (MDP), peak voltage (Peak), AP amplitude (APA), maximum upstroke velocity ($\mathrm{V_{max}}$) and AP duration at different percentages of repolarization ($\mathrm{APD_{10}}$, $\mathrm{APD_{30}}$, $\mathrm{APD_{90}}$). As an additional

AP feature, the AP shape factor rappAPD defined by Ma *et al.* [17] as

$$rappAPD = \frac{\mathrm{APD}_{30} - \mathrm{APD}_{40}}{\mathrm{APD}_{70} - \mathrm{APD}_{80}}$$

was included in Table 3.2: this feature represents a threshold for discriminating among ventricular-like and atrial-like hiPSC-CMs.

3.2.2 Fast sodium current ($\mathbf{I_{Na}}$)

Our I_{Na} formulation is based on the I/V, activation (G/G_{max}) and inactivation (I/I_{max}) curves measured by Ma *et al.* [17] at 35-37°C (basic fittings in Fig. 3.1a and 3.1b). To discriminate between the ventricular-like and atrial-like phenotypes we referred to Li *et al.* [20]: in particular we took into account the higher current density in the atrial phenotype with respect to the ventricular one by choosing the ratio $G_{\mathrm{Namax,ventricular\text{-}like}}/G_{\mathrm{Namax,atrial\text{-}like}} \simeq 0.6$. This was implemented by scaling the basic current conductance by 0.65 for the ventricular-like and by 1.1 for the atrial-like model.

3.2.3 L-type calcium current ($\mathbf{I_{CaL}}$)

The voltage clamp I_{CaL} recordings (I/V, activation and inactivation curves) reported by Ma *et al.* [17] were performed at room temperature; the basic fittings are reported in Fig. 3.1c and 3.1d. I_{CaL} voltage-dependent gate time constants are based on the TenTusscher model [21] , and on Grandi *et al.* [22] ,while the Ca^{2+}-dependent gate time constant is based on our hESC-CM model [19] . Before integrating the I_{CaL} formulation into the models, time constants were scaled considering a Q_{10} factor of 2.1 [7]. We considered the differences in the activation and inactivation curves reported in Camara *et al.* [23] between the ventricular and atrial phenotypes, in particular the half-voltages of the steady-state activation and voltage-dependent inactivation for the atrial-like I_{CaL} were slightly shifted by 3.1 mV and 0.8 mV, respectively, towards positive potentials. Moreover, the voltage-dependent fast inactivation time constant was doubled in the atrial-like model with respect to the ventricular-like one. No differences in current density were taken into account since Camara *et al.* [23] reported current data only, without considering the greater ventricular than atrial myocyte membrane capacitance [8]; moreover Hatano *et al.* [24] did not found any significant difference in the specific I_{CaL} density.

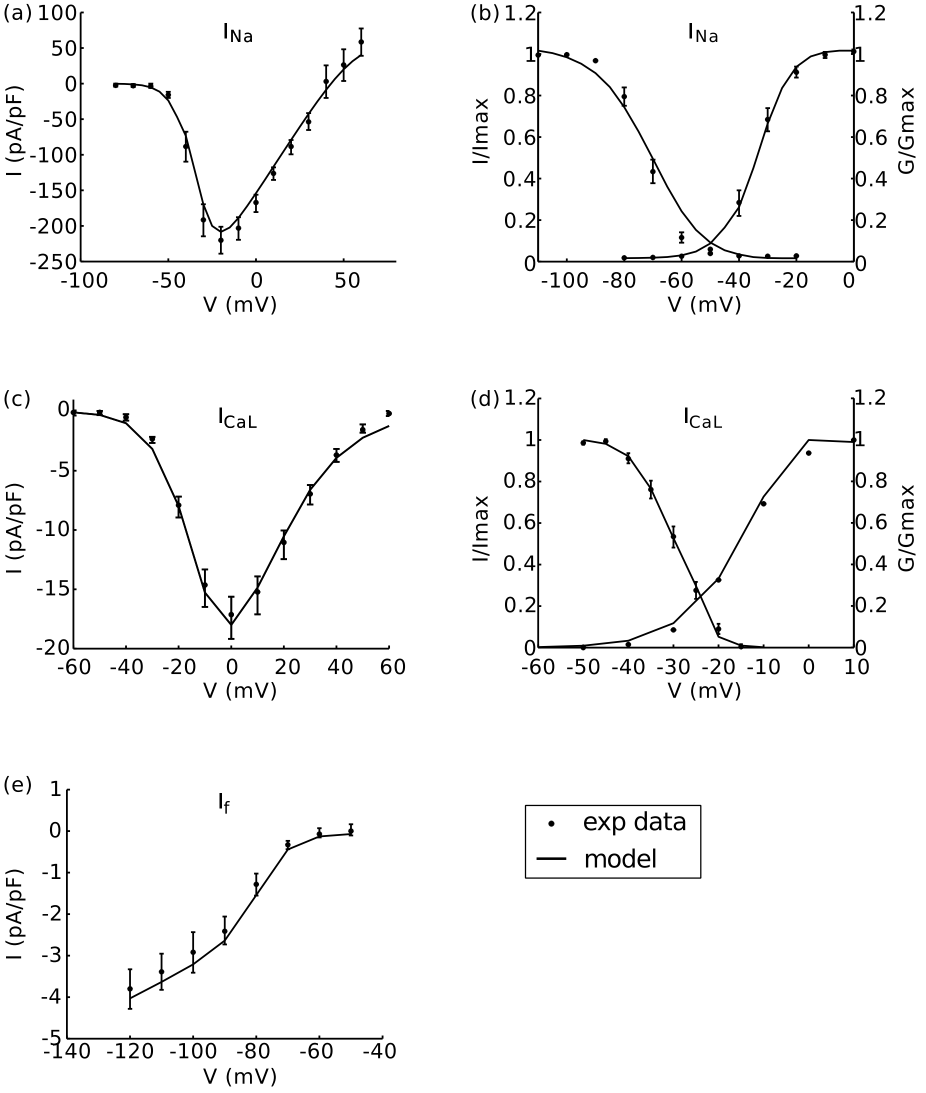

Figure 3.1: Basic fitting of the characteristics of I_{Na}, I_{CaL} and I_f; all the experimental data from Ma *et al.* [17]. (a) Peak I_{Na} I/V curve. (b) I_{Na} steady state activation and inactivation curves. (c) Peak I_{CaL} I/V curve. (d) I_{CaL} steady state activation and inactivation curves. (e) Peak I_f I/V curve.

3.2.4 Hyperpolarization-activated Cyclic Nucleotide-gated funny current (I_f)

The basic fitting of I_f is shown in Fig. 3.1e; in the ventricular-like and atrial-like models I_f was scaled to take into account also the presence of nodal-like cells in the recorded samples. Since nodal cells show a stronger expression of I_f than ventricular and atrial myocytes [25] we scaled the maximum I_f conductance by 0.7 both for the ventricular-like and atrial-like phenotypes.

3.2.5 Transient outward (I_{to}), rapid and slow delayed rectifier (I_{Kr}, I_{Ks}) currents

The basic fitting of the I_{to} current density is shown in Fig. 3.2a. The main difference we considered between the ventricular-like and atrial-like I_{to} currents was the greater outward current reported by Amos *et al.* [26] in human atrial cells: thus we considered the ratio $G_{\text{tomax,ventricular-like}}/G_{\text{tomax,atrial-like}}=0.5$.
The basic fitting of the two delayed rectifier currents I_{Kr} and I_{Ks} are reported in Fig. 3.2b, 3.2c and 3.2d. No significant differences between the ventricular and atrial phenotype were found in literature.

3.2.6 Inward rectifier current (I_{K1})

I_{K1} was formulated as in [7, 19] and it is characterized by one time-independent inactivation gate. I_{K1} data from Ma *et al.* [17] were reproduced using the same experimental voltage ramp protocol and reported in Fig. 3.2d. As reported in Amos *et al.* [26] and Schram *et al.* [27] ventricular cells in guinea pig and human show a greater I_{K1} than atrial cells. We scaled the basic I_{K1} fitting by 1.1 for the ventricular-like and by 0.66 for the atrial-like phenotype.

3.2.7 Sodium calcium exchanger (I_{NaCa}), sodium potassium pump (I_{NaK}) , sarcolemmal calcium pump (I_{pCa}) and SR currents

For I_{NaCa}, I_{NaK}, I_{pCa} and SR currents no data were available in Ma *et al.* [17], so we based their formulations on our previous model of hESC-CM, optimizing them to get the best AP shape. In particular, we referred to Wang *et al.* [28] for the I_{NaCa} and I_{NaK} differences between ventricular and atrial cells.

3.2.8 Membrane capacity and volumes

The mean membrane capacity from Ma *et al.* [17] of 88.7 pF was scaled according to Grandi *et al.* [8] to reproduce a greater capacitance for the ventricular-like than for the atrial-like hiPSC-CMs. In detail, the ventricular-like and atrial-like hiPSC-CM capacities were set to 98.716 pF and 78.662 pF thus reproducing the capacity ratio of 0.7976. The cellular volumes were scaled accordingly (see Table 3.1).

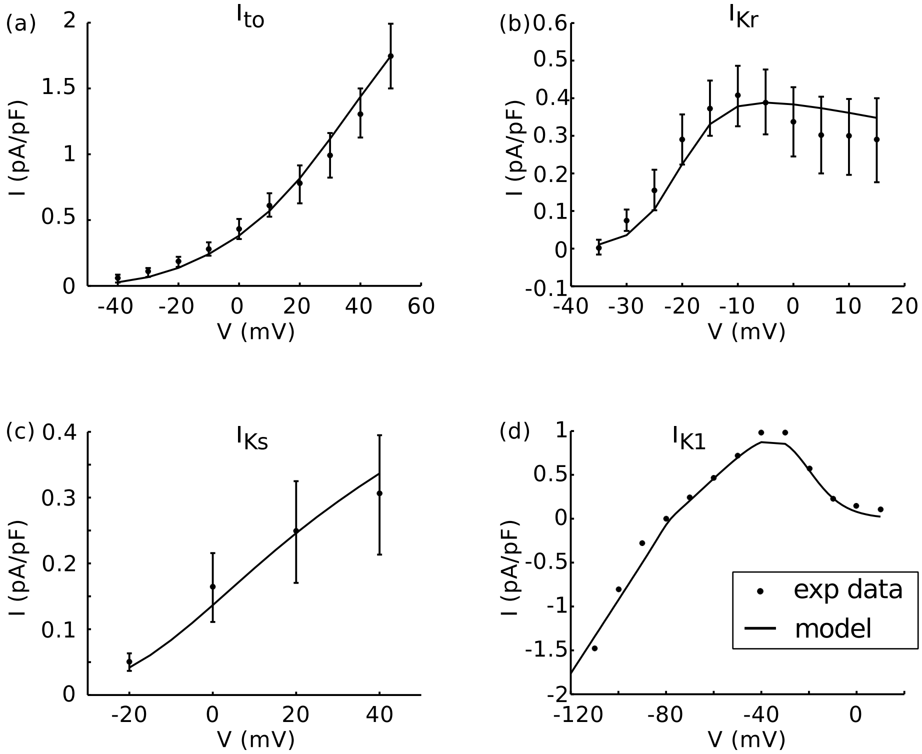

Figure 3.2: Basic fitting of the I/V curves of (a) I_{to}, (b) I_{Kr}, (c) I_{Ks} and (d) I_{K1}; all the experimental data from Ma *et al.* [17].

Table 3.1: Differences between the ventricular-like and atrial-like hiPSC-CM models. Comparison of the parameters changing between the ventricular-like and atrial-like models. $G_{\mathrm{Na,bas}}$, $G_{\mathrm{f,bas}}$, $G_{\mathrm{to,bas}}$, $G_{\mathrm{K1,bas}}$: maximum conductances in the basic fitting. $Vh_{\mathrm{d,bas}}$, $Vh_{\mathrm{f,bas}}$, $Vh_{\mathrm{f2,bas}}$: half potentials of the voltage dependent activation and inactivation gates of I_{CaL}. τ_{f2} : time constant of the fast voltage-dependent inactivation of I_{CaL}; $C_{\mathrm{m,bas}}$: mean membrane capacitance. $I_{\mathrm{NaCaMax,ventr}}$, $I_{\mathrm{NaKMax,ventr}}$: maximum current in the ventricular-like model. $I_{\mathrm{upMax,ventr}}$, $I_{\mathrm{relMax,ventr}}$: maximum fluxes in the ventricular-like model. V_{c} , V_{SR}: cellular and SR volumes. GP: guinea pig. H: human. †: values optimized to reproduce the best AP shape. !: scaled coherently with the Cm.

	basic fitting, data from Ma *et al.* 14	Ventricular-like	Atrial-like	units	Ref.
I_{Na}	$G_{\mathrm{Na,bas}}$= 6212.6	0.65*$G_{\mathrm{Na,bas}}$= 4070.1	1.1*$G_{\mathrm{Na,bas}}$= 6887.8	S/F	GP [20]
I_{CaL}	$Vh_{\mathrm{d,bas}}$= -9.1	$Vh_{\mathrm{d,bas}}$= -9.1	$Vh_{d,bas}$+3.114= -5.986	mV	GP [23]
	$Vh_{\mathrm{f,bas}}$= -26	$Vh_{\mathrm{f,bas}}$= -26	$Vh_{\mathrm{f,bas}}$+0.774= -25.226	mV	GP [23]
	$Vh_{\mathrm{f2,bas}}$= -32	$Vh_{\mathrm{f2,bas}}$= -32	$Vh_{\mathrm{f2,bas}}$+0.774= -31.226	mV	GP [23]
	$\tau_{\mathrm{f2,bas}}$	$\tau_{\mathrm{f2,bas}}$	2*$\tau_{\mathrm{f2,bas}}$	ms	†
I_{f}	$G_{\mathrm{f,bas}}$= 57.118	0.7*$G_{\mathrm{f,bas}}$= 39.99	0.7*$G_{\mathrm{f,bas}}$= 39.99	S/F	H [25]
I_{to}	$G_{\mathrm{to,bas}}$= 59.81	0.5*$G_{\mathrm{to,bas}}$= 29.9	1*$G_{\mathrm{to,bas}}$= 59.81	S/F	H [26]
I_{K1}	$G_{\mathrm{K1,bas}}$= 25.59	1.1*$G_{\mathrm{K1,bas}}$= 28.15	0.66*$G_{\mathrm{K1,bas}}$= 16.89	S/F	H [26]
Cm	$C_{\mathrm{m,bas}}$= 88.7	1.113*$C_{\mathrm{m,bas}}$= 98.716	0.887*$C_{\mathrm{m,bas}}$= 78.662	pF	H [8]
I_{NaCa}	-	$I_{\mathrm{NaCaMax,ventr}}$= 6125	0.35*$I_{\mathrm{NaCaMax,ventr}}$= 2143.8	A/F	H [28]
I_{NaK}	-	$I_{\mathrm{NaKMax,ventr}}$= 1.0896	0.8*$I_{\mathrm{NaKMax,ventr}}$= 0.8717	A/F	H [28]

	basic fitting, data from Ma *et al.* 14	Ventricular-like	Atrial-like	units	Ref.
I_{up}	-	$I_{upMax,ventr}$= 1.4016	0.2564*$I_{upMax,ventr}$= 0.3594	mM/s	†
I_{rel}	-	$I_{relMax,ventr}$= 1.0154	1.3514*$I_{relMax,ventr}$= 1.3722	mM/s	†
V_c	-	V_c = 8752.718	V_c = 6975.437	μm^3	!
V_{SR}	-	V_{SR} = 583.728	V_{SR} = 465.199	μm^3	!

3.2.9 Current blocker simulations

AP shape changes due to the action of current blockers were investigated on stimulated ventricular-like hiPSC-CMs as done experimentally by Ma *et al.* [17]: experiments regarded Tetrodotoxin (TTX), E4031, Nifedipine Nifed) and 3R4S-Chromanol 293B (Chr).

We simulated these experiments by reducing the maximum conductance of the current targeted by the specific blocker by 50%, 70% and 90% , thus simulating diverse blockade levels. The stimulation protocol is the same used in Ma *et al.* [17]: constant pacing rate 1 Hz with depolarizing pulses of 5 ms duration and 550 pA amplitude.

Additional simulations of current blocker effects with the atrial-like model are reported in the Appendix 2 on page 191.

3.2.10 Replacing adult currents into the ventricular-like hiPSC-CM model

We implemented I_{Na}, I_{to}, I_{CaL}, I_{K1}, I_{Kr} and I_{Ks} from the O'Hara-Rudy (ORd) adult ventricular cell model [6] to test their effects on the ventricular-like AP if used to replace the original hiPSC-CM currents. Since there is no data on the Ca^{2+} /calmodulin-dependent protein kinase II (CaMK) mechanism acting on the membrane currents in hiPSC-CMs, we did not implemented the CaMK part for the ORd formulations of I_{Na}, I_{to} and I_{CaL}.

Our tests were performed by simulating the AP after replacing each adult current, one by one, into the ventricular-like hiPSC-CM model. Two more tests were done: (i) since in adult ventricular cells no functional I_f is found in physiological conditions, we set to 0 the maximum I_f conductance and (ii) finally we put the adult currents all together into the ventricular model, with I_f=0.

3.3 Results

3.3.1 Spontaneous Action potentials.

Simulated traces of the spontaneous ventricular-like and atrial-like APs, are reported in Fig. 3.3a and 3.3c, respectively. Qualitative comparison with representative experimental AP profiles reported in Fig. 3.3b and 3.3d shows that simulated APs mimic experimental recordings of both the phenotypes. Experimental traces from Ma *et al.* [17].

A quantitative comparison between the experimental and simulated APs is reported in Table 3.2 in terms of the AP features detailed in the Materials and Methods section. Our models reproduced the main differences between the ventricular-like and atrial-like hiPSC-CMs reported by Ma *et al.* [17]: (i) greater frequency (shorter interval) of firing for the atrial-like model; (ii) longer APD and greater APA and MDP for the ventricular-like model; (iii) rappAPD respectively greater and smaller than the threshold value of 1.5 for the ventricular-like and atrial-like models. The membrane currents generating and shaping the AP, and the intracellular ionic concentrations are also reported in Fig. 3.4 and 3.5.

3.3.2 Current blocker simulations

Simulation of the effects of current blockers, by using the ventricular-like model, is shown in Fig. 3.6 together with a qualitative comparison between the AP changes observed in our simulations and recorded during Ma *et al.* [17] experiments. We also report in Table 3.3 the effects of blockers for all the conditions in which the AP features, resulted significantly affected in the experiments. The comparison is still qualitative, since we did not select our maximum conductance reductions based on the dose-response characteristics of each blocker. TTX acts on I_{Na}, the main responsible of the upstroke, thus a strong TTX-induced blockade produces an important shift in time of the AP peak (Fig. 3.6a), making the I_{CaL} contribution to the upstroke critical. The main influence of I_{Na} and its blockade is on the V_{max}, since by blocking the 90% of I_{Na}, V_{max} is dramatically reduced by 83%. The I_{CaL} role in sustaining the AP plateau is highlighted by the experiments and simulations about Nifed, which causes the reduction of all the APDs

(Table 3.3) and triangulates the AP profile (Fig. 3.6b). E4031 blocks selectively I_{Kr}, thus lengthening prevalently the APD (Table 3.3 and Fig. 3.6c). Finally, simulations of the I_{Ks} blocker Chr show that it only induces a small prolongation of the APD (Table 3.3 and Fig. 3.6d). All the simulation results were consistent with the experimental ones. In Appendix 2 on page 191, additional simulations of current blocker effects on the atrial-like AP shape are reported. These results are consistent with those detailed in this section.

Table 3.2: Comparison between spontaneously beating ventricular-like and atrial-like hiPSC-CM AP morphological features. Experimental and simulated AP features for the ventricular-like and atrial-like models. †: in Ma *et al.* [17] no frequencies were reported, but intervals; for an easier comprehension we converted the interval data also in frequency. $^!$: rappAPD<1.5: atrial-like, rappAPD>1.5: ventricular-like.

AP feature	units	Ventricular-like		Atrial-like	
		EXP	SIM	EXP	SIM
Cycle Length	s	1.7±0.1	1.79	1.2±0.2	1.04
F†	bpm	35.3±2.2	36.2	50±10	57.9
MDP	mV	-75.6±1.2	76.7	-73.5±1.5	-72.5
Peak	mV	28.3±1.0	28.0	26.7±1.4	26.3
APA	mV	104.0±1.1	104.7	100.2±2.1	98.7
V_{max}	V/s	27.8±4.8	27.8	26.2±3.9	26.6
APD_{10}	ms	74.1±4.8	53.3	60.8±5.5	57.2
APD_{30}	ms	180.0±10.7	235.8	123.1±10.3	133.2
APD_{90}	ms	414.7±21.8	404.7	286.2±21.2	284.5
rappAPD$^!$	-	2.5±0.2 (>1.5)	3.43	1.1±0.1 (<1.5)	1.15

3.3.3 Moving towards the adult ventricular cell by inserting adult membrane currents.

The aim of this last simulation study is the analysis of the current-based differences between ventricular-like hiPSC-CMs and adult ventricular CMs which have the greatest influence in moving the ventricular-like AP towards the adult one. In order to investigate the role of the membrane currents in determining the immature phenotype of hiPSC-CMs we compared the main currents (I_{Na},

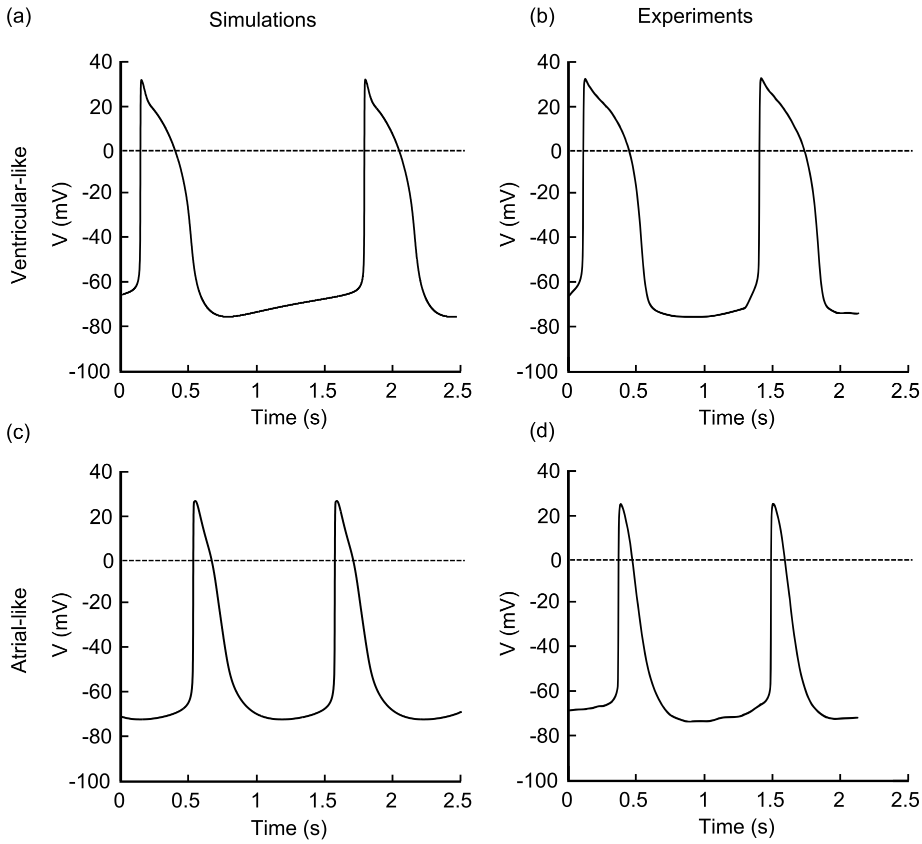

Figure 3.3: Simulated and experimental spontaneous AP traces for (a,b) the ventricular-like and (c,d) the atrial-like models. Experimental traces (b) and (d) were taken from Ma *et al.* [17]. Both experiments and simulations are reported in the same scale for comparison. No external stimulation was used ($I_{stim} = 0$).

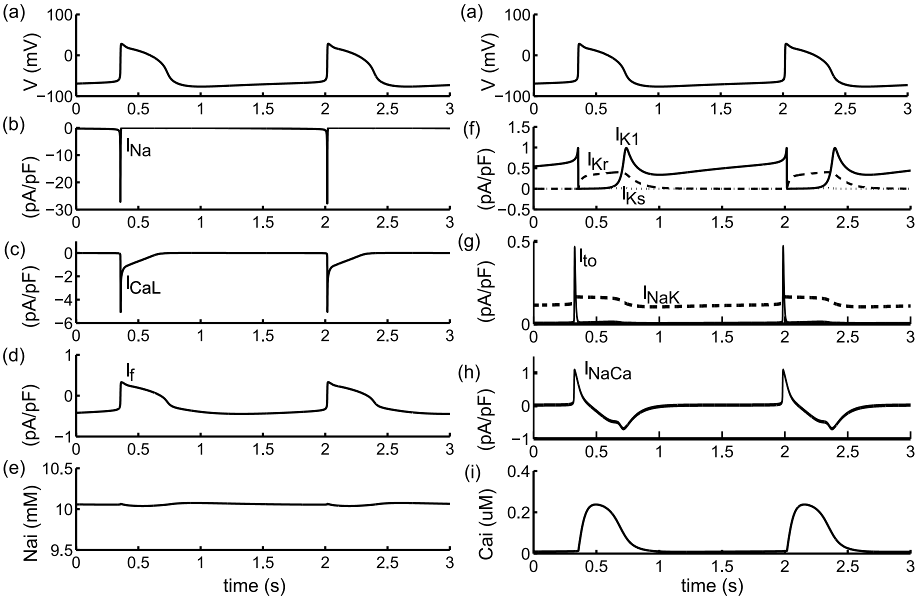

Figure 3.4: Ventricular-like steady state spontaneous AP, ionic currents and concentrations. No external stimulation was used ($I_{stim} = 0$). (a) membrane potential. (b) I_{Na}. (c) I_{CaL}. (d) I_f. (e) intracellular Na^+ concentration. (f) I_{K1}, I_{Kr} and I_{Ks}. (g) I_{to} and I_{NaK}. (h) I_{NaCa}. (i) intracellular Ca^{2+} concentration.

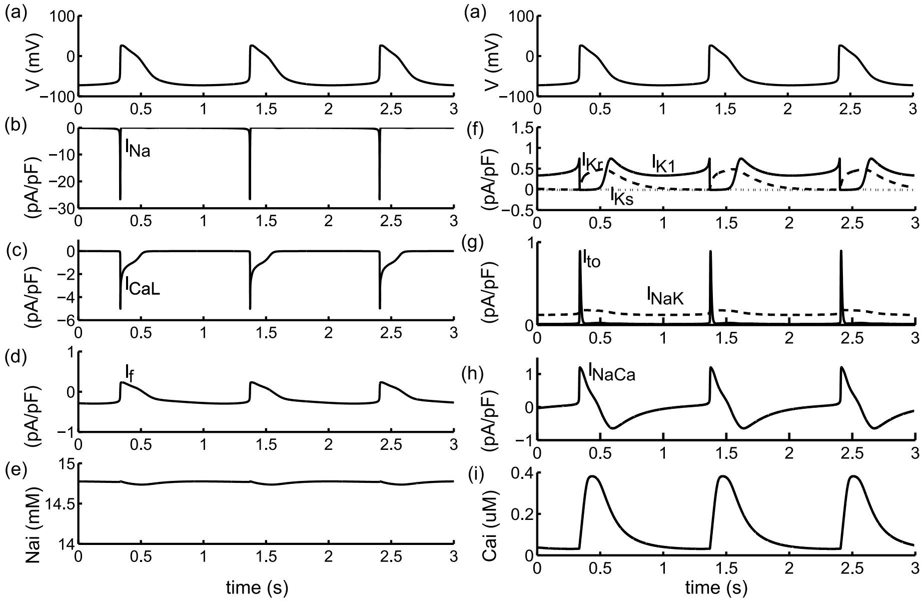

Figure 3.5: Atrial-like steady state spontaneous AP, ionic currents and concentrations. No external stimulation was used ($I_{stim} = 0$). (a) membrane potential. (b) I_{Na}. (c) I_{CaL}. (d) I_f. (e) intracellular Na^+ concentration. (f) I_{K1}, I_{Kr} and I_{Ks}. (g) I_{to} and I_{NaK}. (h) I_{NaCa}. (i) intracellular Ca^{2+} concentration.

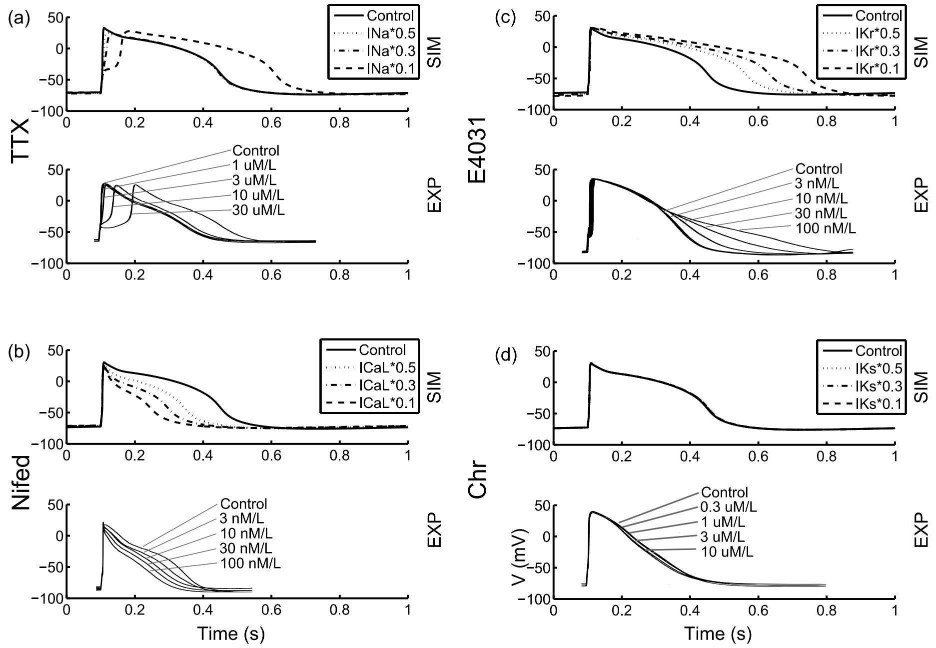

Figure 3.6: Simulated and experimental traces of stimulated APs (I_{stim} = 550 pA) under effect of prototypical current blockers. Experimental traces were taken from Ma *et al.* [17]. (a) TTX acts on I_{Na}, producing an important shift in time of the AP peak, (b) Nifed blocks I_{CaL} and causes the reduction of all the APDs and triangulates the AP profile. (c) E4031 blocks selectively I_{Kr} lengthening prevalently the APD. (d) I_{Ks} blocker Chr does not have any significant effect on the AP shape.

Table 3.3: Quantification of the effects of current blockers on the simulated action potentials and comparison with experimental data. Comparison between AP changes experimentally recorded by Ma *et al.* [17] and simulated using our ventricular-like model. The stimulation protocol is the same reported in section 3.2.9. Values in the Experiments column (means ± SE) represent the % of the experimental control value. Values in the Simulations column are given as % of the simulated control values. This table is based on the significative data ($P<0.05$) reported in Ma *et al.* [17] and it aims to provide a qualitative comparison only, since we did not directly compare the real blocker concentrations with our reduction of the maximum conductances.

AP features	Experiments		Simulations	
V_{max}	TTX 3 μM	41.2±11.2	50% G_{Na}	37.48
	TTX 10 μM	16.7±1.8	30% G_{Na}	17.61
	TTX 30 μM	16.8±2.0	10% G_{Na}	16.78
APD_{50}	E4031 30 nM	109.1±3.7	30% G_{Kr}	155.05
	E4031 100 nM	113.4±3.9	10% G_{Kr}	188.33
APD_{90}	E4031 30 nM	140.3±7.6	30% G_{Kr}	147.85
	E4031 100 nM	170.4±13.6	10% G_{Kr}	174.51
APD_{50}	Nifed 3 nM	84.6±2.4	70% G_{CaL}	72.58
	Nifed 10 nM	70.3±6.1	50% G_{CaL}	64.95
	Nifed 30 nM	65.7±3.0	30% G_{CaL}	50.30
	Nifed 100 nM	45.4±4.5	10% G_{CaL}	32.97
APD_{90}	Nifed 3 nM	89.4±1.0	70% G_{CaL}	76.76
	Nifed 10 nM	78.4±4.4	50% G_{CaL}	71.16
	Nifed 30 nM	74.0±2.3	30% G_{CaL}	61.83
	Nifed 100 nM	58.2±5.4	10% G_{CaL}	49.13

I_{to}, I_{CaL}, I_{K1}, I_{Kr} and I_{Ks}) in our hiPSC-CM ventricular-like model with their corresponding adult version, as formulated in the ORd model [6] of the adult ventricular AP (Fig. 3.7).Then, we simulated the substitution into our hiPSC-CM ventricular-like model of each individual currents with the adult one.

The I/V curve for the adult I_{Na} (Fig. 3.7a) results to be pretty similar to our ventricular-like I_{Na} but insertion of the adult I_{Na} into our hiPSC-CM ventricular-like model results in a stop of the spontaneous firing, which is not shown by adult myocytes. This result can be ascribed to the fact that the adult steady state activation, as described in the ORd model [6], is shifted towards positive potentials by 7.6 mV with respect to the hiPSC-CM one. Because of this difference the partial diastolic depolarization is not sufficient to reach the potential at which the I_{Na} activation can elicit the AP upstroke. In case of external stimulation of the hiPSC-CM model with the adult I_{Na} the AP basically overlaps the spontaneous hiPSC-CM AP (see the first AP in Fig. 3.8a). The adult I_{CaL} (Fig. 3.7b) I/V is shifted towards positive potentials with respect to our venticular-like formulation, due to steepest and positively shifted steady-state activation (by ~5 mV, not shown): its replacement into our model resulted into a deep shortening of the AP, which also translated into a shortening of the cycle length of the spontaneous beating (Fig. 3.8b). The adult I_{Ks} (Fig. 3.7c) and I_{to} (Fig. 3.7d) resulted rather similar to our currents and their effects on the AP shape are negligible (not shown). The adult I_{Kr} I/V curve was quite different than ours (Fig. 3.7e), in particular it is significantly smaller for negative potential steps and greater than our I_{Kr} for positive potentials. Its main effect is a shorter APD (Fig. 3.8c). The I/V curve for I_{K1} (Fig. 3.7f) shows basically the same peak amplitude, but the peak itself is negatively shifted by about 38 mV. The strongly smaller I_{K1} for potentials greater than -60 mV affected dramatically the AP shape, letting some early afterdepolarizations (EADs) arise (Fig. 3.8d). As for the spontaneous firing phenomenon, also the I_f current is distinctive of the immature myocytes and it disappears during maturation [10]. So we tested the effect of I_f removal from the ventricular-like model, which resulted in the stop of the spontaneous beating and a stable potential of -87 mV. In case of no I_f, by providing an external stimulus to the model, the global shape of the AP is still close to the shape of the spontaneous AP but the MDP is much more negative (Fig. 3.8e). The last test aimed to asses the effects of all the adult membrane currents (plus I_f removal) combined together into our model, without changing the membrane capacity, the subcellular compartimentalization and calcium handling. A stimulus current of

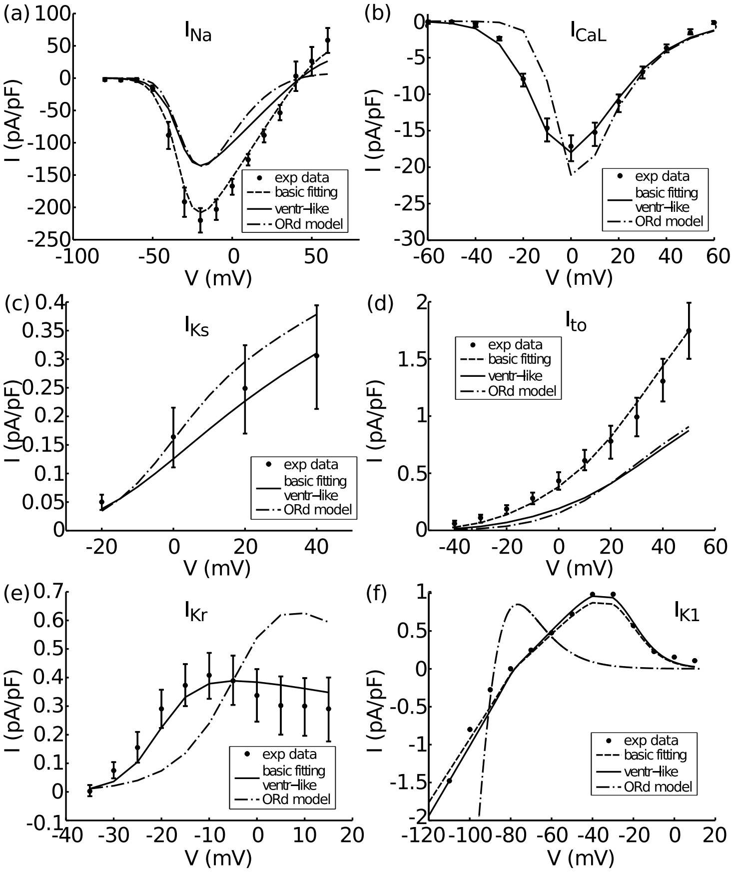

Figure 3.7: Comparison of the major ionic currents between the the experimental data from the mixed phenotyped hiPSC-CMs by Ma *et al.* [17] (dots) their basic fitting (dashed line), our ventricular-like model (solid line) and the ORd model of adult human ventricular myocyte (dash dotted line). If no dashed line is reported, ventricular-like data correspond to basic fitting data. (a) ORd I_{Na} I/V curve is similar to our ventricular-like I_{Na} but its intensity is smaller in the ranges [-60, -40] and [-10 40] mV. (b) ORd I_{CaL} I/V curve is smaller than ours for potential steps smaller than 0 mV and it is greater than ours for voltages greter than 0 mV. (c) ORd I_{Ks} and (d) ORd I_{to} I/V curves are rather similar to ours. (e) ORd I_{Kr} I/V curve was quite different than ours, in particular ORd I_{Kr} is significantly smaller for negative potential steps and greater than our I_{Kr} or positive potential steps. (f) The I/V curve for I_{K1} shows basically the same peak amplitude, but the peak itself is negatively shifted by about 38 mV.

1500 pA was used to elicit the APs, since no spontaneous beating was observed. With respect to our hiPSC-CM ventricular-like model, this hybrid model showed an AP morphology (Fig. 3.8f) closer to the ORd adult ventricular AP (our hybrid model vs ORd model): (i) resting potential -88.8 vs -88 mV, (ii) Peak 49 vs 42 mV, (iii) $\mathrm{APD}_{70}/\mathrm{APD}_{90}$ 200/233 vs 255/275 ms.

3.4 Discussion

The major aim of our work consisted in developing a hiPSC-CM model focused on the electrophysiological characteristics shown by these cells. Since the first pluripotency induction protocols on human adult cells were published [11, 12], the interest in hiPSCs culturing, production and application grew rapidly due to some clear practical advantages with respect to hESCs. In particular the patient-specificity of hiPSCs can be exploited for patient-specific drug development, since hiPSCs carry the same genetic mutations of the donor, as reported in Yazawa *et al.* [29] and Matsa *et al.* [16] for the illustrative Timothy and LQT syndromes respectively. In this framework, we applied for the first time to hiPSC-CMs the mathematical and computational approach to describe their fundamental electrophysiology. A previous model of hiPSC-CM was recently published by Zhang *et al.* [30] in order to study how to compensate the LQT1 induced APD lengthening observed in hiPSC-CMs. Their approach started from the TenTusscher 2004 model [7] were they introduced I_{NaL} and I_f and changed the maximal conductances of I_{CaL}, I_{K1} and I_{Kr}. In spite of the valuable simulations this model provided, the revised values of the TenTusscher model were assigned artificially to achieve a closer matching between the simulated and experimental APs. We chose a different approach, starting directly from the current data characterized in Ma *et al.* [17].

Similar to human cardiac myocytes, hiPSC-CM APs have different morphologies that are usually categorized [14–16] as ventricular-like, atrial-like or nodal-like. Since the ventricular-like and the atrial-like are the most commonly observed we decided to develop two different hiPSC-CM models, using literature data to identify the ionic currents most likely contributing to differentiate the ventricular-like from the atrial-like AP. Also we tested which currents are more likely different in the ventricular-like cells with respect the adult phenotype. This was possible in simulation by developing hypothetical hybrid models of partially mature ventricular CMs.

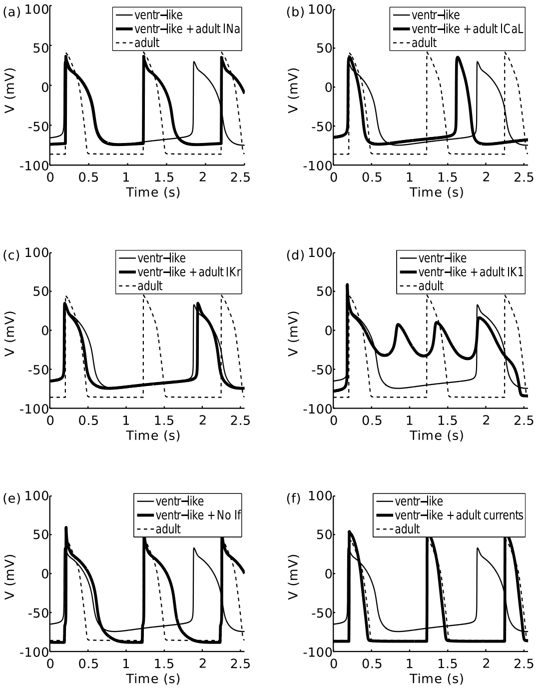

Figure 3.8: Effects of the virtual replacement of each adult ionic current into the ventricular-like model. Ventr-like: the spontaneous APs simulated by our hiPSC-CM ventricular-like model. Adult: the stimulated AP simulated by the ORd adult ventricular model. Ventr-like+adult I_{xx}: APs simulated by replacing the I_{xx} current in our ventricular-like model with its adult version. In (a), (e) and (f) external current stimulation was necessary since no spontaneous beating was produced after current substitution, whereas in (b), (c) and (d) spontaneous APs (I_{stim} = 0) are reported. (a) The adult I_{Na} stops the spontaneous APs. Under stimulation the elicited APs match the original ventricular-like APs. (b) Adult I_{CaL} inclusion into our model results into a shortened APD and a greater frequency of spontaneous beating and APA. (c) I_{Kr} inclusion induces a shortening of the APD. (d) The major effect of using adult I_{K1} is the onset of EADs in case of I_{stim} = 0. By doubling the adult I_{K1} conductance, the spontaneous beating stops and under stimulation no more EADs appear. (e) Absence of I_f stops the spontaneous APs. Under stimulation MDP moves towards the adult MDP. (f) Replacement of I_{Na}, I_{CaL}, I_{to}, I_{Kr}, I_{Ks} and I_{K1} with their adult versions and I_f = 0. Since the model does not show spontaneous APs, it is stimulated by I_{stim} = 1500 pA the AP morphology moves closer to the adult ventricular AP: resting potential -88.8 vs -88 mV, Peak 49 vs 42 mV, APD_{70}/APD_{90} 200/233 vs 255/275 ms.

Our models were validated against the available experimental data ranging over the spontaneously produced APs and the effects of current blockers on the AP shape under an external stimulus. The comparison between the experimental and simulated AP features reported in Table 3.2 shows how the two models are matching the real APs. In particular both the ventricular-like and the atrial-like models match the experimental rate of spontaneous beating, MDP, V_{max}, APA, Peak, APD_{90} and can be correctly classified based on the threshold rappAPD=1.5. The only relevant discrepancy can be found in the ventricular-like model where APD_{10} and APD_{30} don't match their experimental values: especially the simulated APD_{30} is about 50 ms longer than the experimental one. The mismatching in rappAPD is thus attributable to these differences in APD at the lower repolarization percentages and consequently our model is fully compliant with the discriminating rule for the ventricular-like phenotype (rappAPD $>$ 1.5). but it reproduces an AP "slightly more ventricular-like" than the ventricular-like cells do (3.43 vs 2.5 ± 0.2).

We also simulated, the effect of the prototypical current blockers tested by Ma *et al.* [17] (TTX, Nifed, E4031 and Chr), by reducing the maximum conductances of the current affected by the blocker. All our tests qualitatively agreed with the experimental data (Fig. 3.6) and the measurements on our simulated APs (Table 3.3) confirm that the model behaves accordingly to Ma *et al.* [17] measurements, which show that I_{Na}, I_{CaL} and I_{Kr} blockades affect significantly the AP shape by inducing (i) the reduction of the V_{max}, (ii) the shortening and (iii) the lengthening of the APD respectively. I_{Ks} blockade did not affect significantly the AP shape either in the experiments or in the simulations , consistently with the marginal role of the I_{Ks} current in the human cardiac AP under basal conditions (without adrenergic stimulation).

The second aim of our work consisted in using the ventricular-like model to investigate which are the differences between hiPSC-CMs and adult CMs in terms of currents and which of these differences are more relevant in order to reproduce an adult AP. In particular the most evident differences are: (i) the spontaneous firing activity, (ii) a more positive MDP, (iii) a very prolonged APD. It was thus a particular intriguing test for our model changing the main membrane currents with their adult formulations (adapted from the ORd model [6]) and see if the AP of this hybrid ventricular-like model moves closer to the adult ventricular AP.

In the adult heart only specialized cells show a spontaneous electrical activity, since this phenomenon is canceled out during maturation in ventricular and atrial cells. We were able to stop this spontaneous activity in hiPSC-CM by removing the I_f from the model, reproducing its downregulation observed during the myocyte maturation [31]: this supports the hypotesis that I_f has an important role in the automaticity of hiPSC-CMs as already observed in hESC-CMs [10]. Moreover, the arrhythmogenic power of this current should be considered when aiming to use ventricular-like hiPSC-CMs for drug testing or regenerative medicine. Another interesting observation emerging from our simulations is that the spontaneous beating in hiPSC-CMs is due to 2 combined mechanisms: a) the instability of the resting potential with the consequent slow depolarization and b) an increased excitability due to the negative shift of the I_{Na} activation. Indeed, two simulated conditions were both separately able to stop spontaneous beating: a) stabilization of resting potential by I_f current silencing (see Fig. 3.8e) (or alternatively by I_{K1} overexpression) and b) reduced excitability by positive shift of I_{Na} activation (see Fig. 3.8a).

As expected, the current affecting more the MDP resulted to be I_{K1} but, rather surprisingly, by replacing the hiPSC-CM I_{K1} with the adult ORd I_{K1}, MDP became more negative, but this did not stop completely the automaticity of the cell, rather inducing EADs as showed in Fig. 3.8c. It is often thought, even not yet proven, that increasing the quantity of I_{K1} current in these cells might be sufficient to obtain a stable adult ventricular phenotype. Our results point out that the ORd I_{K1} (Fig.3.7f), should have a doubled maximum conductance to be able to stop the spontaneous APs. In that condition, providing an external stimulus (550 pA in our tests), the model produces APs without EADs (data not shown).

I_{CaL} is known to act mainly to sustain the AP plateau. Replacing the hiPSC-CM I_{CaL} with the adult ORd I_{CaL}, which is smaller especially at the negative potentials (Fig. 3.8b), the AP shortens significantly approaching the physiological range for adult ventricular myocytes. This has to be combined with a stronger ORd I_{Kr} for positive potentials (Fig. 3.7e), which means a further APD shortening contribution.

The combination of the adult currents and the absence of I_f led to a model with no automaticity, characterized by an AP morphology similar to that observed in adult ventricular CMs (Fig. 3.8f).

One limitation of our work could appear to be the uniqueness of the data source: in fact we focused principally on the work of Ma *et al.* [17] since it was the most comprehensive report about hiPSC-CM membrane currents and APs, whereas other works, such as Matsa *et al.* [16] or Lahti *et al.* [15], focused on specific currents, especially K^+ current for the study of LQT syndromes. We justify our choice considering that the uniformity of experimental conditions and methodologies offered by a complete work like Ma *et al.* 's [17] represents a more stable basis for the development of a computational model. In conclusion, this study (i) provides two models of hiPSC-CM reproducing the ventricular-like and atrial-like spontaneous APs, (ii) shows that such models also satisfactorily reproduce the response to several current blockers and (iii) suggests a set of membrane currents that can be ascribed for (some) of the differences identified between ventricular-like hiPSC-CMs and adult ventricular cells.

Bibliography

[1] Shannon T, Wang F, Puglisi J, Weber C, Bers DM. A mathematical treatment of integrated Ca dynamics within the ventricular myocyte. Biophys J November 2004;87(5):3351–3371. ISSN 0006-3495.

[2] Faber GM, Rudy Y. Action Potential and Contractility Changes in [Na+]i Overloaded Cardiac Myocytes: A Simulation Study. Biophys J November 2008;78(5):2392–2404. ISSN 0006-3495.

[3] Hund TJ, Rudy Y. Rate dependence and regulation of action potential and calcium transient in a canine cardiac ventricular cell model. Circulation November 2004;110(20):3168–3174. ISSN 1524-4539.

[4] Carro J, Rodriguez J, Laguna P, Pueyo E. A human ventricular cell model for investigation of cardiac arrhythmias under hyperkalaemic conditions. Philos Transact A Math Phys Eng Sci November 2011;369(1954):4205–4232. ISSN 1471-2962.

[5] Grandi E, Pasqualini FS, Bers DM. A novel computational model of the human ventricular action potential and Ca transient. J Mol Cell Cardiol January 2010;48(1):112–21. ISSN 1095-8584.

[6] O'hara T, Virág L, Varró A, Rudy Y. Simulation of the Undiseased Human Cardiac Ventricular Action Potential: Model Formulation and Experimental Validation. PLoS Comput Biol May 2011;7(5):e1002061. ISSN 1553-7358.

[7] ten Tusscher KHWJ, Noble D, Noble PJ, Panfilov AV. A model for human ventricular tissue. Am J Physiol Heart Circ Physiol April 2004; 286(4):H1573–1589.

[8] Grandi E, Pandit S, Voigt N, Workman A, Dobrev D, Jalife J, Bers D. Human Atrial Action Potential and Ca2+ Model: Sinus Rhythm and Chronic Atrial Fibrillation. Circ Res October 2011;109(9):1055–1066. ISSN 1524-4571.

[9] Kehat I, Gepstein A, Spira A, Itskovitz-Eldor J, Gepstein L. High-resolution electrophysiological assessment of human embryonic stem cell-derived cardiomyocytes: a novel in vitro model for the study of conduction. Circ Res 2002;91(8):659–661.

[10] Sartiani L, Bettiol E, Stillitano F, Mugelli A, Cerbai E, Jaconi ME. Developmental changes in cardiomyocytes differentiated from human embryonic stem cells: a molecular and electrophysiological approach. Stem Cells 2007; 25(5):1136–1144.

[11] Takahashi K, Tanabe K, Ohnuki M, Narita M, Ichisaka T, Tomoda K, Yamanaka S. Induction of pluripotent stem cells from adult human fibroblasts by defined factors. Cell November 2007;131(5):861–872.

[12] Yu J, Vodyanik MA, Smuga-Otto K, Antosiewicz-Bourget J, Frane JL, Tian S, Nie J, Jonsdottir GA, Ruotti V, Stewart R, Slukvin II, Thomson JA. Induced Pluripotent Stem Cell Lines Derived from Human Somatic Cells. Science 2007;318(5858):1917–1920.

[13] Zhang J, Wilson GF, Soerens AG, Koonce CH, Yu J, Palecek SP, Thomson JA, Kamp TJ. Functional Cardiomyocytes Derived From Human Induced Pluripotent Stem Cells. Circ Res 2009;104(4):e30–41.

[14] Moretti A, Bellin M, Welling A, Jung CB, Lam JT, Bott-Flügel L, Dorn T, Goedel A, Höhnke C, Hofmann F, Seyfarth M, Sinnecker D, Schömig A, Laugwitz KL. Patient-specific induced pluripotent stem-cell models for long-QT syndrome. N Engl J Med 2010;363(15):1397–1409.

[15] Lahti AL, Kujala VJ, Chapman H, Koivisto AP, Pekkanen-Mattila M, Kerkela E, Hyttinen J, Kontula K, Swan H, Conklin BR, Yamanaka S, Silvennoinen O, Aalto-Setala K. Model for long QT syndrome type 2 using

human iPS cells demonstrates arrhythmogenic characteristics in cell culture. Dis Model Mech November 2011;5(2):220–230. ISSN 1754-8403.

[16] Matsa E, Rajamohan D, Dick E, Young L, Mellor I, Staniforth A, Denning C. Drug evaluation in cardiomyocytes derived from human induced pluripotent stem cells carrying a long QT syndrome type 2 mutation. Eur Heart J April 2011;32(8):952–962.

[17] Ma J, Guo L, Fiene S, Anson B, Thomson J, Kamp T, Kolaja K, Swanson B, January C. High purity human-induced pluripotent stem cell-derived cardiomyocytes: electrophysiological properties of action potentials and ionic currents. Am J Physiol Heart Circ Physiol November 2011;301(5):H2006–H2017.

[18] Yokoo N, Baba S, Kaichi S, Niwa A, Mima T, Doi H, Yamanaka S, Nakahata T, Heike T. The effects of cardioactive drugs on cardiomyocytes derived from human induced pluripotent stem cells. Biochem Biophys Res Commun September 2009;387(3):482–488.

[19] Paci M, Sartiani L, Lungo M, Jaconi M, Mugelli A, Cerbai E, Severi S. Mathematical modelling of the action potential of human embryonic stem cell derived cardiomyocytes. Biomed Eng Online 2012;11(1):61. ISSN 1475-925X.

[20] Li G, Lau C, Shrier A. Heterogeneity of Sodium Current in Atrial vs Epicardial Ventricular Myocytes of Adult Guinea Pig Hearts. J Mol Cell Cardiol September 2002;34(9):1185–1194.

[21] ten Tusscher KHWJ, Panfilov AV. Alternans and spiral breakup in a human ventricular tissue model. American journal of physiology Heart and circulatory physiology September 2006;291(3):H1088–100. ISSN 0363-6135.

[22] Grandi E, Pasqualini FS, Pes C, Corsi C, Zaza A, Severi S. Theoretical investigation of action potential duration dependence on extracellular Ca2+ in human cardiomyocytes. J Mol Cell Cardiol March 2009;46(3):332–342.

[23] Camara AK, Begic Z, Kwok WM, Bosnjak ZJ. Differential modulation of the cardiac L- and T-type calcium channel currents by isoflurane. Anesthesiology 2001;95(2):515–524.

[24] Hatano S, Yamashita T, Sekiguchi A, Iwasaki Y, Nakazawa K, Sagara K, Iinuma H, Aizawa T, Fu LT. Molecular and electrophysiological differences in the L-type Ca2+ channel of the atrium and ventricle of rat hearts. Circ J 2006;70(5):610–614.

[25] Accili EA, Proenza C, Baruscotti M, DiFrancesco D. From funny current to HCN channels: 20 years of excitation. News Physiol Sci February 2002; 17:32–37.

[26] Amos GJ, Wettwer E, Metzger F, Li Q, Himmel HM, Ravens U. Differences between outward currents of human atrial and subepicardial ventricular myocytes. J Physiol Lond February 1996;491 (Pt 1:31–50.

[27] Schram G, Pourrier M, Melnyk P, Nattel S. Differential Distribution of Cardiac Ion Channel Expression as a Basis for Regional Specialization in Electrical Function. Circulation Research May 2002;90(9):939–950. ISSN 00097330.

[28] Wang J, Schwinger RHG, Frank K, Müller-ehmsen J, Martin-vasallo P, Pressley TA, Xiang A, Erdmann E, Mcdonough AA. Regional Expression of Sodium Pump Subunit Isoforms and Na + -Ca ++ Exchanger in the Human Heart. The Journal of Clinical investigation 1996;98(7):1650–1658.

[29] Yazawa M, Hsueh B, Jia X, Pasca AM, Bernstein JA, Hallmayer J, Dolmetsch RE. Using induced pluripotent stem cells to investigate cardiac phenotypes in Timothy syndrome. Nature March 2011;471(7337):230–234.

[30] Zhang H, Zou B, Yu H, Moretti A, Wang X, Yan W, JJ B, Bellin M, OB M, Tomaselli G, Nan F, KL L, Li M. Modulation of hERG potassium channel gating normalizes action potential duration prolonged by dysfunctional KCNQ1 potassium channel. Proc Natl Acad Sci U S A July 2012; 109(29):11866–11871. ISSN 0027-8424.

[31] Yanagi K, Takano M, Narazaki G, Uosaki H, Hoshino T, Ishii T, Misaki T, Yamashita JK. Hyperpolarization-activated cyclic nucleotide-gated channels and T-type calcium channels confer automaticity of embryonic stem cell-derived cardiomyocytes. Stem Cells November 2007;25(11):2712–2719. ISSN 1549-4918.

Part II

Texture descriptors for processing biological images

CHAPTER

ONE

OVERVIEW ON TEXTURE DESCRIPTORS

According to the initial idea of this Ph.D. , the modelling part on hESC-CMs should have been coupled with a collateral image processing study, aimed to extract morphological and textural information related to the maturation of hESC-CMs. The final goal would have been a functional evaluation of the differentiation of hESCs towards the cardiac phenotype by morphological and electrophysiological data. However, during the Ph.D. studies, while the modelling part started focusing also on hiPSC-CMs, the characterization of the hESC maturation by means of image processing was abandoned due to the following issues with the available image dataset: (i) few hESC images; (ii) the maturation time for each cell was not recorded while building the dataset; (iii) cell morphology was affected by the adhesion to the culturing plates. Nevertheless, preliminary processings on hESC-CM and hiPSC-CM image datasets strenghtened the author's interest on texture analysis and texture descriptors and this resulted in the following independent line of research.

The importance of texture analysis as a branch of computer vision has been cleared from decades [1]: traditionally used for face recognition [2], fingerprint matching [3] and other biometric purposes, it has proven to be extremely valuable and effective in the medical and biological fields as well, e.g. polyp detection in colonoscopy images [4]. It is easy to understand the success of texture analysis since almost every image contains texture and the continuous development in image acquisition technology made high-resolution pictures available. There is not unique quantitative definition of texture, even if various qualitative explanations were published. Different attempts are reported in literature [1, 5–7] and reviewed in [8]:

- “We may regard texture as what constitutes a macroscopic region. Its structure is simply attributed to the repetitive patterns in which elements or primitives are arranged according to a placement rule.” [5]
- “A region in an image has a constant texture if a set of local statistics or other local properties of the picture function are constant, slowly varying, or approximately periodic.” [6]
- “The image texture we consider is non figurative and cellular [...] An image texture is described by the number and types of its(tonal) primitives and the spatial organization or layout of its (tonal) primitives [...] A fundamental characteristic of texture: it cannot be analyzed without a frame of reference of tonal primitive being stated or implied. For any smooth gray-tone surface, there exists a scale such that when the surface is examined, it has no texture. Then as resolution increases, it takes on a fine texture and then a coarse texture.” [1]
- “The notion of texture appears to depend upon three ingredients: (i) some local ”order” is repeated over a region which is large in comparison to the order’s size, (ii) the order consists in the non random arrangement of elementary parts, and (iii) the parts are roughly uniform entities having approximately the same dimensions everywhere within the textured region.” [7]

The essential ideas are thus: (i) the presence of repetitive primitives (patterns) having the same size everywhere in the textured region and (ii) the non-random spatial organization of patterns in a region larger in comparison with pattern size [9]. Many texture descriptors were developed, as reviewed in [10], and among this great variety we summarize the approaches used in this thesis:

- methods based on the Grey Level Co-occurence Matrix (GLCM), such as Haralick features [1] (section 1.1);

- neighborhood based methods, computed directly on the image using a shifting neighborhood (square, rectangular, circular, ...) such as Local Binary Pattern (LBP) (1.2) and its variants Local Ternary Pattern (LTP) [11] and Local Quinary Pattern (LQP) [12] (section 1.3). We include among the neighborhood based texture descriptors also the Local Phase Quantization (LPQ) [13] computed on the Fourier transform phase information extracted from the neighborhood (section 1.4).

In particular the LBP descriptor [14] achieved great success in the Computer Vision field, especially for its strength in detecting textural and structural information. In medical imaging LBP was successfully applied for several applications, eg. an automated Marsh-like scoring system for coeliac disease applied to endoscopic images [15] or mass detection in mammographic images [16]. The LBP descriptor finds application also in biology, eg. for classifying different cellular phenotypes [17].

1.1 Haralick features (HAR)

Haralick texture features [1] are calculated from the GLCM. GLCM is a square matrix with dimension N_g, where N_g represents the number of grey level in the image. Each element (i, j) represents the number of times an element of intensity i is adjacent, considering a distance of d pixels, to a pixel of intensity j, normalized by the total amount of the comparison made in order to have each $p(i, j)$ in the $[0, 1]$ range

$$\mathbf{G} = \begin{bmatrix} p(1,1) & p(1,2) & \cdots & p(1,N_g) \\ p(2,1) & p(2,2) & \cdots & p(2,N_g) \\ \vdots & \vdots & \ddots & \vdots \\ p(N_g,1) & p(N_g,2) & \cdots & p(N_g,N_g) \end{bmatrix} \tag{1.1}$$

Since four different adjacency angles $\theta = \{0°, 45°, 90°, 135°\}$ can be used, four different GLCMs can be calculated (Fig. 1.1). From each GLCM 13 features can be extracted, thus having 52 features computed along the four directions depicted in Fig. 1.1. Here we report just some of them to provide the main idea behind these features (see Fig. 1.2 the complete formulation of the whole feature set is available in [1]):

- Angular Second Moment (ASM) is a measurement of the homogeneity of

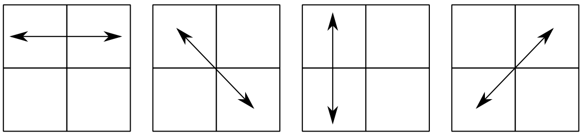

Figure 1.1: The four adjacency directions for GLCMs with distance $d = 1$.

the image. It helps quantify the distribution of values in the GLCM. In a homogeneous image there are few dominant gray-tone transitions thus the GLCM will have few elements of large magnitude and the ASM will be larger. On the contrary, for a non-homogeneus image the GLCM will contain a large number of small elements and the ASM will be smaller.

$$\sum_{i=0}^{N_g-1}\sum_{j=0}^{N_g-1} p(i,j)^2 \tag{1.2}$$

- Contrast is a measure of the amount of local variation present in the image.

$$\sum_{n=0}^{N_g-1} n^2\{\sum_{i=1}^{N_g}\sum_{j=1}^{N_g} p(i,j)\},\ |i-j| = n \tag{1.3}$$

- Correlation measures the linear-dependece of gray-tones in the image. A high correlation value indicates that the pixels in an image have similar tonal values [18].

$$\frac{1}{\sigma_x\sigma_y}\sum_{i=0}^{N_g-1}\sum_{j=0}^{N_g-1}(i-\mu_x)(j-\mu_y)p(i,j) \tag{1.4}$$

where

$$\mu_x = \sum_{i=0}^{N_g-1} ip_x(i) \tag{1.5}$$

$$\mu_y = \sum_{j=0}^{N_g-1} jp_y(i) \tag{1.6}$$

$$\sigma_x^2 = \sum_{i=0}^{N_g-1} (i - \mu_x)^2 p_x(i) \tag{1.7}$$

$$\sigma_y^2 = \sum_{j=0}^{N_g-1} (j - \mu_y)^2 p_y(i) \tag{1.8}$$

and p_x, p_y are the marginal distribution associated with $p(i,j)$.

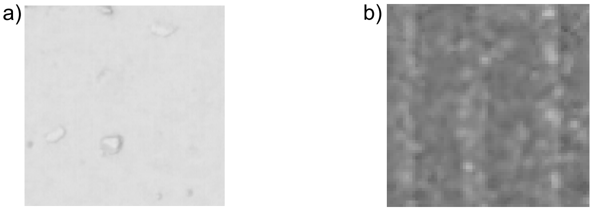

Angle	ASM	Contrast	Correlation	ASM	Contrast	Correlation
0°	0.9869	0.0053	0.3156	0.2540	0.4403	0.1882
45°	0.9870	0.0058	0.2033	0.2480	0.4902	0.0965
90°	0.9887	0.0040	0.4512	0.2693	0.3658	0.3227
135°	0.9868	0.0059	0.2036	0.2480	0.4794	0.1163

Figure 1.2: Haralick textural features for two different category images. Due to its non-homogeneity Fig. 1.2b has a lower ASM than Fig. 1.2a. Since there is a large amount of local variation in Fig. 1.2b than in Fig. 1.2a, the first one has a greater contrast value. For both the images, the correlation features is higher in the vertical 90° direction; especially 1.2b shows defined structures along the 90° direction, thus having a higher correlation along this line. Figure 1.2a and 1.2b from the from the Bonn BTF (2003) database. Available online at http://cg.cs.uni-bonn.de/en/projects/btfdbb/download/.

1.2 Local Binary Pattern (LBP)

The LBP operator [14] has become one of the most appreciated and useful texture operators in the literature due to its high descriptive power and its invariance to local grayscale variations. The basic LBP assumption is that an image is constituted by micropatterns.

1.2.1 Basic formulation

In its original form, the LBP operator is defined as a label for each pixel in the image on the basis of a circular neighborhood of P pixels of grey level q_p and radius R around the central pixel of gray value q_c, as follows:

$$LBP(P,R) = \sum_{p=0}^{P-1} s(q_p - q_c)2^p \tag{1.9}$$

where

$$s(x) = \begin{cases} 1, x \geq 0 \\ 0, x < 0 \end{cases} \tag{1.10}$$

Thus, the extracted binary codes are represented in the histogram form, useful to describe texture patterns in the studied image. Usual neighborhoods (Fig. 1.3) are based on the following (P,R) values:

- $(8,1) \rightarrow 2^8$ features;
- $(16,2) \rightarrow 2^{16}$ features;
- $(24,3) \rightarrow 2^{24}$ features;

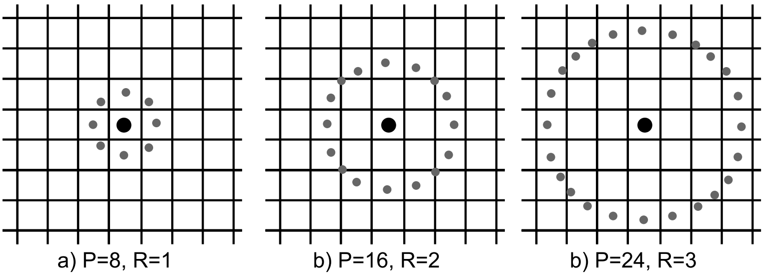
a) P=8, R=1 b) P=16, R=2 b) P=24, R=3

Figure 1.3: LBP neighborhoods for different (P,R). Central pixel in black, neighborhood pixels in grey. Figure adapted from [17].

1.2.2 Rotation invariant LBP

The basic *LBP(P,R)* operator is affected by rotation, since the gray values q_p move when the image is rotated. Values $\{q_0, ..., q_{P-1}\}$ are always taken starting from the gray value of element (0; R) to the right of q_c thus rotating a particular binary pattern results in a different *LBP(P,R)* value, except for those patterns made of only 0s (or 1s) which remain constant. In [14], a rotation invariant version of LBP, was defined:

$$LBP^{ri}(P, R) = min\{ROR(LBP(P, R), i) \mid i = 0, 1, ..., P - 1\} \tag{1.11}$$

where $ROR(x, i)$ performs a circular bit-wise right shift on the P-bit number i times. For example, in case of $P = 8$, all the pattern containing only one bit set to 1 (eg. 00000001, 00000010, 00000100, ...) are gathered under the label 00000001. The 36 unique rotation invariant LBP in case of P=8 are summarized in Table 1.1.

Table 1.1: The 36 rotation invariant LBP. Table adapted from [19].

Pattern	Index
00000000	0
00000001	1
00000011	2
00000101	3
00001001	4
···	···
01111111	34
11111111	35

1.2.3 Uniform LBP and Uniform Rotation Invariant LBP

In [14] it was observed that most of the texture information of an image, sometimes over 90 %, is provided by a small subset of the LBP patterns characterized by few spatial transitions, i.e. bitwise 0/1 changes: to reflect this property they

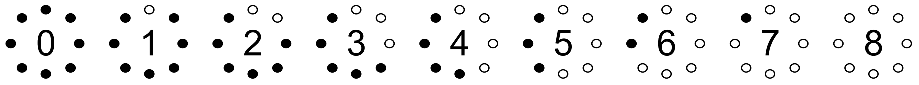

Figure 1.4: The uniform rotation invariant LBP in case of a 8 pixel-sized neighborhhod ($LBP^{riu2}(8,R)$). Black circles correspond to the 0 bit value and white circles to the 1 bit value. Figure adapted from [14].

are called "uniform". Uniformity is formalized as *U("pattern")*

$$U(LBP(P,R)) = |s(q_{P-1}-q_c)-s(q_0-q_c)|+\sum_{p=0}^{P-1} |(s(q_p-q_c)-s(q_{p-1}-q_c)| \quad (1.12)$$

and it corresponds to the occurrence of bitwise 0/1 changes in the "pattern". Fig. 1.4 reports the "uniform" patterns among the 36 rotation invariant patterns in case of neighborhood $(8,1)$. They represent templates for specific micro-features such as bright spot (0), flat area or dark spot (8), and edges of various curvatures (1-7) [14]: patterns 00000000_2 and 11111111_2 have $U = 0$, while the other seven patterns have $U = 2$ as there are exactly two 0/1 transitions in the pattern. All the other patterns in Table 1.1 have $U \geq 4$, thus they cannot be considered "uniform".

"Uniform" patterns can be selected from the basic LBP (see section 1.2.1) or from the rotation invariant LBP (LBP^{ri}, see section 1.2.2). In both cases one unique label is assigned to each "uniform" pattern, while all the other "non-uniform" patterns are gathered under one additional "miscellaneous" label.

Extraction of "uniform" patterns from the basic LBP results in $P^2-P+2+1$ labels as shown in [20], leading to the LBP^{u2} operator: for example, using the $(8,1)$ neighborhood results in 58 "uniform" patterns, thus 59 possible labels.

In [14] the "uniform" version of the rotation invariant LBP is proposed as gray-scale and rotation invariant texture descriptor and it is formalized as follows:

$$LBP^{riu2}(P,R) = \begin{cases} \sum_{p=0}^{P-1} s(q_p - q_c)2^p & \text{if } U(LBP^{ri}(P,R)) \leq 2 \\ P+1 & \text{otherwise} \end{cases} \quad (1.13)$$

In a circularly symmetric neighborhood of P pixels, only $P+1$ rotation invariant "uniform" binary patterns can be composed: a unique label (reported inside each pattern in of Fig. 1.4) is assigned to each of them corresponding to the number of "1" (white circles in Fig. 1.4) in the $\{0, 1, ..., P\}$ pattern, while the "non-uniform" patterns are grouped under the $P+1$ label, thus producing $P+2$ values. In texture analysis, the histogram of the pattern labels over a texture sample is commonly used as a feature vector (Fig. 1.5) and by using $LBP^{riu2}(P, R)$ instead of $LBP(P, R)$ or $LBP^{u2}(P, R)$ or $LBP^{ri}(P, R)$ the amount of features is dramatically reduced. For example, by considering the typical neighborhoods in Fig. 1.3, it results:

- $(8, 1) \rightarrow 10$ features;

- $(16, 2) \rightarrow 18$ features;

- $(24, 3) \rightarrow 26$ features;

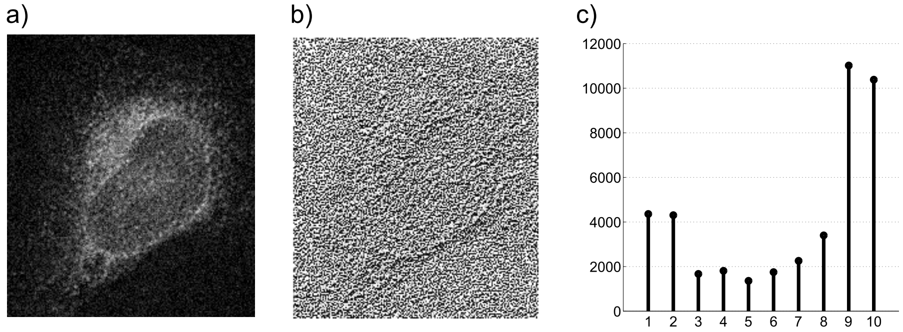

Figure 1.5: Feature extraction from the original image (a) by $LBP^{riu2}(8, 1)$, 10 features, (b) the image after the labeling by $LBP^{riu2}(8, 1)$ and (c) the resulting $LBP^{riu2}(8, 1)$ histogram (in abscissa the bin number, in ordinate the number of occurrences of the given bin). Figure 1.5a from the 2D HeLa dataset available online at http://murphylab.web.cmu.edu//data/#2DHeLa [21].

1.3 Local Ternary (LTP) and Quinary (LQP) Pattern

LTP [11] is based on the same idea of the canonical LBP but it tries to reduce its sensitivity to noise, especially in near-uniform image regions. In fact, the main weakness of the LBP operator is that the binary *s(x)* function thresholds exactly at the intensity value of the central pixel q_c. To overcome this weakness, in [11] the use of a ternary coding was proposed. The ternary coding is achieved by introducing the threshold τ in the canonical LBP *s(x)* function which becomes:

$$s(x) = \begin{cases} 1, x \geq \tau \\ 0, |x| \leq \tau \\ -1, x \leq -\tau \end{cases} \tag{1.14}$$

Due to the length of the ternary coding, the original LTP code is split into a positive and a negative LBP code (Fig. 1.6). The use of the ternary coding requires the threshold τ to be set. The threshold selection is a critical task in order to reduce the sensitivity to noise of this new operator: in [11] threshold was set manually ($\tau = 0.1$ or 0.2) and this is usually done to get the best performance in specific problems, but some automatic adaptive procedures were also proposed in [15] by exploiting local statistics such as mean value and standard deviation inside each neighborhood.

The goodness of this idea led also to the proposal of more complex codings, such as the LQP operator proposed in [12], which exploits two thresholds τ_1 and τ_2, thus allowing the *s(x)* function to assume values in [-2; -1; 0; 1; 2]:

$$s(x) = \begin{cases} 2, x \geq \tau_2 \\ 1, \tau_1 \leq x < \tau_2 \\ 0, -\tau_1 \leq x < \tau_1 \\ -1, -\tau_2 \leq x < -\tau_1 \\ -2, x < -\tau_2 \end{cases} \tag{1.15}$$

The quinary pattern is then split into four binary patterns and the histograms that are computed from these patterns are then concatenated. In case the uniform rotation invariant mapping and the typical (P, R) neighborhoods presented in section 1.2.3 are applied to LQP, it results:

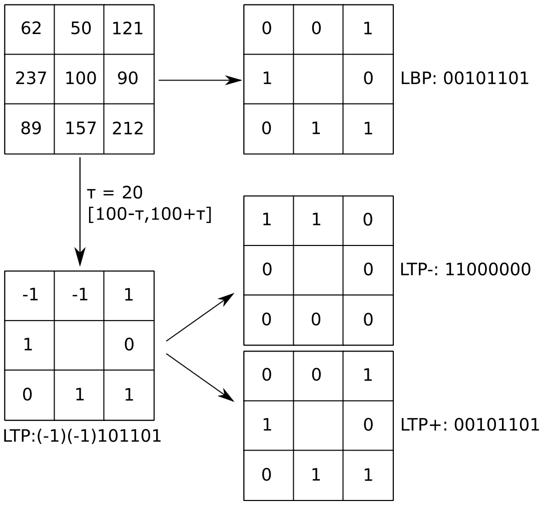

Figure 1.6: LBP vs LTP. Extraction of LBP and LTP from a typical circular 3 by 3 neighborhood. The LTP code is split into its negative (LTP_-) and positive (LTP_+) parts.

- $(8, 1) \rightarrow 40$ features;
- $(16, 2) \rightarrow 72$ features.
- $(8, 1)$ and $(16, 2) \rightarrow 112$ features;

1.4 Local Phase Quantization (LPQ)

LPQ is another important operator for analysis of textural information based on the blur invariance of the Fourier Transform Phase. In this section the basics about LPQ are reported, the full formulation is detailed in the original article of Ojansivu *et al.* [13]. The spatially invariant blurred version $g(\mathbf{x})$ of an original image $f(\mathbf{x})$ can be expressed as

$$g(\mathbf{x}) = f(\mathbf{x}) * h(\mathbf{x}) \tag{1.16}$$

where $\mathbf{x}= [x,y]^T$ represents the spatial coordinate vector and $h(\mathbf{x})$ the blur. Thus, in the Fourier space, this means

$$G(\mathbf{u}) = F(\mathbf{u}) \cdot H(\mathbf{u}) \tag{1.17}$$

where $G(\mathbf{u})$, $F(\mathbf{u})$ and $H(\mathbf{u})$ are the Fourier transformed versions of $g(\mathbf{x})$, $f(\mathbf{x})$ and $h(\mathbf{x})$ respectively while $\mathbf{u}= [u,\ v]^T$ is the frequency coordinate vector. The phase of $G(\mathbf{u})$ is expressed by

$$\angle G(\mathbf{u}) = \angle F(\mathbf{u}) + \angle H(\mathbf{u}) \tag{1.18}$$

and if the blur $h(\mathbf{x})$ is centrally symmetric $H(\mathbf{u})$ is always real-valued, thus its phase is

$$\angle H(\mathbf{u}) = \begin{cases} 0, H(\mathbf{u}) \geq 0 \\ \pi, H(\mathbf{u}) < 0 \end{cases} \tag{1.19}$$

meaning that the original and the blurred images have the same phase at those frequencies which make $H(\mathbf{u})$ positive. The LPQ operator is based on the above properties of blur invariance. It uses the local phase information extracted using the 2D Short Term Fourier Transform (STFT) computed over a square neighborhood N_x of size M by M (usually $M = 3$ or $M = 5$ pixels) at each position $\mathbf{x}$ of the image *f(*$\mathbf{x}$*)*:

$$F(\mathbf{u},\mathbf{x}) = \sum_{y \in N_x} f(\mathbf{x}-\mathbf{y})e^{-j2\pi\mathbf{u}^{\mathrm{T}}\mathbf{y}} = \mathbf{w_u}^{\mathrm{T}}\mathbf{f_x} \tag{1.20}$$

where $\mathbf{w_u}$ is the basis vector of the 2-D STFT at frequency $\mathbf{u}$, and $\mathbf{f_x}$ is a vector containing the M^2 image samples from the neighborhood N_x. Only four frequency vectors are considered: $\mathbf{u}_1 = [a,0]^T$, $\mathbf{u}_2 = [0,a]^T$, $\mathbf{u}_3 = [a,a]^T$ and $\mathbf{u}_4 = [a,\text{-}a]^T$, where the scalar frequency a is small enough to reside below the first zero crossing of $H(\mathbf{u})$ that satisfies

$$\angle G(\mathbf{u}) = \angle F(\mathbf{u}),\ \text{for all } H(\mathbf{u}) \geq 0. \tag{1.21}$$

By assigning

$$\mathbf{F}_x^c = [F(\mathbf{u}_1,\mathbf{x}), F(\mathbf{u}_2,\mathbf{x}), F(\mathbf{u}_3,\mathbf{x}), F(\mathbf{u}_4,\mathbf{x})] \tag{1.22}$$

and

$$\mathbf{F_x} = [Re\{\mathbf{F}_x^c\}, Im\{\mathbf{F}_x^c\}]^T, \tag{1.23}$$

then the corresponding 8 by M^2 transform matrix is

$$\mathbf{W} = [Re\{\mathbf{w_{u1}}, \mathbf{w_{u2}}, \mathbf{w_{u3}}, \mathbf{w_{u4}}\}, Im\{\mathbf{w_{u1}}, \mathbf{w_{u2}}, \mathbf{w_{u3}}, \mathbf{w_{u4}}\}]^T \tag{1.24}$$

and thus,

$$\mathbf{F_x} = \mathbf{W}\ \mathbf{f}_x. \tag{1.25}$$

After computing $\mathbf{F_x}$ for all the image position, the resulting vectors are quantized using the following scalar quantizer

$$q_j = \begin{cases} 1, f_j \geq 0 \\ 0, f_j < 0 \end{cases} \tag{1.26}$$

where f_j represents the j-th component of $\mathbf{F_x}$ and the quantized coefficients are transformed into integers between 0-255 by the binary coding

$$b = \sum_{j=1}^{8} q_j 2^{j-1} \tag{1.27}$$

These integer values are then organized into a 256-bin histogram representing the feature vector useful for classification tasks.

1.5 LPQ with ternary coding (LPQ3)

As for LTP, the LPQ3 operator is formulated as follows:

$$q_j = \begin{cases} 1, f_j \geq \rho \cdot \tau \\ 0, -\rho \cdot \tau \leq f_j \leq \rho \cdot \tau \\ -1, f_j \leq -\rho \cdot \tau \end{cases} \tag{1.28}$$

where f_j is the j-th component of $\mathbf{F_x}$, ρ is the standard deviation of the all f_j and τ is a threshold. The quantized coefficients are then represented as integers in the interval 0 - 255 using the following binary codings:

$$b_+ = \sum_{j=1}^{8} (q_j == 1) 2^{j-1} \tag{1.29}$$

and

$$b_- = \sum_{j=1}^{8} (q_j == -1) 2^{j-1} \tag{1.30}$$

b_+ and b_- values are then summarized in two distinct 256 bins histograms and the two histograms are then concatenated thus providing a 512 valued feature vector, useful for classification task.

1.6 The Multi-threshold approach

The use of ternary and quinary codings requires respectively one threshold (τ) or a couple of thresholds (τ_1, τ_2). The Multi-Threshold approach consists in choosing a set of different τ for the ternary coding (or a set of different (τ_1, τ_2) for the quinary coding), in order to (i) extract one feature set for each threshold (or couple of thresholds), (ii) use each feature set to train a different classifier and (iii) fuse all these results according to a fusion rule (vote, sum, ...) [9, 22]. Exploiting this approach we defined two new texture descriptors: the Multi-Threshold LQP (MLQP) and Multi-Threshold LPQ3 (MLPQ3) [22]. In their original formulation we used:

- 25 couples of thresholds for MLQP, chosen as $\tau_1 = \{1, 3, 5, 7, 9\}$ and $\tau_2 = \{\tau_1 + 2, ..., 11\}$ (eg. if $\tau_1 = 1$ then $\tau_2 = \{3, 4, 5, 6, 7, 8, 9, 10, 11\}$ and if $\tau_1 = 9$ then $\tau_2 = 11$).
- 9 thresholds for MLPQ3, chosen as $\tau = \{0.2, 0.4, 0.6, 0.8, 1, 1.2, 1.4, 1.6, 1.8\}$.

In particular, we focused on the multi-threshold approach combined with support vector machines (SVM) as classifiers.

In its original form, a SVM is a binary classifier which learns the boundary between samples of two different populations by (i) transforming the input training feature vector into a multi-dimensional feature space and (ii) finding an optimal separating hyperplane in order to split the two populations. When a testing sample is classified by a SVM, the algorithm returns one label corresponding to the class (+1/-1) and one decision value (or score) corresponding to the distance of the sample to the hyperplane. Additional details are reported in Chapter 2.

As an example, the implementation of MLQP with SVMs is here reported (implementation of MLPQ3 follows the same scheme). Since binary SVMs are used, the “one against all” strategy is employed in order to classify a *multi-class* (m classes) dataset; the steps are:

- training m SVMs for each of the 25 feature sets from the training data;
- classifying each of the 25 feature sets (from the testing data) with its own group of m SVMs, getting m partial decision values (one decision value for each of the m classes);
- adding the 25 partial decision values corresponding to the *m-th* class, thus getting m different final decision values;
- assigning the class out of the m classes according to the greater final decision value.

Bibliography

[1] Haralick R, Dinstein, Shanmugam K. Textural features for image classification. IEEE Transactions on Systems Man and Cybernetics 1973;SMC-3:610–621.

[2] Ahonen T, Hadid A, Pietikäinen M. Face description with local binary patterns: application to face recognition. IEEE transactions on pattern analysis and machine intelligence December 2006;28(12):2037–41.

[3] Nanni L, Lumini A. Local binary patterns for a hybrid fingerprint matcher. Pattern Recognition 2008;41(11):3461–66.

[4] Ameling S, Wirth S, Paulus D, Lacey G, Vilarino F. Texture-Based Polyp Detection in Colonoscopy. In Meinzer, Hans-Peter And Deserno, Thomas Martin And Handels, Heinz And Tolxdorff T (ed.), Bildverarbeitung für die Medizin 2009. University of Koblenz-Landau Institute for Computational Visualistics Germany: Springer Berlin Heidelberg. ISBN 978-3-540-93860-6, 2009; 346–50.

[5] Tamura H, Mori S. Textural features corresponding to visual perception. Systems Man and 1978;75(6):460–473.

[6] Sklansky J. Image segmentation and feature extraction. IEEE Transactions on Systems Man and Cybernetics 1978;75(4):237–247.

[7] Hawkins JK. Textural Properties for Pattern Recognition. In Lipkin B, Rosenfeld A (eds.), Picture Processing and Psychopictorics Psychopictorics. New York: Academic Press, 1969; 347–370.

[8] Tuceryan M. Texture Analysis. In Chen CH, Pau LF, Wang PSP (eds.), The Handbook of Pattern Recognition and Computer Vision, 2nd edition. World Scientific Publiching Co., 1998; 207–248.

[9] Paci M, Nanni L, Severi S. An ensemble of classifiers based on different texture descriptors for texture classification. Journal of King Saud University Science ;doi: 10.1016/j.jksus.2012.12.001. ISSN 1018-3647.

[10] Fernández A, Álvarez MX, Bianconi F. Texture description through histograms of equivalent patterns. J Math Imaging Vis 2012;.

[11] Tan X, Triggs B. Enhanced local texture feature sets for face recognition under difficult lighting conditions. IEEE T IMAGE PROCESS June 2010; 19(6):1635–50.

[12] Nanni L, Lumini A, Brahnam S. Local binary patterns variants as texture descriptors for medical image analysis. ARTIF INTELL MED 2010; 49(2):117–25.

[13] Ojansivu V, Heikkilä J. Blur Insensitive Texture Classification Using Local Phase Quantization. In LECT NOTES COMPUT SC. Springer Berlin Heidelberg. ISBN 978-3-540-69904-0, 2008; 236–43.

[14] Ojala T, Pietikäinen M, Mäenpää T. Multiresolution Gray-Scale and Rotation Invariant Texture Classification with Local Binary Patterns. IEEE T PATTERN ANAL 2002;24(7):971–87.

[15] Vécsei A, Amann G, Hegenbart S, Liedlgruber M, Uhl A. Automated Marsh-like classification of celiac disease in children using local texture operators. COMPUT BIOL MED April 2011;41(6):313–25.

[16] Oliver A, Lladó X, Freixenet J, Martí J. False positive reduction in mammographic mass detection using local binary patterns. MICCAI International Conference on Medical Image Computing and Computer Assisted Intervention January 2007;10(Pt 1):286–93.

[17] Nanni L, Lumini A. A reliable method for cell phenotype image classification. Artificial intelligence in medicine June 2008;43(2):87–97.

[18] Woods B, Clymer B, Saltz J, Kurc T. A parallel implementation of 4-dimensional haralick texture analysis for disk-resident image datasets. In Supercomputing, 2004. Proceedings of the ACM/IEEE SC2004 Conference. nov. 2004; 48.

[19] Pietikäinen M, Ojala T, Xu Z. Rotation-invariant texture classification using feature distributions. Pattern Recognition 2000;33:43–52.

[20] Fang Y, Luo J, Cai Q, Dai W, Tan Y, Cheng G. A MANOVA of LBP Features for Face Recognition. InTech, July 2011. ISBN 978-953-307-368-2.

[21] Boland MV, Murphy RF. A neural network classifier capable of recognizing the patterns of all major subcellular structures in fluorescence microscope images of HeLa cells. Bioinformatics 2001;17(12):1213–23.

[22] Paci M, Nanni L, Lahti A, Aalto-Setälä K, Hyttinen J, Severi S. Non-Binary Coding for Texture Descriptors in Sub-Cellular and Stem Cell Image Classification. CURR BIOINFORM 2013;.

CHAPTER

TWO

NON-BINARY CODING FOR TEXTURE DESCRIPTORS IN SUB-CELLULAR AND STEM CELL IMAGE CLASSIFICATION

Michelangelo Paci[1], Loris Nanni[2], Anna Lahti[3], Katriina Aalto-Setälä[3,4], Jari Hyttinen[5], Stefano Severi[1]

[1] *DEIS, University of Bologna, Cesena, Italy*
[2] *DEI, University of Padua, Padua, Italy*
[3] *IBT, University of Tampere, Tampere, Finland*
[4] *Tampere University Hospital, Heart Center, Tampere, Finland*
[5] *BME, Tampere University of Technology, Tampere, Finland*

The content of this chapter was accepted for publication in *Current Bioinformatics*.

2.1 Goal of the study

The aim of this work is to assess the classification performance of new variants of the Local Binary Pattern (LBP) operator based on non-binary codings for biological image classification. Our goal is to provide a well-assessed feature set that can be used for cell and tissue analysis. In this work we test LBP, Local Ternary Pattern (LTP), Local Quinary Pattern (LQP) and Local Phase Quantization (LPQ) jointly with Support Vector Machine (SVM) and the random subspace of SVMs on six different datasets of cellular data. We show that the best approaches are Multi-Threshold LQP (MLQP) and the combination of MLQP and Multi-Threshold LPQ3 (MLPQ3).

2.2 Methods

2.2.1 Texture descriptors

The following texture descriptors were tested:

- LTP (see section 1.3) with different values for the threshold τ;
- LQP (see section 1.3) with different values for the thresholds τ_1 and τ_2;
- LPQ (see section 1.4) with different values for the thresholds τ_j;
- The method proposed by Vécsei *et al.* in [1]. It is based on LTP with an adaptive threshold estimated from the pixel standard deviation of each single image compared with the average standard deviation of the pixel intensities within the texture patches in the training set. Moreover, our variants (details in section 2.3.2) were also tested.

2.2.2 Classifiers

Two different classification approaches were tested: one stand-alone SVM and the random subspace of SVMs.

Support Vector Machine

The SVM algorithm was developed during the 1990's for industrial purposes [2, 3], and it was applied for different applications, such as face [4] and object [5] recognition. In its basic form, a SVM is a binary classifier which learns the boundary between samples of two different populations, projecting the samples into a multi-dimensional feature space and drawing a separating hyperplane. Advantages in using a SVM include (i) the capability of managing huge feature vectors, (ii) low risk of overfitting due to the maximized distance between the hyperplane and the closest samples, and (iii) the flexibility offered by various kernel functions (linear, radial, polynomial, etc.).

The random subspace

The random subspace method was introduced in [6] and consists in training N_c classifiers with randomly built subsets T_i from the original training set T. Considering l samples ($1 \leq l \leq L$) and c classes ($1 \leq j \leq c$), from the original d-dimensional training set
$T = \{(\mathbf{x}_l,\ t_l)|1 \leq l \leq L\},\ \mathbf{x}_l{\in}R^d,\ t_l{\in}C{=}\{1{,}...c\}$,
the $d \times k$-dimensional subsets
$T_i = \{(\mathbf{P}_i(\mathbf{x}_l),\ t_l)|1 \leq l \leq L,\ 1 \leq i \leq N_c\}$
are generated, where $\mathbf{P}_i(\mathbf{x}_l)$ represents the random selection of $k \times d$ features ($0 \leq k \leq 1$) from the d features of the sample l. The classification results of the N_c classifiers are then combined according to a fusion rule (e.g., vote rule, sum rule, etc.) [7]. In this study $N_c = 50$ and $k = 0.5$.

2.2.3 Datasets

Tests were performed on 6 datasets of sub-cellular parts (eg. organelles) or whole cells (eg. different cell lines).

2D HeLa

The 2D HeLa dataset[1] [8] (Fig. 2.1) contains 862 single cell images from fluorescence microscope acquisitions on HeLa cells. Images are 16 bit greyscale and 512 by 382 pixels in size. The whole dataset includes 10 different classes corresponding to 10 diverse stainings:

- Actin filaments (98 images);
- Endosomes (84 images);

---

[1] available for download at http://murphylab.web.cmu.edu//data/#2DHeLa

- Endoplasmic reticulum (86 images);
- Golgi giantin (87 images);
- Golgi GPP130 (85 images);
- Lysosome (91 images);
- Microtubules (91 images);
- Mitochondria (73 images);
- Nucleolus (80 images);
- Nucleus (87 images).

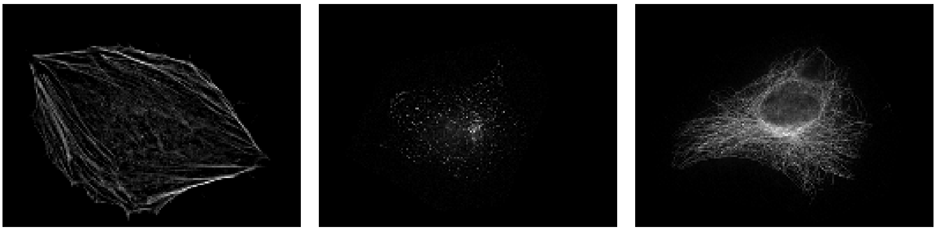

Figure 2.1: 2D HeLa dataset [8] illustrative samples (from left to right): Actin filaments, Endosomes, Microtubules.

LOCATE ENDOGENOUS mouse sub-cellular organelles (LE)

This dataset[2] [9, 10] (Fig. 2.2) contains images of endogenous proteins or features of specific organelles from mouse cells, stained with fluorescent antibodies or other probes. Images are 8 bit greyscale and 768 by 512 pixels in size. The 10 located organelles are:

- Actin;
- Endoplasmic Reticulum;
- Endosome;

---

[2] available for download at http://locate.imb.uq.edu.au/

- Golgi;
- Lysosome;
- Microtubules;
- Mitochondria;
- Nucleus;
- Peroxisome;
- Plasma Membrane.

For each organelle/class, about 50 images were acquired; as a result, the whole dataset includes 502 images, each containing up to 13 cells.

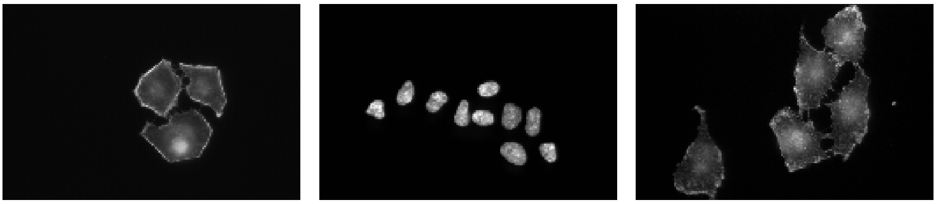

Figure 2.2: Locate endogenous dataset [9, 10] illustrative samples (from left to right): Actin, Nucleus, Plasma membrane.

LOCATE TRANSFECTED mouse sub-cellular organelles (LT)

This dataset[3] [9, 10] (Fig. 2.3) contains images of epitope- or fluorescence-tagged protein transiently expressed in the specific organelle and subsequently detected. Images are 8 bit greyscale and 768 by 512 pixels in size. In addition to the 10 classes contained in the LOCATE ENDOGENOUS dataset, the supplementary Cytoplasm class is included. For each organelle/class about 50 images were acquired. The whole dataset includes 553 images each containing up to 13 cells.

---

[3] available for download at http://locate.imb.uq.edu.au/

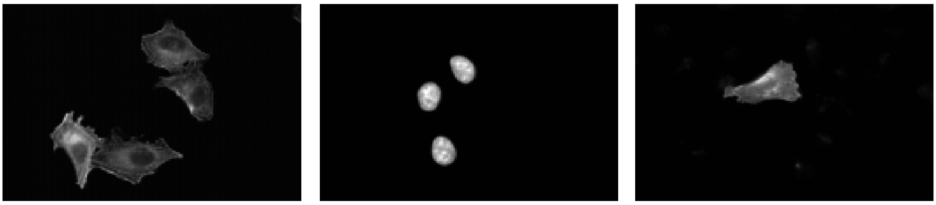

Figure 2.3: Locate transfected dataset [9, 10] illustrative samples (from left to right): Actin, Nucleus, Plasma membrane

STEM

This dataset (Fig. 2.4) was created from 100 movies of beating cardiomyocytes derived from hESCs and hiPSCs acquired in contrast phase microscopy (no staining and no dissociation or breaking up the cells) at the Institute of Biomedical Technology, Tampere, Finland. From each movie, 100 single cell frames were extracted, thus the whole dataset contains 10000 images. Images are 8 bit grayscale, and range in size (66 - 292) by (80 - 282) pixels. The dataset includes 2 classes:

- hESC (1700 images from 17 cells);
- hiPSC (8300 images from 83 cells).

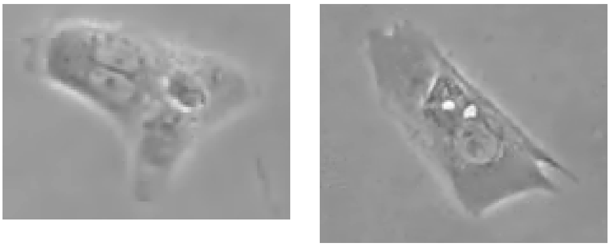

Figure 2.4: STEM dataset illustrative samples (from left to right): hESC, hiPSC.

CHO

This dataset[4] [11] (Fig. 2.5) contains 327 fluorescent microscopy images from Chinese Hamster Ovary cells. Images are 16 bit grayscale and 512 by 382 in size. Classes included in this dataset are:

- Giantin (77 images);
- Hoechst (69 images);
- Lamp2 (97 images);
- Nop4 (33 images);
- Tubulin (51 images).

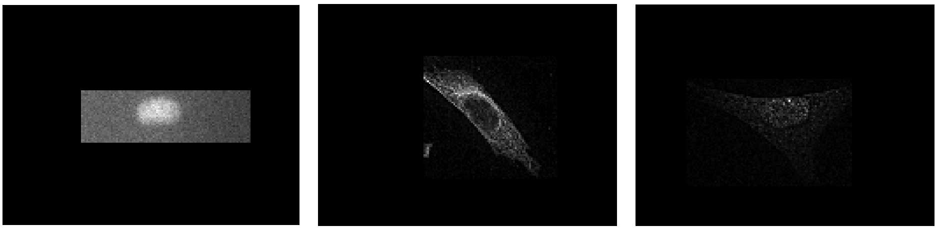

Figure 2.5: CHO dataset [11] illustrative samples (from left to right): Hoechst, Nop4, Tubulin.

RNAi

This dataset[5] (Fig. 2.6) contains 200 fluorescence microscopy images of fly cells subjected to a set of gene-knockdowns using RNAi. The cells are stained with DAPI to visualize their nuclei. Images are 16 bit grayscale and 1024 by 1024 in size. Ten genes were selected, and their Gene IDs are used for the class names. Each class contains 20 images.

---

[4] available for download at http://murphylab.web.cmu.edu//data/#2DCHO

[5] available for download from http://ome.grc.nia.nih.gov/iicbu2008/rnai/index.html

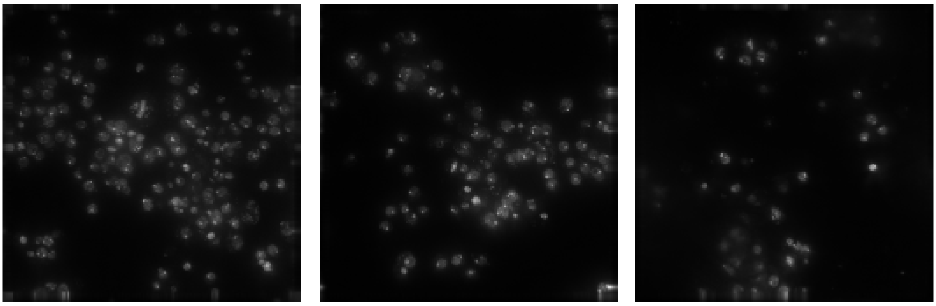

Figure 2.6: RNAi dataset illustrative samples (from left to right): CG03733, CG03938, CG12284.

2.2.4 Classification protocols

Two classification protocols were used:

- the 5-fold cross validation for the 2D HeLa, LE, LT, CHO and RNAi datasets;
- the Movie Leave One Out protocol for the STEM dataset. Due to the structure of the STEM dataset (as reported in 2.2.3) a canonical leave one out would have left pictures of the cell to be classified in the training set and biased the classification. The Movie Leave One Out protocol uses 99 calls (9900 images) as training set and 1 cell (100 images) as test set. This procedure is iterated for all the 100 cells.

The performance indicators are the accuracy for multi-class datasets and the area under the ROC curve (AUC) for the STEM dataset.

2.3 Experimental results

Before presenting the specific results, a brief overview of the performed tests is here proposed:

- standard texture descriptors (uniform LBP, uniform rotation invariant LBP and LPQ) are used the 6 datasets in order to provide a baseline for the next tests. Both the stand-alone SVM and the random subspace of SVMs were used;

- the non-binary coded variants of the previous descriptors and their multi-threshold versions were tested, as well as the method proposed in [1]. The vote rule was used as fusion rule both for the multi-threshold approach and for the random subspace;
- finally, we changed the fusion rule for the multi-threshold approach and the random subspace with the sum rule. Moreover we tested two different combinations of the best multi-threshold descriptors.

2.3.1 Classification using standard texture descriptors

Table 2.1 reports the performances of the following standard texture descriptors:

- U(x), uniform bins extracted using $LBP^{u2}(8,1)$ (x=8) and $LBP^{u2}(16,2)$ (x=16) (the length of the feature vector is 59 in case of U(8) and 243 in case of U(16));
- U(8+16), concatenation of U(8) and U(16) (the length of the feature vector is 59+243 = 302);
- RU(x), rotation invariant uniform bins extracted using $LBP^{riu2}(8,1)$ (x=8) and $LBP^{riu2}(16,2)$ (x=16) (the length of the feature vector is 10 in case of RU(8) and 18 in case of RU(16));
- RU(8+16), concatenation of RU(8) and RU(16) (the length of the feature vector is 10+18 = 28);
- L(x), standard LPQ with neighborhood radius x=3 or x=5 (the length of the feature vector is 256 in both cases);
- L(3+5), concatenation of L(3) and L(5) (the length of the feature vector is 512).

Each cell in Table 2.1 contains two values: the performance obtained by a stand-alone SVM and the performance obtained by a random subspace of SVMs (within brackets). Two performance indicators were used: the accuracy for the multi-class datasets and the area under the ROC curve for the STEM dataset. The AVG row in Table 2.1 reports the average performance for each texture descriptor: in spite of the weak mathematical meaning of this average, a unique global performance index is useful to compare the different descriptors.

Table 2.1: Comparison among standard texture descriptors. The performance indicators are AUC (%) for the STEM dataset and Accuracy (%) for the other datasets. Values for stand-alone SVM, in brackets for random subspace of SVMs.

	U(8)	U(16)	U(8+16)	RU(8)	RU(16)	RU(8+16)	L(3)	L(5)	L(3+5)
HeLa	82.4 (83.7)	86.7 (86.8)	87.1 (87.2)	84.2 (82.1)	88.0 (88.7)	89.3 (**90.0**)	81.7 (83.8)	83.6 (83.9)	88.3 (86.3)
LE	87.6 (88.6)	90.2 (89.6)	**91.6** (90.0)	80.4 (77.2)	87.6 (88.6)	89.6 (89.8)	82.0 (85.8)	82.4 (83.2)	85.6 (83.8)
LT	78.4 (81.8)	80.9 (82.4)	82.2 (82.6)	73.6 (70.4)	77.5 (79.3)	80.4 (81.6)	86.4 (86.7)	85.3 (87.3)	86.7 (**87.8**)
CHO	96.9 (96.6)	97.5 (96.6)	97.2 (96.9)	96.0 (95.6)	96.0 (96.6)	**98.1** (97.5)	95.6 (96.3)	91.0 (92.3)	97.8 (96.0)
RNAi	70.0 (73.0)	77.0 (76.5)	77.5 (**78.0**)	63.3 (66.5)	70.0 (69.5)	75.0 (76.0)	71.0 (67.5)	68.5 (69.0)	72.5 (74.0)
STEM	80.3 (78.1)	64.7 (69.7)	69.1 (69.3)	79.4 (76.4)	83.6 (81.7)	**87.9** (86.0)	79.8 (72.1)	74.7 (70.2)	76.6 (71.6)
AVG	82.6 (83.6)	82.8 (83.6)	84.1 (84.0)	79.4 (78.0)	83.8 (84.1)	86.7 (**86.8**)	82.8 (82.0)	80.9 (81.0)	84.6 (83.2)

2.3.2 Classification with new texture descriptors

In Table 2.2 we compare:

- LTPu, single LTP with uniform bins U(8+16), the threshold optimized for each dataset, only the best results are reported;
- MLTPu, all the single LTP with uniform mapping (LTPu) (τ={1,3,5,7,9}) are combined by vote rule;
- LQPu, single LQP with uniform bins U(8+16), only the best results are reported;
- MLQPu, MLQP with uniform bins U(8+16), 25 couples of thresholds (τ_1={1,3,5,7,9} and τ_2={τ_1+2, τ_1+3,. . . , 11}) and fusion by the vote rule;
- MLQPr, MLQP with rotation invariant uniform bins RU(8+16), 25 couples of thresholds (τ_1={1,3,5,7,9} and τ_2={τ_1+2, τ_1+3,. . . , 11}) and fusion by the vote rule;
- VE, the method proposed in [1], based on LTP and adaptive threshold;

- VLQ, VE applied to LQP, τ_1 estimated as in VE and $\tau_2 = 2 \times \tau_1$;
- MV1, multi-threshold variant of VE. For each class a different threshold is computed not using all the training images but only those images belonging to that class;
- LPQ3, only the best results are reported;
- MLPQ3, with 9 thresholds (τ_j={0.2, 0.4, 0.6, 0.8, 1, 1.2, 1.4, 1.6, 1.8}) and fusion by the vote rule.

In Table 2.2 the AVG row reports the average performance for each texture descriptor on all the datasets, while AVG2 doesn't consider the STEM dataset (it is useful for comparison with tests reported in 2.3.3). The best performance is obtained by MLQPr. Moreover, we note that in these tests the random subspace of SVMs exploiting the vote rule does not improve the performance of the stand-alone SVM.

2.3.3 Changing the fusion rule

Due to the low performance of random subspace of SVMs combined by the vote rule, additional tests using the sum rule to combine the SVMs into a new random subspace. The sum rule is used also as fusion rule for MLQPu or MLQPr and MLPQ3. Moreover, two additional combination of texture descriptors are tested, namely

- FUSu, fusion of MLQPu and MLPQ3 by the sum rule;
- FUSr, fusion of MLQPr and MLPQ3 by the sum rule.

The STEM dataset is not used in this test due to its large dimension which would have resulted in high computational load.
The results reported in Table 2.3 lead to the following considerations:

- also in these tests the random subspace does not improve significantly the classification performance;
- the multi-threshold approaches obtain better results with respect to the previous tests where the vote rule was used;
- MLQPr outperforms MLQPu;
- the best approach is FUSr.

Table 2.2: Comparison among the non-binary coded and multi-threshold texture descriptors. The performance indicators are AUC (%) for the STEM dataset and Accuracy (%) for the other datasets. Values for stand-alone SVM, in brackets for random subspace of SVMs.

	LTPu	MLTPu	LQPu	MLQPu	MLQPr
HeLa	85.3 (85.3)	89.1 (89.5)	90.1 (90.3)	87.9 (89.2)	91.1 (92.3)
LE	92.8 (91.4)	94.2 (94.6)	95.6 (95.6)	95.0 (94.8)	**98.6** (98.4)
LT	85.6 (84.3)	90.9 (90.6)	91.1 (90.6)	92.7 (92.9)	**98.1** (98.1)
CHO	98.4 (98.4)	97.9 (98.2)	98.1 (97.9)	98.8 (98.8)	99.1 (**99.3**)
RNAi	72.0 (72.5)	73.0 (71.5)	77.5 (78.5)	75.5 (77.0)	86.0 (**88.0**)
STEM	81.5 (82.7)	83.5 (84.0)	84.1 (84.5)	84.0 (84.8)	88.5 (**89.2**)
AVG	85.9 (85.8)	88.1 (88.1)	89.4 (89.6)	89.0 (89.6)	93.6 (**94.2**)
AVG2	86.8 (86.4)	89.0 (88.9)	90.5 (90.6)	90.0 (90.5)	94.6 (**95.2**)

	VE	VLQ	MV1	LPQ3	MLPQ3
HeLa	86.0 (86.1)	86.4 (87.2)	89.3 (90.3)	90.5 (90.6)	92.3 (**92.9**)
LE	94.0 (94.4)	93.8 (93.6)	95.2 (95.0)	97.8 (96.8)	**98.6** (98.4)
LT	87.3 (87.3)	90.6 (90.7)	91.3 (**91.8**)	93.1 (92.0)	95.3 (95.1)
CHO	97.2 (96.6)	97.5 (97.5)	97.5 (97.9)	96.3 (96.3)	96.9 (96.9)
RNAi	68.0 (63.0)	67.5 (68.0)	70.5 (71.0)	78.5 (79.0)	65.5 (70.5)
STEM	82.0 (82.6)	83.0 (82.9)	84.2 (84.5)	85.5 (85.2)	86.0 (86.0)
AVG	85.8 (85.0)	86.5 (86.7)	88.0 (88.4)	90.3 (90.0)	89.1 (90.0)
AVG2	86.5 (85.5)	87.2 (87.4)	88.8 (89.2)	90.9 (91.2)	89.7 (90.8)

Table 2.3: Comparison among the multi-threshold texture descriptors with sum rule. Accuracy (%) obtained using sum rule to combine the classifiers. Values for stand-alone SVM, in brackets for random subspace of SVMs.

	MLQPu	MLQPr	MLPQ3	FUSu	FUSr
HeLa	90.23 (90.23)	92.56 (93.02)	93.72 (93.60)	**94.53** (94.30)	93.95 (94.07)
LE	97.80 (97.80)	98.20 (98.20)	**98.80** (**98.80**)	**98.80** (**98.80**)	98.40 (**98.80**)
LT	96.36 (96.55)	98.00 (98.18)	98.36 (98.00)	97.82 (98.00)	**98.55** (98.36)
CHO	98.77 (99.08)	99.38 (99.38)	99.08 (99.08)	**100** (**100**)	**100** (99.69)
RNAi	85.62 (85.00)	90.63 (87.50)	74.38 (76.88)	86.25 (87.50)	91.87 (**91.88**)
AVG	93.75 (93.73)	95.75 (92.25)	92.87 (93.27)	95.48 (95.72)	96.55 (**96.56**)

2.3.4 Comparison with other descriptors and methods

In this section, we compare our results with other descriptors and classifiers representative of the state of art (Table 2.4), focusing in particular on those works using the same datasets investigated in this paper, thus providing a quantitative benchmark. In [12], the HeLa, CHO and RNAi datasets were used to assess the performances of a Multi Layer Perceptron (stand-alone and random subspace methods) trained with the Grey Level Co-occurence Matrix second-order statistics. A comparison between their best classification results obtained with the random subspace and our results using the random subspace of SVMs shows that our MLQPr feature set produces better results on HeLa (91.20% vs 93.02%) and CHO (98.86% vs 99.38%) datasets while it fails on the RNAi dataset (91.03% vs 87.50%). Conversely, FUSr shows the best results on all these datasets with the following classification rates: HeLa (94.07%), CHO (99.69%) and RNAi (91.88%). In [13] a set of four global and two local descriptors obtained the following accuracies on the HeLa, LE and LT datasets respectively: 95.8%, 99.5% and 97.0%. But these results were obtained via concatenation. The best results for one single descriptor were 90.8%, 95.7% and 91.8%.

Table 2.4: Comparison with other paper results. Accuracy (%) resulted using different classifiers (conc.: concatenated descriptors, single: single descriptors). [a] [12]; [b] [13].

	Our best descriptors		Zhang[a]	Nanni[b]	
	MLQPr	FUSr		conc.	single
HeLa	93.02	94.07	91.20	95.8	90.8
CHO	99.38	99.69	98.86	—	—
RNAi	87.50	91.88	91.03	—	—
LE	98.20	98.80	—	99.5	95.7
LT	98.18	98.36	—	97.0	91.8

2.4 Discussion and Conclusion

In this work we applied non-binary coded texture descriptors, such as LTP and LQP, for sub-cellular structure and stem cell image classification, in particular focusing on the threshold selection. Starting from the best texture descriptors in literature, we compare different approaches changing the coding (from binary to ternary and quinary) and the threshold selection (dataset optimized threshold or multiple thresholds). Changing the coding from binary to ternary improves the classification performances on four of the six proposed datasets (data refer to Tables 2.1 and 2.2, stand-alone SVM): LE (91.6% vs 92.8%), LT (82.2% vs 85.6%), CHO (97.2% vs 98.4%) and STEM (69.1% vs 81.5%). Changing the coding from binary to quinary improves again the results for all the datasets with the sole exception of RNAi: HeLa (87.1% vs 90.1%), LE (91.6% vs 95.6%), LT (82.2% vs 91.1%), CHO (97.2% vs 98.1%) and STEM (69.1% vs 84.1%). The use of the multi-threshold approach (fusion by the vote rule) results in better classification than the single-threshold descriptors as reported in Table 2.2: MV1 vs VE in each dataset, MLTPu vs LTPu in each dataset except CHO, MLPQ3 vs LPQ3 (the only exception is RNAi whose poor result biases the average accuracies AVG and AVG2 in Table 2.2).

Among all the tested descriptors, MLQPr achieves the highest performance: it gets the best results on LE, LT, CHO, STEM and RNAi datasets (see Table 2.2) both with the stand-alone SVM and the random subspace of SVMs. This suggests that the refined pattern partition, due to the quinary coding, combined with the lower correlation and amount of rotation invariant uniform patterns with respect to the uniform patterns, allows for better classification. The prevalence of MLQPr still remains using the sum rule instead of the vote rule, even if the influence of the random subspace of SVMs on the classification result is weak in this case. In addition, the highest accuracy reached by MLQPr in five out of the six proposed datasets leads us to consider our approach representative for the classification problem of cellular and sub-cellular images. Moreover, we studied the fusion between MLQP with MLPQ3 which shows an accuracy higher than MLQP alone (see Table 2.3) at the cost of a higher computational load: in fact the main drawback of FUSr is the computation time, which makes FUSr not suited for real time applications. For example, LQP extraction from one image of the 2D HeLa dataset takes approximately 3 seconds with a Duo P8600. In our opinion, FUSr could be used in real time applications if a TESLA GPU is used for feature extraction. Since the six tested datasets are representative of a quite large variety of biological classification problems, from sub-cellular to cellular identification, we can conclude that new non-binary coded variants of standard texture descriptors and their combinations provide improved results in biological image classification.

2.5 Acknowledgments

The authors thank: T. Ojala, M. Pietikäinen and T. Mäenpää for their LBP code and V. Ojansivu and J. Heikkilä for their LPQ code.

Bibliography

[1] Vécsei A, Amann G, Hegenbart S, Liedlgruber M, Uhl A. Automated Marsh-like classification of celiac disease in children using local texture operators. COMPUT BIOL MED April 2011;41(6):313–25.

[2] Boser BE, Guyon IM, Vapnik VN. A Training Algorithm for Optimal Margin Classifiers. In Proceedings of the 5th Annual ACM Workshop on Computational Learning Theory. ACM Press. ISBN 978-3-540-69904-0, 1992; 144–52.

[3] Vapnik V. The Support Vector method. In Artificial Neural Networks ICANN'97, volume 1327. Lecture Notes in Computer Science, 1997; 261–71.

[4] Osuna E, Freund R, Girosi F. Training Support Vector Machines: an Application to Face Detection. In Proceedings of the 1997 Conference on Computer Vision and Pattern Recognition (CVPR '97). Washington, DC, USA: IEEE Computer Society. ISBN 978-3-540-69904-0, 1997; 130–37.

[5] Blanz V, Scholkopf B, Bultho H, Burges C, Vapnik V, Vetter T. Comparison of view-based object recognition algorithms using realistic 3D models. In Artificial Neural Networks ICANN'96. Springer. ISBN 978-3-540-69904-0, 1996; 251–56.

[6] Ho TK. The random subspace method for constructing decision forests. IEEE transactions on pattern analysis and machine intelligence August 1998; 20(8):832–44.

[7] Wang X, Tang X. Random Sampling for Subspace Face Recognition. International Journal of Computer Vision October 2006;70(1):91–104.

[8] Boland MV, Murphy RF. A neural network classifier capable of recognizing the patterns of all major subcellular structures in fluorescence microscope images of HeLa cells. Bioinformatics 2001;17(12):1213–23.

[9] Fink JL, Aturaliya RN, Davis MJ, Zhang F, Hanson K, Teasdale MS, Kai C, Kawai J, Carninci P, Hayashizaki Y, Teasdale R. LOCATE: a mouse protein subcellular localization database. Nucleic Acids Research January 2006;34(Database issue):D213–7.

[10] Hamilton N, Pantelic R, Hanson K, Teasdale R. Fast automated cell phenotype image classification. BMC bioinformatics January 2007;8(1):110.

[11] Boland MV, Markey MK, Murphy RF. Automated recognition of patterns characteristic of subcellular structures in fluorescence microscopy images. Cytometry 1998;33(3):366–75.

[12] Zhang B, Pham TD. Phenotype Recognition with Combined Features and Random Subspace Classifier Ensemble. BMC bioinformatics April 2011; 12(1):128.

[13] Nanni L, Brahnam S, Lumini A. Novel Features for Automated Cell Phenotype Image Classification. Advances in Experimental Medicine and Biology 2011;680(3):207–13.

CHAPTER

THREE

A SET OF FEATURES FOR HEP-2 CELL CLASSIFICATION

Michelangelo Paci[1], Loris Nanni[2] and Stefano Severi[1]

[1] *DEIS, University of Bologna, Cesena, Italy*
[2] *DEI, University of Padua, Padua, Italy*

The content of this chapter was object of the *ICPR 2012 Contest on HEp-2 Cells Classification.*

Abstract

In this work we propose a set of texture descriptors for a high performance HEp-2 cells classification system. Our approach is based on two recently proposed texture descriptors (Multi-Threshold LQP (MLQP) and Multi-Threshold LPQ3 (MLPQ3)) and the Haralick features, all managed by using support vector machines SVMs. Our results show that our ensemble drastically outperform baseline methods local binary/ternary patterns: the average error rate is 2.4% using the 10-fold cross validation. The system here proposed has been submitted to the Contest on HEp-2 Cells Classification (http://mivia.unisa.it/hep2contest/index.shtml) hosted by the International Conference on Pattern Recognition (ICPR) 2012.

3.1 Introduction

ANA test is a commonly used test in screening of rheumatic diseases such as drug-induced lupus, Systemic Lupus erythemathosus and Scleroderma [1]. These antibodies can be used for a huge variety of substrates and staining techniques: a common application is IIF microscopy on human epithelial-2 (HEp-2) cells [2]. IIF slides are examinated by the physician at the fluorescence microscope and the diagnosis requires to assess both the fluorescence intensity and the staining pattern [3]. While the first step can be achieved by assigning a semi-quantitative score with respect to positive and negative controls contained in each slide, the second step, performed on the positive (and sometimes on the weakly positive) slides, can be difficult for a human observer. At the most used dilution [2, 4] the staining patterns are not easily detectable and classifiable thus texture analysis integrated into a computer-aided diagnosis system could be a valuable help for physicians. The most commonly described nuclear staining patterns are [5]:

- homogeneous: the interphase nuclei and the chromatin of mitotic cells show a homogeneous staining, specific for Systemic Lupus erythemathosus;
- speckled: a fine to coarse nuclear staining of the interphase cell nuclei;
- nucleolar: large coarse speckled staining inside the nucleus;
- cytoplasmic: fluorescent filaments crossing the cell length;

- centromere: discrete speckles spread everywhere in the interphase nuclei.

In this paper the staining pattern classification method proposed for the HEp-2 Cells Classification Contest (http://mivia.unisa.it/hep2contest/index.shtml) hosted by the ICPR 2012 is described.

3.2 Methods

3.2.1 Dataset

The whole HEp-2 cell dataset (MIVIA HEp-2 images dataset, http://mivia.unisa.it) [6] is constituted by 28 images (color, 24 bits, resolution of 1388 × 1038 pixels) acquired by means of a fluorescence microscope and containing 1457 cells. The training dataset provided to the HEp-2 cell classification contest participants and used in this study consists in 14 out of the 28 images for a total 721 cells (see http://mivia.unisa.it/hep2contest/dataset.shtml). In details the HEp-2 dataset is divided in the as follows (*pattern: whole dataset, training dataset;*):

- Centromere: 388, 208;
- Coarse Speckled: 239, 109;
- Cytoplasmatic: 128, 58;
- Fine Speckled: 225, 94;
- Homogeneous: 345, 150;
- Nucleolar: 257, 102;

Each image is 24 bits color and it is provided together with its segmentation mask. For the purpose of this study, each training picture was converted in 8 bits grayscale before applying the segmentation mask.

3.2.2 Texture descriptors

In this work we characterize each image with three descriptors: Multi-Threshold LQP (MLQP), Multi-Threshold LPQ3 (MLPQ3) and Haralick features (HAR):

- MLQP was calculated using 25 threshold couples ($\tau_1=\{1,3,5,7,9\}$ and $\tau_2=\{\tau_1+2, \tau_1+3, \ldots, 11\}$);

- MLPQ3 was calculated using 5 thresholds (τ_2={*0.2, 0.4, 0.6, 0.8, 1*});
- HAR was managed as a stand-alone descriptor: features were extracted exploring the GLCM matrix according to four directions (*0*°, *45*°, *135*° and *90*°), with *d=1*.

The multi-threshold approach was implemented as reported in Chapter 1.6 and finally the three scores resulted from MLQP, MLPQ3 and HAR were combined by the sum rule.

3.2.3 Classifiers and classification protocol

We used SVMs as classifiers and a 10-fold cross validation for testing the texture descriptors, in particular the 10-fold is performed 10 times and the average results are reported.

3.3 Experimental results

The first experiment was aimed at assessing the performances of some standard texture descriptors. Table 3.1 refers to the following nine standard texture descriptor:

- U(x), uniform bins extracted using $LBP^{u2}(8,1)$ (x=8) and $LBP^{u2}(16,2)$ (x=16) (the length of the feature vector is 59 in case of U(8) and 243 in case of U(16));
- U(8+16), concatenation of U(8) and U(16) (the length of the feature vector is 59+243 = 302);
- RU(x), rotation invariant uniform bins extracted using $LBP^{riu2}(8,1)$ (x=8) and $LBP^{riu2}(16,2)$ (x=16) (the length of the feature vector is 10 in case of RU(8) and 18 in case of RU(16));
- RU(8+16), concatenation of RU(8) and RU(16) (the length of the feature vector is 10+18 = 28);
- L(x), standard LPQ with neighborhood radius x=3 or x=5 (the length of the feature vector is 256 in both cases);

- L(3+5), concatenation of L(3) and L(5) (the length of the feature vector is 512).

The best performance was obtained by RU(8+16).

Table 3.1: Classification accuracy (%) of the nine standard texture descriptors.

U(8)	U(16)	U(8+16)	RU(8)	RU(16)	RU(8+16)	L(3)	L(5)	L(3+5)
88.39	92.89	93.75	85.28	90.78	**94.07**	91.40	86.57	93.13

The second test (Table 3.2) was aimed to assess the performances of two non-binary coded texture descriptors, namely LTP [7] and LPQ3, thus providing a basis for a comparison with results of the multi-threshold approach (Table 3.3). It is particularly interesting the result of LPQ varying the threshold τ: values greater than 1 degrade the classification performances, thus in the next tests MLPQ3 thresholds belong to interval *[0; 1]*. It is worth noting that LTP outperforms LBP and LPQ3 outperforms LPQ.

Table 3.2: Accuracy (%) of texture descriptors LTP and LPQ3.

τ	1	3	5	7	9	τ	0.2	0.6	1	1.4	1.8
LTP	**94.56**	93.17	89.76	85.85	86.19	LPQ3	94.69	**94.79**	86.50	81.60	79.90

Table 3.3 summarizes the results achieved by the three chosen descriptors. MLQP obtained an accuracy of 96.50%, while MLPQ3 got 95.22%.We emphasize that MLQP and MLPQ3 outperformed LTP and LPQ3 respectively.
The fusion by the sum rule between MLQP and MLPQ3 resulted in an accuracy of 97.00%. HAR got an accuracy of 95.51% while the global fusion MLQP + MLPQ3 + HAR obtained 97.57%.

Table 3.3: Accuracy (%) of the descriptors chosen for the HEp-2 Cells Classification Contest.

	MLQP	MLPQ3	HAR	MLQP+ MLPQ3	MLQP+ HAR	MLQP+MLPQ3+ HAR
Accuracy	96.50	95.22	95.51	97.00	96.50	**97.57**

3.4 Discussion and conclusions

The aim of this study was to provide a texture descriptor set useful for HEp-2 cell staining pattern classification. In [8] the classification rate on a population of 1222 patients was 90% for the positive only samples and 85% for the positive and weak samples. The performance degradation is clear when the university laboratory cohort of 924 patients is considered: the agreement comparing the visually and automatically defined patterns was 90.1% for the positive samples, but 74.3% only for the weak samples. In [9] the classification success rate on a population of 1041 patients was 83.1%.
Our approach, in its most complete formulation MLQP+ MLPQ3 + HAR shows a 97.57% accuracy on images of both positive and intermediate fluorescence, outperforming these previous studies. Especially we show that the multi-threshold approach combined with the quinary coding improves the performance of LBP (see Table 3.1) and LTP (see Table 3.2). Our algorithm was placed 13^{th} out of the 28 methods proposed for the ICPR 2012 Contest on HEp-2 Cells Classification.

Bibliography

[1] Lane SK, Gravel JW. Clinical utility of common serum rheumatologic tests. AM FAM PHYSICIAN March 2002;65(6):1073–1080.

[2] Solomon D, Kavanaugh A, Schur P. Evidence-based guidelines for the use of immunologic tests: Antinuclear antibody testing. ARTHRITIS RHEUM August 2002;47(4):434–444.

[3] NCCLS. I/LA02-A Quality Assurance for the Indirect Immunofluorescence Test for Autoantibodies to Nuclear Antigen (IF-ANA); Approved Guideline. NCCLS ILA2 A January 2012;16(11).

[4] Soda P, Iannello G. Aggregation of classifiers for staining pattern recognition in antinuclear autoantibodies analysis. IEEE T INF TECHNOL B May 2009; 13(3):322–329.

[5] Cordelli E, Soda P. Color to grayscale staining pattern representation in iif. In Proceedings of the 2011 24th International Symposium on Computer-Based Medical Systems, CBMS '11. Washington, DC, USA: IEEE Computer Society. ISBN 978-1-4577-1189-3, 2011; 1–6.

[6] Foggia P, Percannella G, Soda P, Vento M. Early experiences in mitotic cells recognition on hep-2 slides. In Computer-Based Medical Systems (CBMS), 2010 IEEE 23rd International Symposium on. oct. 2010; 38 –43.

[7] Tan X, Triggs B. Enhanced local texture feature sets for face recognition under difficult lighting conditions. IEEE T IMAGE PROCESS June 2010; 19(6):1635–50.

[8] Egerer K, Roggenbuck D, Hiemann R, Weyer M, Buettner T, Radau B, Krause R, Lehmann B, Feist E, Burmester G. Automated evaluation of autoantibodies on human epithelial-2 cells as an approach to standardize cell-based immunofluorescence tests. ARTHRITIS RES THER January 2010; 12(2):R40.

[9] Sack U, Knoechner S, Warschkau H, Pigla U, Emmrich F, Kamprad M. Computer-assisted classification of HEp-2 immunofluorescence patterns in autoimmune diagnostics. AUTOIMMUN REV September 2003;2(5):298–304.

Conclusion

GENERAL CONCLUSIONS

During the Ph.D. studies the author was involved in different and intriguing research topics, but in this thesis only the two main lines of research are exposed, shaping the thesis itself in the unusual form of a volume organized in two different parts. In this chapter we report conclusions that can be extracted from part I and part II.

In Part I we focused on human stem cell-derived CMs from the perspective of single cell computational modelling. In particular two types of CMs were investigated: hESC-CMs and hiPSC-CMs. Since 1998 when Thomson *et al.* [1] discovered how to extract pluripotent cells from human blastocysts, interest and high hopes arose as well as criticisms about the ethical issues and the applicability (eg. the hESC-CM safety itself and how to deliver the pluripotent cells in the damaged areas of the heart, as focused in [2]), which dampened the initial enthusiasm. In 2006/07 a new boost to research on human pluripotent stem cells arrived from the two seminal works of the groups of Shinya Yamanaka [3] and James Thomson [4] who were able, following two different protocols, to produce human pluripotent stem cells from adult somatic cells, sweeping the ethical doubts away and introducing new valuable elements such as the patient-specificity and the disease-specificity. On the contrary new questions arose:

- will differentiated hiPSC-CMs develop into a fully functional adult phenotype or will they just remain in an immature state?
- are hiPSC-CMs really safe for cellular therapies (the tumor issue reported in [5, 6])?

Diverse studies reported the feasibility of deriving CMs from hiPSCs, but on the contrary the ventricular-like and atrial-like hiPSC-CMs introduced in section 1.2.1 and described in chapter 3 still show relevant differences with respect to adult CMs, especially in terms of spontaneous beating and the slightly differently shaped APs (longer APD, more negative MDP). From the computational point of view, modelling hESC-CMs and hiPSC-CMs resulted an extremely challenging task since the beginning for the following reasons:

- with the exception of preliminary modelling works, such as [7], whose results were very helpful in developing our models, no specific hESC-CM or hiPSC-CM models were available in literature;
- the shortage of available experimental data from stem cell-derived CMs, especially hESC-CMs, and their high variability;
- open-questions about hESC-CM and hiPSC-CM electrophysiology, e.g. the functionality of the SR and of the Ca^{2+} handling system.

Our hESC-CM model is a first attempt to integrate the available data on hESC-CM currents and Ca^{2+} handling, replicating also the maturation process through the two developmental stages Early and Late [8]. We showed how the maturation process affects the automaticity of the beating, which resulted to be a more robust mechanism at the Early stage than at the Late one, as expected in the context of immature cells maturing towards the mature phenotype (eg. a small increment of the repolarizing K^+ currents I_{Kr}, I_{Ks} and I_{K1} blocks the spontaneous APs). The role of I_f as a pacemaker current has already been debated [9] but interestingly also I_{NaCa} showed to cover a decisive role in the automaticity. I_{NaCa} is an inward current during the late repolarization phase, opposing the repolarizing K^+ currents, on the contrary it is an outward current during the upstroke/depolarization, thus opposing the two main depolarizing currents, namely I_{Na} and I_{CaL}. Consequently it is no surprising that an I_{NaCa} increment blocks the spontaneous beating in the hESC-CM. In the Late model, the simulated blockade of I_{NaCa} by nickel or its simple zeroing stops the automaticity as well: in a scenario of a reduced (by maturation) I_f, I_{NaCa} has a key-role in mantaining the spontaneous beating. Moreover our model confirmed that a functional but still immature Ca^{2+} handling system is already present at the Early developmental stage, but the Ca^{2+} cycling is mainly governed by the sarcolemmal fluxes (eg. I_{CaL} and I_{NaCa}) as suggested by the only 12% reduction of the Ca^{2+} transient amplitude during the blockade of the Ca^{2+} release from the SR. At the Late stage a greater contribution of SR to Ca^{2+} cycling is confirmed by the 33% reduction of the Ca^{2+} transient amplitude. Interestingly, the experimental data we used for comparison [10, 11] were not initially taken into consideration during the model development, thus providing a further validation in terms of the Ca^{2+} transient shape (amplitude, Ca^{2+} transient Maximum Upstroke Velocity ($V_{\mathrm{maxCa,upstroke}}$) and Ca^{2+} transient Maximum Decay Velocity ($V_{\mathrm{maxCa,decay}}$)).

As we stated in chapter 2, this model suffers some limitations especially due to the lack of experimental data from CMs derived from HUMAN stem cells. Thus the compulsory choice was using also data from animal ESC-CMs: this led to two hybrid/"not fully human" models. Although this approach could appear inconsistent, it was already extensively used in the past for human CM models, such as the Courtemanche model [12] where guinea pig and rabbit data completed the experimental basis for the model development, or the Priebe model [13] where the ionic pumps and exchangers were derived from a previous guinea pig ventricular model [14].

In chapter 3 we presented our hiPSC-CM model, developed coincidentally during the same year Prof. Shinya Yamanaka and Prof. John B. Gurdon won the Nobel Prize for "the discovery that mature cells can be reprogrammed to become pluripotent" [15]. Unlike the hESC-CM model, during the development of the hiPSC-CM model we were facilitated by the solid set of experimental data published by Ma *et al.* [16], which allowed us also to discriminate between the atrial-like and the ventricular-like cells, and by the experience of the previous hESC-CM model. In addition of an improved ability in simulating current blockers effect, this model was used to provide a potential answer to the question "which are the main current differences between hiPSC-CMs and adult CMs and which of these are more relevant in order to reproduce an adult AP?". Understanding how far hiPSC-CMs are from adult CMs is fundamental, since they are already used in basic research as an *in-vitro* model for a better comprehension of their physiology and as disease-specific models for channel mutations, eg. for LQT syndromes [17, 18]. We focused on the ventricular-like hiPSC-CM since this is the most commonly observed phenotype during hiPSC differentiation into CMs (29 out of 40 hiPSC-CMs [18], 32 out of 59 hiPSC-CMs [16]) and thus we started a computational study mixing our model with the adult currents extracted from the recent O'Hara-Rudy model [19] of an adult ventricular cell (details in chapter 3). Our simulations suggested that the interplay of immature I_{Na}, I_{f} and I_{K1} is the main responsible for the spontaneous beating in hiPSC-CMs while the I_{CaL} activation shift towards negative potentials is the responsible of the observed prolonged APD. In this analysis we did not focus on the I_{NaCa} role, since specific data from hiPSC-CMs was not available, thus we used our previous data from hESC-CMs.

During these studies we retraced the first steps that from the first seminal CM models developed during the '60s and the '70s, eg. the generic mammalian ventricular AP model of Beeler and Reuter [20], led to high-detailed models describing the AP for specific species (Shannon/rabbit [21], Pandit/rat [22], Tentusscher/human [23]) also distinguishing on the basis of the cell/fiber location (eg. atrial, ventricular, endocardial or epicardial). Future models could also include gender-related differences, eg. the greater prolongation of the APD in response to K^+ current blockers in preparations from females, which result at the macroscopic level in diverse QTc intervals (women>men) or a different risk for developing bradycardia-related Torsades de Pointes (women>men) [24]. We started with the hybrid hESC-CM model, then we moved to the hiPSC-CM model based on a fully human dataset and describing two different phenotypes. Due to the growing interest in human stem cells, more specific forms of specialization and clustering of computational models will be possible along with new experimental measurements.

The secondary research topic of this Ph.D. thesis is the application of texture descriptors to biological image processing. In particular we took into consideration datasets of cellular and subcellular parts. Most of the used datasets (HeLa [25], CHO [26], etc.) are publicly available and commonly used as benchmarks to assess and compare the discriminant power of texture descriptors. The main conclusion of this study is that the combination of a non binary coding (ternary/quinary) and the multi-threshold approach, detailed in 1, improve the discriminant power among the various classes of the considered datasets. The first point was already studied in [27, 28] and confirmed by our results, but the threshold selection resulted controversial: the usual approach consists in optimizing the threshold for the specific problem/dataset, even if some attempts of an automatic threshold selection based on local and global statistics were proposed [27]. In our approach we overcome these difficulties by choosing a set of threshold (ternary coding) or a set of couples of thresholds (quinary coding) on the assumption that each feature set computed by a specific threshold/couple can catch some specific information not identifiable by the other feature sets from the processed image. Even if in thesis we mostly dealt with benchmark datasets, texture analysis and the use of texture descriptors are finding application also in the diagnostic field, even if they are far to become a standard clinical tool. Anyway the idea of a computed aided diagnostic system is promising, not in terms of replacement of the human physician, but to assist him in decisions and in the identification of features or peculiarities hard to be seen also by trained radiologists. In this sense not only standard descriptors are used for medical image processing (eg. [29] for breast tumor or [30] for brain lesions) but new descriptors are developed for more specific applications, such as in [27] for coeliac disease-related damages in duedonoscopy images or in [31] for chest CT images.

Bibliography

[1] Thomson JA. Embryonic Stem Cell Lines Derived from Human Blastocysts. Science 1998;282:1145–1147.

[2] Fujita J, Itabashi Y, Seki T, Tohyama S, Tamura Y, Sano M, Fukuda K. Myocardial Cell Sheet Therapy and Cardiac Function. American journal of physiology Heart and circulatory physiology September 2012;303(10):H1169–1182. ISSN 1522-1539.

[3] Takahashi K, Tanabe K, Ohnuki M, Narita M, Ichisaka T, Tomoda K, Yamanaka S. Induction of pluripotent stem cells from adult human fibroblasts by defined factors. Cell November 2007;131(5):861–872.

[4] Yu J, Vodyanik MA, Smuga-Otto K, Antosiewicz-Bourget J, Frane JL, Tian S, Nie J, Jonsdottir GA, Ruotti V, Stewart R, Slukvin II, Thomson JA. Induced Pluripotent Stem Cell Lines Derived from Human Somatic Cells. Science 2007;318(5858):1917–1920.

[5] Okita K, Ichisaka T, Yamanaka S. Generation of germline-competent induced pluripotent stem cells. Nature July 2007;448(7151):313–7. ISSN 1476-4687.

[6] Pasi CE, Dereli-Oz A, Negrini S, Friedli M, Fragola G, Lombardo A, Van Houwe G, Naldini L, Casola S, Testa G, Trono D, Pelicci PG, Halazonetis

TD. Genomic instability in induced stem cells. Cell Death Differ February 2011;.

[7] Itoh H, Naito Y, Tomita M. Simulation of developmental changes in action potentials with ventricular cell models. Syst Synth Biol March 2007;1(1):11–23.

[8] Sartiani L, Bettiol E, Stillitano F, Mugelli A, Cerbai E, Jaconi ME. Developmental changes in cardiomyocytes differentiated from human embryonic stem cells: a molecular and electrophysiological approach. Stem Cells 2007; 25(5):1136–1144.

[9] Accili EA, Proenza C, Baruscotti M, DiFrancesco D. From funny current to HCN channels: 20 years of excitation. News Physiol Sci February 2002; 17:32–37.

[10] Liu J, Fu JD, Siu CW, Li RA. Functional Sarcoplasmic Reticulum for Calcium Handling of Human Embryonic Stem Cell-Derived Cardiomyocytes: Insights for Driven Maturation. Stem Cells 2007;25(12):3038–3044.

[11] Satin J, Itzhaki I, Rapoport S, Schroder EA, Izu L, Arbel G, Beyar R, Balke CW, Schiller J, Gepstein L. Calcium handling in human embryonic stem cell-derived cardiomyocytes. Stem Cells 2008;26(8):1961–1972.

[12] Courtemanche M, Ramirez RJ, Nattel S. Ionic mechanisms underlying human atrial action potential properties: insights from a mathematical model. Am J Physiol July 1998;275(1 Pt 2):H301–321.

[13] Priebe L, Beuckelmann DJ. Simulation Study of Cellular Electric Properties in Heart Failure. Circulation Research June 1998;82(11):1206–1223. ISSN 0009-7330.

[14] Luo CH, Rudy Y. A dynamic model of the cardiac ventricular action potential. I. Simulations of ionic currents and concentration changes. Circ Res June 1994;74(6):1071–1096. ISSN 0009-7330.

[15] Nobelprize.org. The Nobel Prize in Physiology or Medicine 2012, 2012. URL http://www.nobelprize.org/nobel_prizes/medicine/laureates/2012/.

[16] Ma J, Guo L, Fiene S, Anson B, Thomson J, Kamp T, Kolaja K, Swanson B, January C. High purity human-induced pluripotent stem cell-derived cardiomyocytes: electrophysiological properties of action potentials and ionic currents. Am J Physiol Heart Circ Physiol November 2011;301(5):H2006–H2017.

[17] Matsa E, Rajamohan D, Dick E, Young L, Mellor I, Staniforth A, Denning C. Drug evaluation in cardiomyocytes derived from human induced pluripotent stem cells carrying a long QT syndrome type 2 mutation. Eur Heart J April 2011;32(8):952–962.

[18] Lahti AL, Kujala VJ, Chapman H, Koivisto AP, Pekkanen-Mattila M, Kerkela E, Hyttinen J, Kontula K, Swan H, Conklin BR, Yamanaka S, Silvennoinen O, Aalto-Setala K. Model for long QT syndrome type 2 using human iPS cells demonstrates arrhythmogenic characteristics in cell culture. Dis Model Mech November 2011;5(2):220–230. ISSN 1754-8403.

[19] O'hara T, Virág L, Varró A, Rudy Y. Simulation of the Undiseased Human Cardiac Ventricular Action Potential: Model Formulation and Experimental Validation. PLoS Comput Biol May 2011;7(5):e1002061. ISSN 1553-7358.

[20] Beeler BYGW, Reutert H. Reconstruction of the action potential of ventricular myocardial fibres. The Journal of physiology 1977;268:177–210.

[21] Shannon T, Wang F, Puglisi J, Weber C, Bers DM. A mathematical treatment of integrated Ca dynamics within the ventricular myocyte. Biophys J November 2004;87(5):3351–3371. ISSN 0006-3495.

[22] Pandit SV, Clark RB, Giles WR, Demir SS. A mathematical model of action potential heterogeneity in adult rat left ventricular myocytes. Biophysical journal December 2001;81(6):3029–51. ISSN 0006-3495.

[23] ten Tusscher KHWJ, Noble D, Noble PJ, Panfilov AV. A model for human ventricular tissue. Am J Physiol Heart Circ Physiol April 2004; 286(4):H1573–1589.

[24] Cheng J. Evidences of the gender-related differences in cardiac repolarization and the underlying mechanisms in different animal species and human. Fundamental clinical pharmacology February 2006;20(1):1–8. ISSN 0767-3981.

[25] Boland MV, Murphy RF. A neural network classifier capable of recognizing the patterns of all major subcellular structures in fluorescence microscope images of HeLa cells. Bioinformatics 2001;17(12):1213–23.

[26] Boland MV, Markey MK, Murphy RF. Automated recognition of patterns characteristic of subcellular structures in fluorescence microscopy images. Cytometry 1998;33(3):366–75.

[27] Vécsei A, Amann G, Hegenbart S, Liedlgruber M, Uhl A. Automated Marsh-like classification of celiac disease in children using local texture operators. COMPUT BIOL MED April 2011;41(6):313–25.

[28] Nanni L, Lumini A, Brahnam S. Local binary patterns variants as texture descriptors for medical image analysis. ARTIF INTELL MED 2010; 49(2):117–25.

[29] Holli K, Lääperi AL, Harrison L, Luukkaala T, Toivonen T, Ryymin P, Dastidar P, Soimakallio S, Eskola H. Characterization of Breast Cancer Types by Texture Analysis of Magnetic Resonance Images. Academic Radiology 2010; 17(2):135–141. ISSN 1076-6332.

[30] Holli KK, Harrison L, Dastidar P, Wäljas M, Liimatainen S, Luukkaala T, Ohman J, Soimakallio S, Eskola H. Texture analysis of MR images of patients with mild traumatic brain injury. BMC medical imaging January 2010;10:8. ISSN 1471-2342.

[31] Peng SH, Kim DH, Lee SL, Lim MK. Texture feature extraction based on a uniformity estimation method for local brightness and structure in chest CT images. Computers in biology and medicine 2010;40(11-12):931–42. ISSN 1879-0534.

LIST OF ORIGINAL PUBLICATIONS

Journal Articles

- **M. Paci**, J. Hyttinen, K. Aalto-Setälä and S.Severi, Computational models of ventricular- and atrial-like human induced pluripotent stem cell derived cardiomyocytes, *submitted.*

- **M. Paci**, L. Nanni and S.Severi, An ensemble of classifiers based on different texture descriptors for texture classification, Journal of King Saud University (Science), *in press.*

- **M. Paci**, L. Nanni, A. Lahti, K. Aalto-Setälä, J.Hyttinen and S. Severi, Non-Binary Coding for Texture Descriptors in Sub-Cellular and Stem Cell Image Classification, Current Bioinformatics, *in press.*

- **M. Paci**, L. Sartiani, M. Del Lungo, M. Jaconi, A. Mugelli, E. Cerbai and S. Severi, Mathematical modelling of the action potential of human embryonic stem cell derived cardiomyocytes, BioMedical Engineering OnLine 2012;11:61.

Conference proceedings

- **M. Paci**, J. Hyttinen and S. Severi, A Novel Model of the Action Potential of Ventricular-like Human Induced Pluripotent Stem Cell-derived Cardiomyocytes, Computing in Cardiology 2012, Krakow (Poland), September 2012, Comput Cardiol. 2012;39:289-292.

- **M. Paci**, J Hyttinen and S. Severi, Computational modelling of human induced pluripotent stem cell derived cardiomyocytes, Bioengineering Italian Group, Third Congress, Rome (Italy), June 2012, Proceedings: pp. 151-152.
- **M. Paci**, L. Nanni, A. Lahti, S. Severi, K. Aalto-Setälä and J.Hyttinen, Computer vision for human stem cell derived cardiomyocytes classification: the induced pluripotent VS embryonic stem cell case study, Computing in Cardiology 2011, Hangzhou (China), September 2011, Comput Cardiol. 2011;38:569-572.
- **M. Paci**, L. Sartiani, M.E. Jaconi, E. Cerbai and S. Severi, Mathematical modelling of electrotonic interaction between stem cell-derived cardiomyocytes and fibroblast", Computing in Cardiology 2010, Belfast (UK), September 2010, Comput Cardiol. 2010;37:649-652.
- S. Severi, **M. Paci**, L. Sartiani, M.E. Jaconi, A. Mugelli and E. Cerbai, Mathematical modelling of action potential in embryonic stem cell-derived cardiomyocytes, Bioengineering Italian Group, Second Congress, Turin (Italy), July 2010, Proceedings: pp. 151-152.

ACKNOWLEDGMENTS

First, I would like to thank my doctoral advisors, Prof. Stefano Severi and Prof. Gianni Gnudi. Without your precious guidance I would not have been able to accomplish nearly as much during my graduate studies: your support has been invaluable. Many thanks also to my reviewers Prof. Cristiana Corsi, Prof. Claudio Lamberti and Prof. Beatriz Trénor, to Prof. Loris Nanni, who introduced me to the texture analysis world, and to Prof. Laura Sartiani and Prof. Elisabetta Cerbai for their support and fruitful collaboration we had during these years.

I also thank all the members of the Ph.D. Committee, in particular our Coordinator Prof. Angelo Cappello, who constantly encouraged us during these years.

Kiitos to Prof. Jari Hyttinen who welcomed me in Finland and supported me through my work not only during the period I spent in Tampere but also later on, providing detailed and constructive comments to my work.

Thanks also to all the friends I met at the italian and finnish offices (in random order, if the OpenOffice randomizer works properly): Tomas Cervinka, Stefano Morotti, Maria Cristina Bisi, Florentino Santos, Iina Vainio, Pasi Kauppinen, Antti Ahola, Federico Riva, Elisa Passini, Ville-Pekka Seppä, Luca Tersi, Aurora Summa, Jarno Tanskanen, Emre Kapucu, Giulia Callisesi, Juho Väisänen, Nathaniel Narragirish, Javier Tabuenca, Filippo Cona, Federico Giovannini, Claudia Perazzini, Baran Aydogan, Soile Lönnqvist, Edite Figueiras, Alper Cömert, Soile Nymark, Antti Aula, Markus Hannula, Chiara Bartolucci and Atte Joutsen.

I'm especially grateful to my former colleagues at Elettrotecnica Zambelli, who always supported me, also when I decided to leave the company in order to start this Ph.D. adventure, in particular: Alessandro Marchini, Franco Fabbri, Giuseppe Maltese, Fabrizio Brunelli, Antonio Vicciantuoni and James Minns.

Last but not least my dearest friends Riccardo Amadori, Silvia Lombardi, Paolo Palmieri, Luca Calderoni, Elena Palmieri and Rosanna Villani.

Michelangelo Paci

Appendix

SUPPLEMENTARY METHODS: MATHEMATICAL MODELLING OF THE ACTION POTENTIAL OF HUMAN EMBRYONIC STEM CELL DERIVED CARDIOMYOCYTES

Human ESC culture and differentiation

The human embryonic stem cell (hESC) line H1 from WICELL RESEARCH INSTITUTE (Madison, WI) was cultivated following WICELL protocols. Briefly, undifferentiated hESCs were grown on irradiated mouse embryonic fibroblasts and passaged once a week using collagenase and mechanical dissociation. Propagation medium was composed of DMEM/F12 supplemented with 20% Serum Replacement, 1% penicillin-streptomycin, 1% non-essential amino-acids (NEAA), b-mercaptoethanol (SIGMA-ALDRICH CHEMIE, Buchs, Switzerland), L-Glutamine and 4 ng/ml human bFGF. Embryoid bodies (EBs) formation was obtained from hESC colonies incubated with collagenase and gently scraped in differentiation medium (KnockOut-DMEM supplemented with 20% Defined FBS (HYCLONE LABORATORIES South Logan, UT), 1% penicillin-streptomycin, 1% NEAA, L-Glutamine and b-mercapto-ethanol). EBs were cultured for 4 days in Costar ultra-low attachment 6-well plates (CORNING, Schiphol-Rijk, The Netherlands), with medium change every 2 days. EBs were then plated on gelatin-coated 6 cm-dishes and medium was changed every 2-3 days.

Cell isolation

Beating clumps were dissected from embryo bodies using a microscalpel and directly placed into the solution used to perform intracellular recordings. Alternatively, they were digested with 1 mg/ml collagenase B (ROCHE, Basel, Switzerland) in PBS supplemented with 30 mM calcium for 15-20 minute at 37°C with pipetting every 5-10 min. Dissociated cells were then plated on gelatin-coated dishes in differentiation medium and used for patch-clamp recordings.

Patch-clamp recordings

The experimental set-up for patch-clamp (whole-cell) recording and data acquisition was similar to that described previously [1]. Briefly, the patch-clamped cell was superfused by means of a temperature-controlled (37°C) micro-superfusor allowing rapid changes of the solution bathing the cell. Patch-clamp pipettes, prepared from glass capillary tubes (HARVARD APPARATUS, Edenbridge, UK) by means of a two-stage horizontal puller (SUTTER INSTITUTE, Sacramento, CA, model P-87), had a resistance of 2-3 MW when filled with the internal solution. Cell membrane capacitance (C_m) was measured by integrating the capacitance current recorded during a ±10 mV hyperpolarizing pulse from a holding potential of -70 mV, as previously reported [1]. Series resistance and membrane capacitance were compensated in order to minimize the capacitive transient. Transient outward potassium current (I_{to}) was evoked by steps from -40 to +70 mV (holding potential -70 mV), after a pre-step to -40 mV to inactivate sodium current (I_{Na}). I_{to} was measured as the difference between peak outward current at the beginning of the depolarizing step and the steady state current at the end of the step, and normalized with respect to C_m. The funny current (I_f) was evoked by hyperpolarizing steps from -50 to -130 mV (holding potential -40 mV). Steady-state values of current were calculated by fitting current traces to a mono-exponential function. I_f amplitudes were measured as the difference between the extrapolated value at the steady state and that at the beginning of the test pulse, and normalized with respect to C_m, as reported elsewhere [2]. Sodium-calcium exchanger (I_{NaCa}) current was elicited with an ascending voltage ramp (from -120 to +70 mV, holding potential -40mV). Current was defined as the difference current in the absence and presence of $NiCl_2$ (2 mM) and amplitude was normalized to whole cell capacitance.

Intracellular recordings

The experimental set-up for intracellular recordings and data acquisition was similar to that described previously [2]. Briefly, spontaneously beating EBs were fixed on bottom of a perfusion chamber, thermostatically controlled at $33-35°C$ and superfused a constant-flow. Embryoid body electrical activity was recorded using a standard electrophysiological techniques, as previously reported [3]. Briefly, the recording electrode consisted of a short Ag/AgCl pin that was partly inserted into a floating glass microelectrode containing 3 M KCl and connected to the headstage of the amplifier. An Ag/AgCl pellet served as reference electrode in the perfusion chamber. The tip resistance of the microelectrode ranged between 30 and 40 MW. The recording microelectrode and the reference electrode were connected through a high input impedance amplifier (BIOMEDICA MANGONI, Pisa, Italy) interfaced with a computer. The microelectrode was slowly moved into the chamber under microscopic inspection with the use of a micromanipulator. The electrode potential was compensated to zero in the bathing solution. Spontaneous APs were digitized by an A/D converter and analyzed off-line with Iox software (EMKA TECHNOLOGY, Falls Church, VA).

Solutions

Normal Tyrode's solution (in mM): $NaCl$ 140; KCl 5.4; $CaCl_2$ 1.8; $MgCl_2$ 1.2; $D-glucose$ 10; $HEPES$ 5 (pH 7.35 with $NaOH$).
Modified Tyrode's solution for I_f current (in mM): $NaCl$ 140, KCl 25, $CaCl_2$ 1.5, $MgCl_2$ 1.2, $BaCl_2$ 2, $MnCl_2$ 2, $4-aminopyridine$ 0.5, $glucose$ 10, $HEPES-NaOH$ 5 (pH 7.35); this solution allowed the reduction of interference from other currents, i.e. I_{CaL} , I_{CaT}, I_{K1} and I_{to}. Modified Tyrode's solution for I_{to} current: normal Tyrode's solution plus $CdCl_2$ 0.5 mM.
Pipette solutions for AP, I_{to}, I_f (in mM): $K-Aspartate$ 130; Na_2-ATP 5, $MgCl_2$ 2, $CaCl_2$ 5, $EGTA$ 11, $HEPES-KOH$ 10 (pH 7.2). Pipette solutions for I_{CaL} (in mM): $Mg-ATP$ 5, $EGTA$ 15, $TEA-Cl$ 20, $HEPES$ 10, $CsCl$ 125, (pH 7.20 with $CsOH$).
Solution for I_{NaCa} current (in mM): $NaCl$ 128; $CsCl$ 10; $CaCl_2$ 2; $MgCl_2$ 1; $Na-HEPES$ 10; $Glucose$ 10; $Lacidipine$ 10; $SITS$ 100 ; $Ouabaine$ 0.5. (PH 7.4 with $CsOH$); this solution allowed the reduction of interference from other currents, i.e. I_{CaL}, I_{Cl}, I_{NaK}.

Pipette solutions for I_{NaCa} (in mM): $CsCl$ 120; $CaCl_2$ 3; $MgCl_2$ 0.5; $HEPES$ 20; $Mg - ATP$ 5; $BAPTA(K^+)$ 4 5; (PH 7.25 with $CsOH$)
External solution for intracellular recordings (in mM): $NaCl$ 125, KCl 4, $NaHCO_3$ 25, NaH_2PO_4 0.5, $MgSO_4$ 1.2, $CaCl_2$ 2.7, $Glucose$ 1 (pH 7.2 when gassed with 5% $CO_2/95\%O_2$.
Pipette solution for intracellular recordings (in mM): KCl 3

Formulation of the hESC-CM model

Model Parameters

RaI_{xx} represents a variable fraction (ratio), of the current maximal conductance in the adult model ([4], except where differently specified). Time constants in *ms.*

$$Na_o = 150.5\ (mM)$$

$$K_o = 4\ (mM)$$

$$Ca_o = 2.7\ (mM)$$

$$Na_i = 7\ (mM)$$

$$K_i = 140\ (mM)$$

$$Ca_i = 0.0002\ (mM)$$

$$Ca_{SR} = 0.2\ (mM)$$

$$g_{CaL} = 0.175 \times Ra_{ICaL}\ (dm^3/(F \times s))$$

$$Ra_{ICaL} = \begin{cases} 0.25 & , Early \\ 0.422 & , Late \end{cases} \quad (dimensionless)$$

$$g_{bca} = 0.592\ \times Ra_{Iback}(S/F)$$

$$Ra_{Iback} = \begin{cases} 0.2 & , Early \\ 1 & , Late \end{cases} \quad (dimensionless)$$

$$Buf_c = 0.25\ (mM)$$

$$Buf_{sr} = 10\ (mM)$$

$$K_{buf_c} = 0.001\ (mM)$$

$$K_{buf_{sr}} = 0.3\ (mM)$$

$$K_{up} = 0.00025\ (mM)$$

$$V_{leak} = 0.08\ \times Ra_{Ileak}\ (1/s)$$

$$Ra_{Ileak} = \begin{cases} 0.005556 & ,Early \\ 0.3 & ,Late \end{cases} \quad (dimensionless)$$

$$Cm = 185\ \times Ra_{Cm}\,(pF) = \begin{cases} 41\ pF, Early\ (30\ cells) \\ 33\ pF,\ Late\ (26\ cells) \end{cases}$$

$$Ra_{Cm} = \begin{cases} 0.22162 & ,Early \\ 0.17838 & ,Late \end{cases} \quad (dimensionless)$$

$$V_c = 16404 \times Ra_{Cm}\ (um^3)$$

$$V_{sr} = 1094\ \times Ra_{Cm}\ (um^3)$$

$$Vmax_{up} = 0.425 \times Ra_{Iup}\ (mM/s)$$

$$Ra_{Iup} = \begin{cases} 0.133 & ,Early \\ 0.33 & ,Late \end{cases} \quad (dimensionless)$$

$$a_{rel} = 16.464\ (mM/s)$$

$$b_{rel} = 0.25\ (mM)$$

$$c_{rel} = 8.232\ (mM/s)$$

$$Ra_{Irel} = \begin{cases} 0.0111 & ,Early \\ 0.4 & ,Late \end{cases} \quad (dimensionless)$$

$$\tau_g = 2\ (ms)$$

$$K_{pCa} = 0.0005\ (mM)$$

$$g_{pCa} = 0.825\ \times Ra_{IpCa}(A/F)$$

$$Ra_{IpCa} = 1\ (dimensionless)$$

$$g_{Na} = 14838\ \times Ra_{INa}(S/F)$$

$$Ra_{INa} = \begin{cases} 0.038 & ,Early \\ 1 & ,Late \end{cases} \quad (dimensionless)$$

$$g_{K1} = 5405{\times}Ra_{IK1}\ (S/F)$$

$$Ra_{IK1} = \begin{cases} 0.0445 & ,Early \\ 0.2136 & ,Late \end{cases} \quad (dimensionless)$$

$$F = 96485.3415\ (C \times mM)$$

$$R = 8.314472\ (J/(M \times K))$$

$$T = 310\ (K)$$

$$g_{Kr} = 96\ {\times}Ra_{IKr}(S/F)$$

$$Ra_{IKr} = \begin{cases} 3 & ,Early \\ 1.4 & ,Late \end{cases} \quad (dimensionless)$$

$$L_0 = 0.025\ (dimensionless)$$

$$P_{kna} = 0.03\ (dimensionless)$$

$$g_{Ks} = 157{\times}Ra_{IKs}\ (S/F)$$

$$Ra_{IKs} = 0.1\ (dimensionless)$$

$$K_{NaCa} = 1000\ {\times}Ra_{INaCa}(A/F)$$

$$Ra_{INaCa} = \begin{cases} 17.50 & ,Early \\ 18.24 & ,Late \end{cases} \quad (dimensionless)$$

$$K_{sat} = 0.1\ (dimensionless)$$

$$Km_{Ca} = 1.38\ (mM)$$

$$Km\ _{ai} = 87.5\ (mM)$$

$$\alpha = \begin{cases} 0.8 & ,Early \\ 0.38 & ,Late \end{cases} \quad (dimensionless)$$

$$\gamma = 0.35\ (dimensionless)$$

$$K_{mNa} = 40\ (mM)$$

$$K_{mk} = 1\ (mM)$$

$$P_{NaK} = 1.362\ \times Ra_{INaK}(A/F)$$

$$Ra_{INaK} = \begin{cases} 0.7 & ,Early \\ 0.83 & ,Late \end{cases} \quad (dimensionless)$$

$$g_{to} = 294 \times Ra_{Ito}\ (S/F)$$

$$Ra_{Ito} = \begin{cases} 0.065622 & ,Early \\ 0.165653 & ,Late \end{cases} \quad (dimensionless)$$

$$g_f = 90.926 \times Ra_{If}\ (S/F)$$

$$Ra_{If} = \begin{cases} 0.5389 & ,Early \\ 0.23 & ,Late \end{cases} \quad (dimensionless)$$

$$\tau_f = 1900\ (ms)$$

Membrane Potential

$$\frac{\mathrm{d}V}{\mathrm{d}time} = -I_{ion} = \\ = -\left(I_{K1} + I_{to} + I_{Kr} + I_{Ks} + I_{CaL} + I_{NaK} + I_{Na} + I_{NaCa} + I_{b_{Ca}} + I_{p_{Ca}} + I_{CaT} + I_f\right) \tag{S1}$$

Na^+ current, I_{Na}

$$I_{Na} = g_{Na} \cdot m^3 \cdot h \cdot j \cdot (V - E_{Na}) \tag{S2}$$

I_{Na}, h gate

$$h_{inf} = \begin{cases} \frac{1}{\sqrt{\left(1+e^{\frac{V+73}{5.6}}\right)}} & ,Early \\ \frac{1}{\left(1+e^{\frac{V+71.55}{7.43}}\right)^2} & ,Late \end{cases} \tag{S3}$$

$$\alpha_h = \begin{cases} 0.057 \cdot e^{\frac{-(V+80)}{6.8}}, \text{ if } V < -40 \\ 0, \text{ otherwise} \end{cases} \tag{S4}$$

$$\beta_h = \begin{cases} 2.7 \cdot e^{0.079 \cdot V} + 3.1 \times 10^5 \cdot e^{0.3485 \cdot V}, \text{ if } V < -40 \\ \frac{0.77}{0.13 \cdot \left(1+e^{\frac{V+10.66}{-11.1}}\right)}, \text{ otherwise} \end{cases} \tag{S5}$$

$$\tau_h = \frac{2.8}{\alpha_h + \beta_h} \tag{S6}$$

$$\frac{\mathrm{d}h}{\mathrm{d}time} = \frac{h_{inf} - h}{\tau_h} \tag{S7}$$

I_{Na}, $\boldsymbol{j}$ gate

$$j_{inf} = \begin{cases} \frac{1}{\sqrt{\left(1+e^{\frac{V+73}{5.6}}\right)}} & ,Early \\ \frac{1}{\left(1+e^{\frac{V+71.55}{7.43}}\right)^2} & ,Late \end{cases} \tag{S8}$$

$$\alpha_j = \begin{cases} \frac{\left(-25428 \cdot e^{0.2444 \cdot V} - 6.948 \times 10^{-6} \cdot e^{-0.04391 \cdot V}\right) \cdot (V+37.78)}{1+e^{0.311 \cdot (V+79.23)}}, \text{ if } V < -40 \\ 0, \text{ otherwise} \end{cases} \tag{S9}$$

$$\beta_j = \begin{cases} \frac{0.02424 \cdot e^{-0.01052 \cdot V}}{1+e^{-0.1378 \cdot (V+40.14)}}, \text{ if } V < -40 \\ \frac{0.6 \cdot e^{0.057 \cdot V}}{1+e^{-0.1 \cdot (V+32)}}, \text{ otherwise} \end{cases} \tag{S10}$$

$$\tau_j = \frac{1}{\alpha_j + \beta_j} \tag{S11}$$

$$\frac{\mathrm{d}j}{\mathrm{d}time} = \frac{j_{inf} - j}{\tau_j} \tag{S12}$$

I_{Na}, $\boldsymbol{m}$ gate

$$m_{inf} = \frac{1}{\left(1+e^{\frac{-56.86-V}{9.03}}\right)^2} \tag{S13}$$

$$\alpha_m = \frac{1}{1+e^{\frac{-60-V}{5}}} \tag{S14}$$

$$\beta_m = \frac{0.1}{1+e^{\frac{V+35}{5}}} + \frac{0.1}{1+e^{\frac{V-50}{200}}} \tag{S15}$$

$$\tau_m = \alpha_m \cdot \beta_m \tag{S16}$$

$$\frac{\mathrm{d}m}{\mathrm{d}time} = \frac{m_{inf} - m}{\tau_m} \tag{S17}$$

L-type Ca^{2+} current, I_{CaL}

$$I_{CaL} = \frac{g_{CaL} \cdot d \cdot f \cdot fCa \cdot 4 \cdot V \cdot F^2}{R \cdot T} \cdot \frac{\left(Ca_i \cdot e^{\frac{2 \cdot V \cdot F}{R \cdot T}} - 0.341 \cdot Ca_o\right)}{e^{\frac{2 \cdot V \cdot F}{R \cdot T}} - 1} \tag{S18}$$

I_{CaL}, $\boldsymbol{d}$ gate

$$d_{inf} = \begin{cases} \frac{1}{1+e^{\frac{12.5-V}{12.5}}} & ,Early \\ \frac{1}{1+e^{\frac{16-V}{12.8}}} & ,Late \end{cases} \tag{S19}$$

$$\alpha_d = \frac{1.4}{1+e^{\frac{-35-V}{13}}} + 0.25 \tag{S20}$$

$$\beta_d = \frac{1.4}{1+e^{\frac{V+5}{5}}} \tag{S21}$$

$$\gamma_d = \frac{1}{1+e^{\frac{50-V}{20}}} \tag{S22}$$

$$\tau_d = \alpha_d \cdot \beta_d + \gamma_d \tag{S23}$$

$$\frac{\mathrm{d}d}{\mathrm{d}time} = \frac{d_{inf}-d}{\tau_d} \tag{S24}$$

I_{CaL}, f_{Ca} gate [5]

$$\alpha_{fCa} = \begin{cases} \frac{1}{1+\left(\frac{Ca_i+0.00011}{0.000325}\right)^8} & ,Early \\ \frac{1}{1+\left(\frac{Ca_i}{0.0006}\right)^8} & ,Late \end{cases} \tag{S25}$$

$$\beta_{fCa} = \begin{cases} \frac{0.1}{1+e^{\frac{Ca_i+0.00011-0.0005}{0.0001}}} & ,Early \\ \frac{0.1}{1+e^{\frac{Ca_i-0.0009}{0.0001}}} & ,Late \end{cases} \tag{S26}$$

$${}_{fCa} = \begin{cases} \frac{0.2}{1+e^{\frac{Ca_i+0.00011-0.00075}{0.0008}}} & ,Early \\ \frac{0.3}{1+e^{\frac{Ca_i-0.00075}{0.0008}}} & ,Late \end{cases} \tag{S27}$$

$$fCa\ _{nf} = \begin{cases} \frac{\alpha_{fCa}+\beta_{fCa}+{}_{fCa}+0.23}{1.46} & ,Early \\ \frac{\alpha_{fCa}+\beta_{fCa}+{}_{fCa}}{1.3156} & ,Late \end{cases} \tag{S28}$$

$$\tau_{fCa} = 2 \tag{S29}$$

$$\frac{\mathrm{d}fCa}{\mathrm{d}time} = constfCa \cdot \frac{fCa_{inf}-fCa}{\tau_{fCa}} \tag{S30}$$

$$constfCa = \begin{cases} 0, \text{ if } \left(fCa_{inf} > fCa\right) \text{ and } (V > -60) \\ \qquad 1, \text{ otherwise} \end{cases} \tag{S31}$$

I_{CaL}, $\boldsymbol{f}$ gate [5]

$$f_{inf} = \frac{1}{1+e^{\frac{V+20}{7}}} \tag{S32}$$

$$\tau_f = \begin{cases} 100 & ,Early \\ \left(1125 \cdot e^{\frac{-(V+27)^2}{240}} + 80 + \frac{165}{1+e^{\frac{25-V}{10}}}\right) \cdot & \end{cases}$$

$$\cdot \begin{cases} \left(1 + 1433 \cdot (Ca_i - 50 \times 10^{-6})\right), \frac{\mathrm{d}f}{\mathrm{d}time} > 0 \\ 1 \quad ,otherwise \end{cases} ,Late \tag{S33}$$

$$\frac{\mathrm{d}f}{\mathrm{d}time} = \frac{f_{inf} - f}{\tau_f} \tag{S34}$$

$T - typeCa^{2+}$ Current, I_{CaT} [6]

$$I_{CaT} = g_{CaT} \cdot dCaT \cdot fCaT \cdot (V - E_{Ca}) \tag{S35}$$

I_{CaT}, $\boldsymbol{dCaT}$ gate

$$dCaT_{inf} = \frac{1}{1+e^{-\frac{V+26.3}{6}}} \tag{S36}$$

$$\tau_{dCaT} = \frac{1}{1.068 \cdot e^{\frac{V+26.3}{30}} + 1.068 \cdot e^{-\frac{V+26.3}{30}}} \tag{S37}$$

$$\frac{ddCaT}{dtime} = \frac{dCaT_{inf} - dCaT}{\tau_{dCaT}} \tag{S38}$$

I_{CaT}, $\boldsymbol{fCaT}$ gate

$$fCaT_{inf} = \frac{1}{1+e^{\frac{V+61.7}{5.6}}} \tag{S39}$$

$$\tau_{fCaT} = \frac{1}{0.0153 \cdot e^{-\frac{V+61.7}{83.3}} + 0.015 \cdot e^{\frac{V+61.7}{15.38}}} \tag{S40}$$

$$\frac{dfCaT}{dtime} = \frac{fCaT_{inf} - fCaT}{\tau_{fCaT}} \tag{S41}$$

Transient outward current, I_{to}

$$I_{to} = g_{to} \cdot r \cdot s \cdot (V - E_K) \tag{S42}$$

I_{to}, $\boldsymbol{r}$ gate

$$r_{inf} = \frac{1}{1 + e^{\frac{-5-V}{1.8}}} \tag{S43}$$

$$\tau_r = 9.5 \cdot e^{\frac{-(V+40)^2}{1800}} + 0.8 \tag{S44}$$

$$\frac{\mathrm{d}r}{\mathrm{d}time} = \frac{r_{inf} - r}{\tau_r} \tag{S45}$$

I_{to}, *s* gate

$$s_{inf} = \frac{1}{1+e^{\frac{V+20}{5}}} \tag{S46}$$

$$\tau_s = 85 \cdot e^{\frac{-(V+45)^2}{320}} + \frac{5}{1+e^{\frac{V-20}{5}}} + 3 \tag{S47}$$

$$\frac{\mathrm{d}s}{\mathrm{d}time} = \frac{s_{inf} - s}{\tau_s} \tag{S48}$$

Rapid delayed rectifier K^+ current, I_{Kr}

$$I_{Kr} = g_{Kr} \cdot \sqrt{\frac{K_o}{5.4}} \cdot Xr1 \cdot Xr2 \cdot (V - E_K) \tag{S49}$$

I_{Kr}, *Xr1* gate [5]

$$V_{1/2} = 1000 \cdot \left(-\frac{R \cdot T}{F \cdot Q} \cdot ln\left(\frac{\left(1+\frac{Ca_o}{2.6}\right)^4}{L_0 \cdot \left(1+\frac{Ca_o}{0.58}\right)^4}\right) - 0.026\right) \tag{S50}$$

$$xr1_{inf} = \frac{1}{1+e^{\frac{V_{1/2}-V}{7}}} \tag{S51}$$

$$\alpha_{xr1} = \frac{450}{1+e^{\frac{-45-V}{10}}} \tag{S52}$$

$$\beta_{xr1} = \frac{6}{1+e^{\frac{V+30}{11.5}}} \tag{S53}$$

$$\tau_{xr1} = \alpha_{xr1} \cdot \beta_{xr1} \tag{S54}$$

$$\frac{\mathrm{d}Xr1}{\mathrm{d}time} = \frac{xr1_{inf} - Xr1}{\tau_{xr1}} \tag{S55}$$

I_{Kr}, *Xr2* gate

$$xr2_{inf} = \frac{1}{1+e^{\frac{V+88}{24}}} \tag{S56}$$

$$\alpha_{xr2} = \frac{3}{1+e^{\frac{-60-V}{20}}} \tag{S57}$$

$$\beta_{xr2} = \frac{1.12}{1+e^{\frac{V-60}{20}}} \tag{S58}$$

$$\tau_{xr2} = \alpha_{xr2} \cdot \beta_{xr2} \tag{S59}$$

$$\frac{\mathrm{d}Xr2}{\mathrm{d}time} = \frac{xr2_{inf} - Xr2}{\tau_{xr2}} \tag{S60}$$

Slow delayed rectifier K^+ current, I_{Ks} [5]

$$I_{Ks} = g_{Ks} \cdot Xs^2 \cdot \left(1 + \frac{0.6}{1+\left(\frac{3.8\times10^{-5}}{Ca_i}\right)^{1.4}}\right) \cdot (V - E_{Ks}) \tag{S61}$$

I_{Ks}, $\boldsymbol{Xs}$ gate

$$xs_{inf} = \frac{1}{1+e^{\frac{-5-V}{14}}} \tag{S62}$$

$$\alpha_{xs} = \frac{1100}{\sqrt{1+e^{\frac{-10-V}{6}}}} \tag{S63}$$

$$\beta_{xs} = \frac{1}{1+e^{\frac{V-60}{20}}} \tag{S64}$$

$$\tau_{xs} = \alpha_{xs} \cdot \beta_{xs} \tag{S65}$$

$$\frac{\mathrm{d}Xs}{\mathrm{d}time} = \frac{xs_{inf} - Xs}{\tau_{xs}} \tag{S66}$$

Inward rectifier K^+ current, I_{K1}

$$\alpha_{K1} = \frac{0.1}{1 + e^{0.06\cdot(V-15-E_K-200)}} \tag{S67}$$

$$\beta_{K1} = \frac{3\cdot e^{0.0002\cdot\left(V-15-E_K+100\right)} + e^{0.1\cdot\left(V-15-E_K-10\right)}}{1+e^{-0.5\cdot\left(V-15-E_K\right)}} \tag{S68}$$

$$xK1_{inf} = \frac{\alpha_{K1}}{\alpha_{K1} + \beta_{K1}} \tag{S69}$$

$$I_{K1} = g_{K1} \cdot xK1_{inf} \cdot \sqrt{\frac{K_o}{5.4}} \cdot (V - E_K) \tag{S70}$$

Hyperpolarization activated funny current, I_f

$$I_f = g_f \cdot Xf \cdot (V - E_f)\,, E_f = -17(mV) \tag{S71}$$

I_f, $\boldsymbol{Xf}$ gate

$$xf_{inf} = \frac{1}{1+e^{\frac{102.4+V}{7.6}}} \tag{S72}$$

$$\frac{dXf}{dtime} = \frac{xf_{inf} - Xf}{\tau_f} \tag{S73}$$

Na^+/K^+ pump current, I_{NaK}

$$I_{NaK} = \frac{\frac{\frac{P_{NaK} \cdot K_o}{K_o + K_{mk}} \cdot Na_i}{Na_i + K_{mNa}}}{1 + 0.1245 \cdot e^{\frac{-0.1 \cdot V \cdot F}{R \cdot T}} + 0.0353 \cdot e^{\frac{-V \cdot F}{R \cdot T}}} \tag{S74}$$

Na^+/Ca^{2+} exchanger current, I_{NaCa}

$$I_{NaCa} = \frac{K_{NaCa} \cdot \left(e^{\frac{\gamma \cdot V \cdot F}{R \cdot T}} \cdot {Na_i}^3 \cdot Ca_o - e^{\frac{(\gamma - 1) \cdot V \cdot F}{R \cdot T}} \cdot {Na_o}^3 \cdot Ca_i \cdot \alpha \right)}{({Km_{Nai}}^3 + {Na_o}^3) \cdot (Km_{Ca} + Ca_o) \cdot \left(1 + K_{sat} \cdot e^{\frac{(\gamma - 1) \cdot V \cdot F}{R \cdot T}} \right)} \tag{S75}$$

Ca^{2+} dynamics

$$I_{rel} = \left(\frac{a_{rel} \cdot {Ca_{SR}}^2}{{b_{rel}}^2 + {Ca_{SR}}^2} + c_{rel} \right) \cdot d \cdot g \tag{S76}$$

$$I_{up} = \frac{Vmax_{up}}{1 + \frac{{K_{up}}^2}{{Ca_i}^2}} \tag{S77}$$

$$I_{leak} = V_{leak} \cdot (Ca_{SR} - Ca_i) \tag{S78}$$

$$g_{inf} = \begin{cases} \frac{1}{1 + \left(\frac{Ca_i}{0.00035} \right)^6}, \text{ if } Ca_i \leq 0.00035 \\ \frac{1}{1 + \left(\frac{Ca_i}{0.00035} \right)^{16}}, \text{ otherwise} \end{cases} \tag{S79}$$

$$\frac{\mathrm{d}g}{\mathrm{d}time} = constg \cdot \frac{g_{inf} - g}{\tau_g} \tag{S80}$$

$$constg = \begin{cases} 0, \text{ if } (g_{inf} > g) \text{ and } (V > -60(mV)) \\ 1, \text{ otherwise} \end{cases} \tag{S81}$$

$$Ca_{i_{bufc}} = \frac{1}{1 + \frac{Buf_c \cdot K_{buf_c}}{\left(Ca_i + K_{buf_c} \right)^2}} \tag{S82}$$

$$Ca_{sr_{bufsr}} = \frac{1}{1 + \frac{Buf_{sr} \cdot K_{buf_{sr}}}{\left(Ca_{SR} + K_{buf_{sr}} \right)^2}} \tag{S83}$$

$$\frac{\mathrm{d}Ca_i}{\mathrm{d}time} = Ca_{i_{bufc}} \cdot \left(I_{leak} - I_{up} + I_{rel} - \frac{\left(I_{CaL} + I_{CaT} + I_{b_{Ca}} + I_{p_{Ca}} - 2 \cdot I_{NaCa} \right)}{2 \cdot V_c \cdot F} \cdot Cm \right) \tag{S84}$$

$$\frac{\mathrm{d}Ca_{SR}}{\mathrm{d}time} = \frac{Ca_{sr_{bufsr}} \cdot V_c}{V_{sr}} \cdot (I_{up} - (I_{rel} + I_{leak})) \tag{S85}$$

Ca^{2+} pump current, I_{pCa}

$$I_{p_{Ca}} = \frac{g_{pCa} \cdot Ca_i}{Ca_i + K_{pCa}} \qquad \text{(S86)}$$

Ca^{2+} background current, I_{bCa}

$$I_{b_{Ca}} = g_{bca} \cdot (V - E_{Ca}) \qquad \text{(S87)}$$

Reversal potentials

$$E_{Na} = \frac{R \cdot T}{F} \cdot \ln \frac{Na_o}{Na_i} \qquad \text{(S88)}$$
$$E_K = \frac{R \cdot T}{F} \cdot \ln \frac{K_o}{K_i} \qquad \text{(S89)}$$
$$E_{Ks} = \frac{R \cdot T}{F} \cdot \ln \frac{K_o + P_{kna} \cdot Na_o}{K_i + P_{kna} \cdot Na_i} \qquad \text{(S90)}$$
$$E_{Ca} = \frac{0.5 \cdot R \cdot T}{F} \cdot \ln \frac{Ca_o}{Ca_i} \qquad \text{(S91)}$$

Interaction with in silico fibroblasts

AP of hESC-CM coupled to N_f fibroblasts evolves according to:

$$\frac{dV}{dt} = -\frac{C_m \cdot I_{ion} + N_f \cdot I_{gap}}{C_m} \qquad \text{(S92)}$$

where I_{ion} represents the global current density across the hESC-CM membrane and I_{gap} the current flowing through the gap junction.

$$I_{gap} = G_{gap} \cdot (V - V_{fibro}) \qquad \text{(S93)}$$

V_{fibro}: fibroblast potential;
$G_{gap} = 1$ (nS): conductance of the hESC-CM - fibroblast coupling [7];
N_f: number of coupled fibroblasts;

The fibroblast AP evolves according to

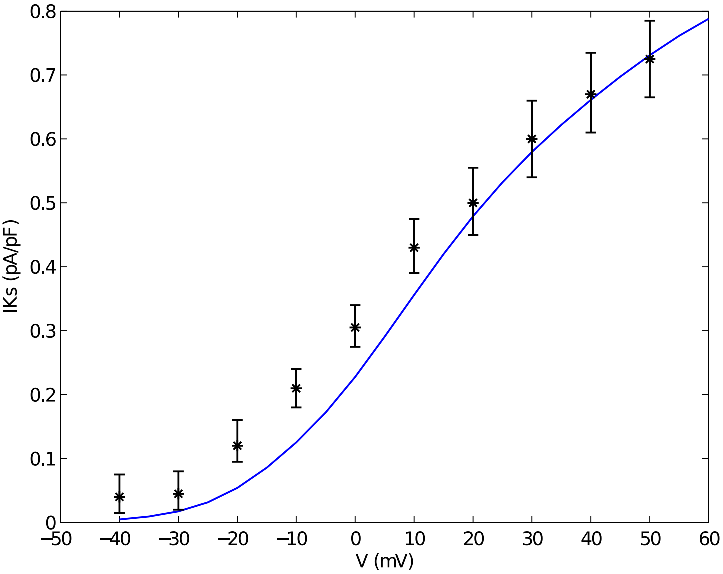

Figure S1: I/V curve for I_{Ks}, obtained with the following protocol: 2 second-test pulses from -40 to 60 mV from an holding potential of -40 mV [8].

$$\frac{dV_{fibro}}{dt} = -\frac{C_{fibro} \cdot I_{fibro}(V_{fibro}) - I_{gap}}{C_{fibro}} \tag{S94}$$

(S94)

$C_{fibro} = 1.6$ (pF): fibroblast capacity;

$I_{fibro}(V_{fibro})$: fibroblast global transmembrane current density;

In particular, $I_{fibro}(V_{fibro})$ is the sum of the four currents identified by MacCannell et al. (delayed rectifying K^+ current, inward rectifying K^+ current, Na^+/K^+ pump current, and background Na^+ current) [7]. The background Na^+ current conductance G_{bNa} changed from 0.0095 nS/pF to 0.003 nS/pF. We set this parameter in order to equal the integrated Na^+ influx through the leak pathway to the Na^+ efflux through the Na^+/K^+ pump. We assume this discrepancy to be caused by differences in the cardiomyocyte model.

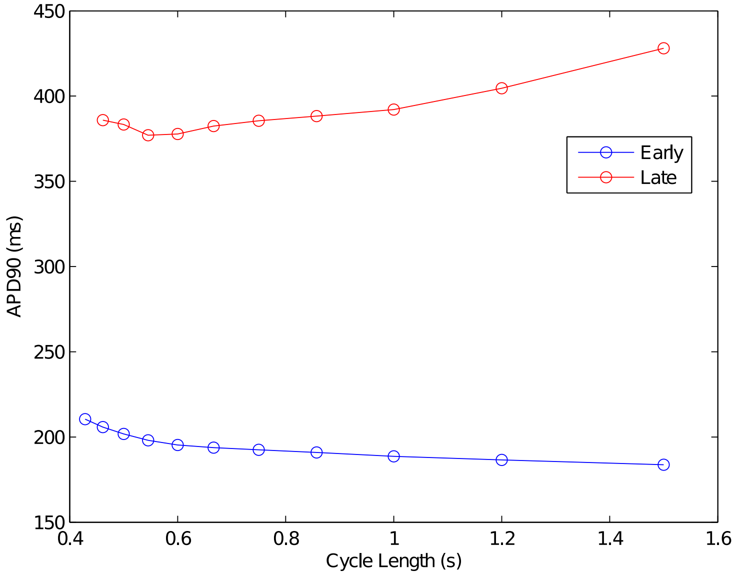

Figure S2: APD90 rate dependence. The used protocol consisted in 300 s with amplitude 0 pA, thus leaving the model reaching spontaneously its own steady state, and then 300 s of stimulation at constant Cycle Length and amplitude 300 pA; then APD90 was computed. At the Early stage no significant APD90 dependence to the stimulus was noticed, while at the Late stage a physiological dependence starts to appear for Cycle Lengths greater than 0.6 s.

Bibliography

[1] Sartiani L, Cerbai E, Lonardo G, DePaoli P, Tattoli M, Cagiano R, Carratù MR, Cuomo V, Mugelli A. Prenatal exposure to carbon monoxide affects postnatal cellular electrophysiological maturation of the rat heart: a potential substrate for arrhythmogenesis in infancy. Circulation January 2004; 109(3):419–423. ISSN 1524-4539.

[2] Sartiani L, Bettiol E, Stillitano F, Mugelli A, Cerbai E, Jaconi ME. Developmental changes in cardiomyocytes differentiated from human embryonic stem cells: a molecular and electrophysiological approach. Stem Cells 2007; 25(5):1136–1144.

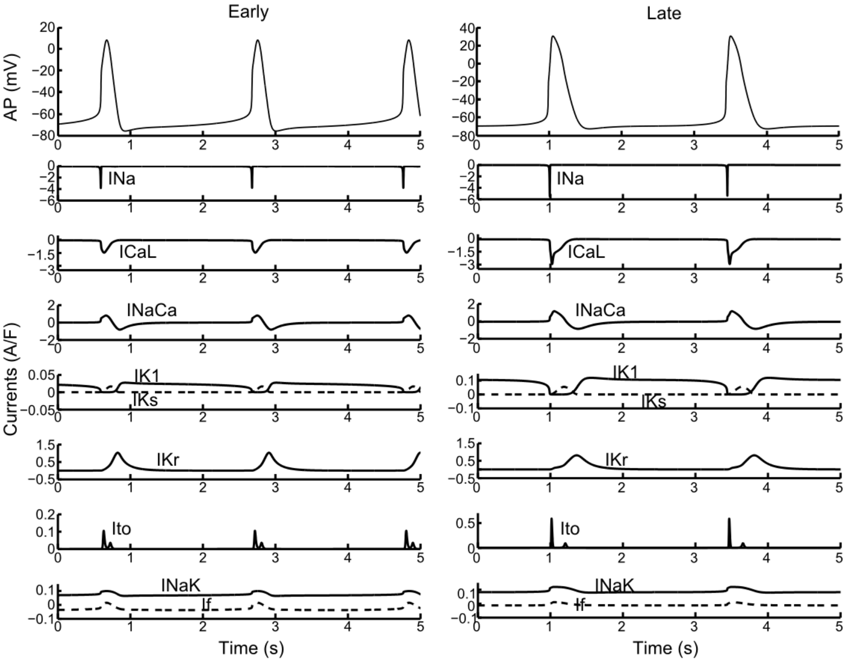

Figure S3: APs and currents at the Early and Late stages.

[3] Barbieri M, Varani K, Cerbai E, Guerra L, Li Q, Borea PA, Mugelli A. Electrophysiological basis for the enhanced cardiac arrhythmogenic effect of isoprenaline in aged spontaneously hypertensive rats. J MOL CELL CARDIOL July 1994;26(7):849–60. ISSN 0022-2828.

[4] ten Tusscher KHWJ, Noble D, Noble PJ, Panfilov AV. A model for human ventricular tissue. Am J Physiol Heart Circ Physiol April 2004;286(4):H1573–1589.

[5] Grandi E, Pasqualini FS, Pes C, Corsi C, Zaza A, Severi S. Theoretical investigation of action potential duration dependence on extracellular Ca2+ in human cardiomyocytes. J Mol Cell Cardiol March 2009;46(3):332–342.

[6] Maltsev Va, Lakatta EG. Synergism of coupled subsarcolemmal Ca2+ clocks and sarcolemmal voltage clocks confers robust and flexible pacemaker function in a novel pacemaker cell model. Am J Physiol Heart Circ Physiol March 2009; 296(3):H594–615. ISSN 0363-6135.

[7] MacCannell KA, Bazzazi H, Chilton L, Shibukawa Y, Clark RB, Giles WR. A mathematical model of electrotonic interactions between ventricular myocytes and fibroblasts. Biophys J June 2007;92(11):4121–4132. ISSN 0006-3495.

[8] Wang K, Terrenoire C, Sampson KJ, Iyer V, Osteen JD, Lu J, Keller G, Kotton DN, Kass RS. Biophysical properties of slow potassium channels in human embryonic stem cell derived cardiomyocytes implicate subunit stoichiometry. The Journal of physiology December 2011;589(Pt 24):6093–6104. ISSN 1469-7793.

SUPPLEMENTARY METHODS: COMPUTATIONAL MODELS OF VENTRICULAR-LIKE AND ATRIAL-LIKE HUMAN INDUCED PLURIPOTENT STEM CELL DERIVED CARDIOMYOCYTES

Formulation of the hiPSC-CM model

All the time constants in *ms*

Extracellular and intracellular ionic concentrations

$$Na_o = 151\ (mM)$$

$$K_o = 5.4\ (mM)$$

$$Ca_o = 1.8\ (mM)$$

$$Na_i = \begin{cases} 10\ (mM)\ ,\ Ventricular-like \\ 14.75\ (mM)\ ,\ Atrial-like \end{cases}$$

$$K_i = 150\ (mM)$$

$$Ca_i = 0.0002\ (mM)$$

$$Ca_{SR} = 0.3\ (mM)$$

Cell size and dimensions

$$Cm = \begin{cases} 98.7109\ (pF)\ ,\ Ventricular-like \\ 78.6671\ (pF)\ ,\quad Atrial-like \end{cases}$$

$$V_c = \begin{cases} 8752.72\ (um^3)\ ,\ Ventricular-like \\ 6975.44\ (um^3)\ ,\quad Atrial-like \end{cases}$$

$$V_{sr} = \begin{cases} 583.73\ (um^3)\ ,\ Ventricular-like \\ 465.20\ (um^3)\ ,\quad Atrial-like \end{cases}$$

Maximum conductances and currents

$$g_{Na} = \begin{cases} 4.0701e3\ (S/F)\ ,\ Ventricular-like \\ 6.8878e3\ (S/F)\ ,\quad Atrial-like \end{cases}$$

$$g_{CaL} = 8.5502e-5\,(m^3/(F \cdot s))$$

$$g_{to} = \begin{cases} 29.9038\ (S/F)\ ,\ Ventricular-like \\ 59.8077\ (S/F)\ ,\quad Atrial-like \end{cases}$$

$$g_{Kr} = 29.8667\,(S/F)$$

$$g_{Ks} = 2.041\ (S/F)$$

$$g_{K1} = \begin{cases} 28.1492\ (S/F)\ ,\ Ventricular-like \\ 16.8895\ (S/F)\ ,\quad Atrial-like \end{cases}$$

$$g_f = 39.9826\ (S/F)$$

$$P_{NaK} = \begin{cases} 1.0896\ \ (A/F)\ ,\ Ventricular-like \\ 0.87168\ \ (A/F)\ ,\quad Atrial-like \end{cases}$$

$$K_{NaCa} = \begin{cases} 6125\ (A/F)\ ,\ Ventricular-like \\ 2143.75\ (A/F)\ ,\quad Atrial-like \end{cases}$$

$$a_{rel} = 16.464\ (mM/s)$$

$$b_{rel} = 0.25\ (mM)$$

$$c_{rel} = 8.232\ (mM/s)$$

$$Vmax_{up} = \begin{cases} 1.4016\ (mM/s)\ ,\ Ventricular - like \\ 0.35938\ (mM/s)\ ,\ Atrial - like \end{cases}$$

$$V_{leak} = 4.4444e - 4\ (1/s)$$

$$g_{pCa} = 0.4125(A/F)$$

Other constants

$$Buf_c = 0.25\ (mM)$$

$$Buf_{sr} = 10\ (mM)$$

$$K_{buf_c} = 0.001\ (mM)$$

$$K_{buf_{sr}} = 0.3\ (mM)$$

$$K_{up} = 0.00025\ (mM)$$

$$K_{pCa} = 0.0005\ (mM)$$

$$F = 96485.3415\ (C \times mM)$$

$$R = 8.314472\ (J/(M \times K))$$

$$T = 310\ (K)$$

$$L_0 = 0.025\ (dimensionless)$$

$$P_{kna} = 0.03\ (dimensionless)$$

$$K_{sat} = 0.1\ (dimensionless)$$

$$Km_{Ca} = 1.38\ (mM)$$

$$Km\ _{ai} = 87.5\ (mM)$$

$$\alpha = 3.571429\ (dimensionless)$$

$$\gamma = 0.35\ (dimensionless)$$

$$K_{mNa} = 40\ (mM)$$

$$K_{mk} = 1\ (mM)$$

Initial conditions

$$h_0 = 0.75\,(\,dimensionless)$$

$$j_0 = 0.75\,(\,dimensionless)$$

$$m_0 = 0\ \ (\,dimensionless)$$

$$d_0 =\ 0\ (\,dimensionless)$$

$$fCa_0 =\ 1\ (\,dimensionless)$$

$$f_{1,0} =\ 1\ (\,dimensionless)$$

$$f_{2,0} = 1\ \ (\,dimensionless)$$

$$r_0 =\ 0\ (\,dimensionless)$$

$$q_0 =\ 1\ \ (\,dimensionless)$$

$$Xr1_0 = 0\,(\,dimensionless)$$

$$Xr2_0 = 1\ (\,dimensionless)$$

$$Xs_0 = 0\,(\,dimensionless)$$

$$Xf_0 = 0\,.1\,(\,dimensionless)$$

$$g_0 =\ 0\ (\,dimensionless)$$

$$V_0 =\ -70 \cdot 10^{-3}\ (\,V)$$

Membrane Potential

$$\begin{aligned}&\frac{\mathrm{d}V}{\mathrm{d}time} = -I_{ion} = \\ &= -\left(I_{K1} + I_{to} + I_{Kr} + I_{Ks} + I_{CaL} + I_{NaK} + I_{Na} + I_{NaCa} + I_{p_{Ca}} + I_f\right)\end{aligned} \tag{S1}$$

Na$^+$ current, I$_{Na}$

$$I_{Na} = g_{Na} \cdot m^3 \cdot h \cdot j \cdot (V - E_{Na}) \tag{S2}$$

I$_{Na}$, h gate

$$h_{inf} = \frac{1}{\sqrt{\left(1+e^{\frac{V+72.1}{5.7}}\right)}} \tag{S3}$$

$$\alpha_h = \begin{cases} 0.057 \cdot e^{\frac{-(V+80)}{6.8}}, \, if \, V < -40 \\ 0, \, otherwise \end{cases} \tag{S4}$$

$$\beta_h = \begin{cases} 2.7 \cdot e^{0.079 \cdot V} + 3.1 \times 10^5 \cdot e^{0.3485 \cdot V}, \, if \, V < -40 \\ \frac{0.77}{0.13 \cdot \left(1+e^{\frac{V+10.66}{-11.1}}\right)}, \, otherwise \end{cases} \tag{S5}$$

$$\tau_h = \begin{cases} \frac{1.5}{\alpha_h+\beta_h}, \, V < -40 \, mV \\ 2.542 \, , \, V \geq -40 \, mV \end{cases} \tag{S6}$$

$$\frac{\mathrm{d}h}{\mathrm{d}time} = \frac{h_{inf}-h}{\tau_h} \tag{S7}$$

I$_{Na}$, j gate

$$j_{inf} = h_{inf} \tag{S8}$$

$$\alpha_j = \begin{cases} \frac{\left(-25428 \cdot e^{0.2444 \cdot V} - 6.948 \times 10^{-6} \cdot e^{-0.04391 \cdot V}\right) \cdot (V+37.78)}{1+e^{0.311 \cdot (V+79.23)}}, \, if \, V < -40 \\ 0, \, otherwise \end{cases} \tag{S9}$$

$$\beta_j = \begin{cases} \frac{0.02424 \cdot e^{-0.01052 \cdot V}}{1+e^{-0.1378 \cdot (V+40.14)}}, \, if \, V < -40 \\ \frac{0.6 \cdot e^{0.057 \cdot V}}{1+e^{-0.1 \cdot (V+32)}}, \, otherwise \end{cases} \tag{S10}$$

$$\tau_j = \frac{7}{\alpha_j+\beta_j} \tag{S11}$$

$$\frac{\mathrm{d}j}{\mathrm{d}time} = \frac{j_{inf}-j}{\tau_j} \tag{S12}$$

I$_{Na}$, m gate

$$m_{inf} = \frac{1}{\left(1+e^{\frac{-34.1-V}{5.1}}\right)^{1/3}} \tag{S13}$$

$$\alpha_m = \frac{1}{1+e^{\frac{-60-V}{5}}} \tag{S14}$$

$$\beta_m = \frac{0.1}{1+e^{\frac{V+35}{5}}} + \frac{0.1}{1+e^{\frac{V-50}{200}}} \tag{S15}$$

$$\tau_m = \alpha_m \cdot \beta_m \tag{S16}$$

$$\frac{\mathrm{d}m}{\mathrm{d}time} = \frac{m_{inf}-m}{\tau_m} \tag{S17}$$

L-type Ca^{2+} current, I$_{CaL}$

$$I_{CaL} = \frac{g_{CaL} \cdot 4 \cdot V \cdot F^2}{R \cdot T} \cdot \frac{\left(Ca_i \cdot e^{\frac{2 \cdot V \cdot F}{R \cdot T}} - 0.341 \cdot Ca_o\right)}{e^{\frac{2 \cdot V \cdot F}{R \cdot T}} - 1} \cdot d \cdot f_1 \cdot f_2 \cdot fCa \tag{S18}$$

$\mathbf{I}_{CaL}$, d gate

$$d_{inf} = \begin{cases} \frac{1}{1+e^{-\frac{V+9.1}{7}}} & , Ventricular - like \\ \frac{1}{1+e^{-\frac{V+5.986}{7}}} & , Atrial - like \end{cases} \tag{S19}$$

$$\alpha_d = \frac{1.4}{1+e^{\frac{-35-V}{13}}} + 0.25 \tag{S20}$$

$$\beta_d = \frac{1.4}{1+e^{\frac{V+5}{5}}} \tag{S21}$$

$$\gamma_d = \frac{1}{1+e^{\frac{50-V}{20}}} \tag{S22}$$

$$\tau_d = \alpha_d \cdot \beta_d + \gamma_d \tag{S23}$$

$$\frac{\mathrm{d}d}{\mathrm{d}time} = \frac{d_{inf}-d}{\tau_d} \tag{S24}$$

$\mathbf{I}_{CaL}$, $\mathbf{f}_{Ca}$ gate

$$\alpha_{fCa} = \frac{1}{1+\left(\frac{Ca_i}{0.0006}\right)^8} \tag{S25}$$

$$\beta_{fCa} = \frac{0.1}{1+e^{\frac{Ca_i-0.0009}{0.0001}}} \tag{S26}$$

$$\gamma_{fCa} = \frac{0.3}{1+e^{\frac{Ca_i-0.00075}{0.0008}}} \tag{S27}$$

$$fCa_{inf} = \frac{\alpha_{fCa}+\beta_{fCa}+_{fCa}}{1.3156} \tag{S28}$$

$$\tau_{fCa} = 2\ (ms) \tag{S29}$$

$$\frac{\mathrm{d}fCa}{\mathrm{d}t} = constfCa \cdot \frac{fCa_{inf}-fCa}{\tau_{fCa}} \tag{S30}$$

$$constfCa = \begin{cases} 0,\ if\ (fCa_{inf} > fCa)\ and\ (V > -60\ (mV)) \\ 1,\ otherwise \end{cases} \tag{S31}$$

$\mathbf{I}_{CaL}$, $\mathbf{f}_1$ gate

$$f_{1inf} = \begin{cases} \frac{1}{1+e^{\frac{V+26}{3}}}, & Ventricular - like \\ \frac{1}{1+e^{\frac{V+25.226}{3}}}, & Atrial - like \end{cases} \tag{S32}$$

$$\tau_{f1} = \left(1102.5 \cdot e^{-\left[\frac{(V+27)^2}{15}\right]^2} + \frac{200}{1+e^{\frac{13-V}{10}}} + \frac{180}{1+e^{\frac{V+30}{10}}} + 20\right) \cdot \tag{S33}$$

$$\cdot \begin{cases} \left(1 + 1433 \cdot (Ca_i - 50 \times 10^{-6})\right) & , \frac{df}{dtime} > 0 \\ 1 & , otherwise \end{cases}$$

$$\frac{\mathrm{d}f_1}{\mathrm{d}time} = \frac{f_{1inf}-f_1}{\tau_{f1}} \tag{S34}$$

$\mathbf{I}_{CaL}$, $\mathbf{f}_2$ gate

$$f_{2inf} = \begin{cases} \frac{0.67}{1+e^{\frac{V+35}{7}}} + 0.33 \ , \ Ventricular - like \\ \frac{0.67}{1+e^{\frac{V+31.226}{7}}} + 0.33 \ , \quad Atrial - like \end{cases} \tag{S35}$$

$$\tau_{f2} = \left(600 \cdot e^{-\frac{(V+25)^2}{170}} + \frac{31}{1+e^{\frac{25-V}{10}}} + \frac{16}{1+e^{\frac{V+30}{10}}}\right) \cdot \begin{cases} 1, Ventricular - like \\ 2 \qquad , Atrial - like \end{cases} \tag{S36}$$

$$\frac{\mathrm{d}f_2}{\mathrm{d}time} = \frac{f_{2inf} - f_2}{\tau_{f2}} \tag{S37}$$

Transient outward current, $\mathbf{I}_{to}$

$$I_{to} = g_{to} \cdot r \cdot q \cdot (V - E_K) \tag{S38}$$

$\mathbf{I}_{to}$, r gate

$$r_{inf} = \frac{1}{1+e^{\frac{22.3-V}{12}}} \tag{S39}$$

$$\tau_r = \frac{14.40516}{1.037e^{0.09 \cdot (V+30.61)} + 0.369e^{-0.12 \cdot (V+23.84)}} + 2.75352 \tag{S40}$$

$$\frac{\mathrm{d}r}{\mathrm{d}time} = \frac{r_{inf} - r}{\tau_r} \tag{S41}$$

$\mathbf{I}_{to}$, q gate

$$q_{inf} = \frac{1}{1+e^{\frac{V+53}{13}}} \tag{S42}$$

$$\tau_q = \frac{39.102}{0.57e^{-0.08 \cdot (V+44)} + 0.065e^{0.1 \cdot (V+45.93)}} + 6.06 \ \mathrm{(S43)}$$

$$\frac{\mathrm{d}q}{\mathrm{d}time} = \frac{q_{inf} - q}{\tau_q} \tag{S44}$$

Rapid delayed rectifier $\mathbf{K}^+$ current, $\mathbf{I}_{Kr}$

$$I_{Kr} = g_{Kr} \cdot \sqrt{\frac{K_o}{5.4}} \cdot Xr1 \cdot Xr2 \cdot (V - E_K) \tag{S45}$$

$\mathbf{I}_{Kr}$, Xr1 gate

$$V_{1/2} = 1000 \cdot \left(-\frac{R \cdot T}{F \cdot Q} \cdot ln\left(\frac{\left(1+\frac{Ca_o}{2.6}\right)^4}{L_0 \cdot \left(1+\frac{Ca_o}{0.58}\right)^4}\right) - 0.019\right) \tag{S46}$$

$$xr1_{inf} = \frac{1}{1+e^{\frac{V_{1/2}-V}{4.9}}} \tag{S47}$$

$$\alpha_{xr1} = \frac{450}{1+e^{\frac{-45-V}{10}}} \tag{S48}$$

$$\beta_{xr1} = \frac{6}{1+e^{\frac{V+30}{11.5}}} \tag{S49}$$

$$\tau_{xr1} = \alpha_{xr1} \cdot \beta_{xr1} \tag{S50}$$

$$\frac{\mathrm{d}Xr1}{\mathrm{d}time} = \frac{xr1_{inf} - Xr1}{\tau_{xr1}} \tag{S51}$$

I$_{Kr}$, Xr2 gate

$$xr2_{inf} = \frac{1}{1+e^{\frac{V+88}{50}}} \tag{S52}$$

$$\alpha_{xr2} = \frac{3}{1+e^{\frac{-60-V}{20}}} \tag{S53}$$

$$\beta_{xr2} = \frac{1.12}{1+e^{\frac{V-60}{20}}} \tag{S54}$$

$$\tau_{xr2} = \alpha_{xr2} \cdot \beta_{xr2} \tag{S55}$$

$$\frac{\mathrm{d}Xr2}{\mathrm{d}time} = \frac{xr2_{inf} - Xr2}{\tau_{xr2}} \tag{S56}$$

Slow delayed rectifier K$^+$ current, I$_{Ks}$

$$I_{Ks} = g_{Ks} \cdot Xs^2 \cdot \left(1 + \frac{0.6}{1+\left(\frac{3.8\times10^{-5}}{Ca_i}\right)^{1.4}}\right) \cdot (V - E_{Ks}) \tag{S57}$$

I$_{Ks}$, Xs gate

$$xs_{inf} = \frac{1}{1+e^{\frac{-20-V}{16}}} \tag{S58}$$

$$\alpha_{xs} = \frac{1100}{\sqrt{1+e^{\frac{-10-V}{6}}}} \tag{S59}$$

$$\beta_{xs} = \frac{1}{1+e^{\frac{V-60}{20}}} \tag{S60}$$

$$\tau_{xs} = \alpha_{xs} \cdot \beta_{xs} \tag{S61}$$

$$\frac{\mathrm{d}Xs}{\mathrm{d}time} = \frac{xs_{inf} - Xs}{\tau_{xs}} \tag{S62}$$

Inward rectifier K$^+$ current, I$_{K1}$

$$\alpha_{K1} = \frac{3.91}{1+e^{0.5942\cdot(V-E_K-200)}} \tag{S63}$$

$$\beta_{K1} = \frac{-1.509\cdot e^{0.0002\cdot(V-E_K+100)} + e^{0.5886\cdot(V-E_K-10)}}{1+e^{0.4547\cdot(V-E_K)}} \tag{S64}$$

$$xK1_{inf} = \frac{\alpha_{K1}}{\alpha_{K1}+\beta_{K1}} \tag{S65}$$

$$I_{K1} = g_{K1} \cdot xK1_{inf} \cdot \sqrt{\frac{K_o}{5.4}} \cdot (V - E_K) \tag{S66}$$

Hyperpolarization activated funny current, I$_f$

$$I_f = g_f \cdot Xf \cdot (V - E_f) \tag{S67}$$

$\mathbf{I}_f$, Xf gate

$$xf_{inf} = \frac{1}{1+e^{\frac{V+77.85}{5}}} \tag{S68}$$

$$\tau_f = 1900\ (ms) \tag{S69}$$

$$\frac{dXf}{dtime} = \frac{xf_{inf}-Xf}{\tau_f} \tag{S70}$$

Na$^+$/K$^+$ pump current, $\mathbf{I}_{NaK}$

$$I_{NaK} = \frac{\frac{\frac{P_{NaK}\cdot K_o}{K_o+K_{mk}}\cdot Na_i}{Na_i+K_{mNa}}}{1+0.1245\cdot e^{\frac{-0.1\cdot V\cdot F}{R\cdot T}}+0.0353\cdot e^{\frac{-V\cdot F}{R\cdot T}}} \tag{S71}$$

Na$^+$/Ca^{2+} exchanger current, $\mathbf{I}_{NaCa}$

$$I_{NaCa} = \frac{K_{NaCa}\cdot\left(e^{\frac{\gamma\cdot V\cdot F}{R\cdot T}}\cdot Na_i^3\cdot Ca_o - e^{\frac{(\gamma-1)\cdot V\cdot F}{R\cdot T}}\cdot Na_o^3\cdot Ca_i\cdot\alpha\right)}{(Km_{Nai}^3+Na_o^3)\cdot(Km_{Ca}+Ca_o)\cdot\left(1+K_{sat}\cdot e^{\frac{(\gamma-1)\cdot V\cdot F}{R\cdot T}}\right)} \tag{S72}$$

Ca^{2+} dynamics

$$I_{rel} = \left(\frac{a_{rel}\cdot Ca_{SR}^2}{b_{rel}^2+Ca_{SR}^2}+c_{rel}\right)\cdot d\cdot g\cdot\left\{\begin{array}{cc} 0.0411\ , & Ventricular-like \\ 0.0556\ , & Atrial-like \end{array}\right. \tag{S73}$$

$$I_{up} = \frac{Vmax_{up}}{1+\frac{K_{up}^2}{Ca_i^2}} \tag{S74}$$

$$I_{leak} = V_{leak}\cdot(Ca_{SR}-Ca_i) \tag{S75}$$

$$g_{inf} = \left\{\begin{array}{l} \frac{1}{1+\left(\frac{Ca_i}{0.00035}\right)^6},\ \mathrm{i}f\ Ca_i \leq 0.00035 \\ \frac{1}{1+\left(\frac{Ca_i}{0.00035}\right)^{16}},\ otherwise \end{array}\right. \tag{S76}$$

$$\frac{\mathrm{d}g}{\mathrm{d}time} = const2\cdot\frac{g_{inf}-g}{\tau_g} \tag{S77}$$

$$\tau_g = 2\ (ms) \tag{S78}$$

$$const2 = \left\{\begin{array}{cc} 0,\ if\ (g_{inf}>g)\ and\ (V>-60\,(mV)) \\ 1, & otherwise \end{array}\right. \tag{S79}$$

$$Ca_{i_{bufc}} = \frac{1}{1+\frac{Buf_c\cdot K_{buf_c}}{\left(Ca_i+K_{buf_c}\right)^2}} \tag{S80}$$

$$Ca_{sr_{bufsr}} = \frac{1}{1+\frac{Buf_{sr}\cdot K_{buf_{sr}}}{\left(Ca_{SR}+K_{buf_{sr}}\right)^2}} \tag{S81}$$

$$\frac{\mathrm{d}Ca_i}{\mathrm{d}time} = Ca_{i_{bufc}}\cdot\left(I_{leak}-I_{up}+I_{rel}-\frac{\left(I_{CaL}+I_{p_{Ca}}-2\cdot I_{NaCa}\right)}{2\cdot V_c\cdot F}\cdot Cm\right) \tag{S82}$$

$$\frac{\mathrm{d}Ca_{SR}}{\mathrm{d}time} = \frac{Ca_{sr_{bufsr}}\cdot V_c}{V_{sr}}\cdot(I_{up}-(I_{rel}+I_{leak})) \tag{S83}$$

Ca^{2+} pump current, I_{pCa}

$$I_{pCa} = \frac{g_{pCa} \cdot Ca_i}{Ca_i + K_{pCa}} \tag{S84}$$

Na^{+} dynamics

$$\frac{\mathrm{d}Na_i}{\mathrm{d}time} = -C_m \cdot \frac{I_{Na} + 3I_{NaK} + 3I_{NaCa}}{F \cdot V_c}$$

Reversal potentials

$$E_{Na} = \frac{R \cdot T}{F} \cdot \ln \frac{Na_o}{Na_i} \tag{S85}$$

$$E_K = \frac{R \cdot T}{F} \cdot \ln \frac{K_o}{K_i} \tag{S86}$$

$$E_{Ks} = \frac{R \cdot T}{F} \cdot \ln \frac{K_o + P_{kna} \cdot Na_o}{K_i + P_{kna} \cdot Na_i} \tag{S87}$$

$$E_{Ca} = \frac{0.5 \cdot R \cdot T}{F} \cdot \ln \frac{Ca_o}{Ca_i} \tag{S88}$$

$$E_f = -17\ (mV) \tag{S89}$$

Current blocker simulations with the atrial-like model

Additional simulations of the effect of Tetrodotoxine (TTX), Nifedipine (Nifed), E4031 and 3R4S-Chromanol 293B (Chr) were performed with the atrial-like model. The stimulation protocol is constant pacing rate 80 bpm (1.3333 Hz) with depolarizing pulses of 5 ms duration and 550 pA amplitude. Results are consistent with those obtained with the ventricular-like model: (i) TTX (I_{Na} blocker) produces an important shift in time of the AP peak (Fig. S4a); (ii) Nifed ($\mathrm{I}_{\mathrm{CaL}}$ blocker) causes the reduction of the APDs and triangulates the AP shape (Fig. S4b); (iii) E4031 (I_{Kr} blocker) lengthens the APD (Fig. S4c); (iv) Chr (I_{Ks} blocker) does not affect significantly the AP shape (Fig. S4d).

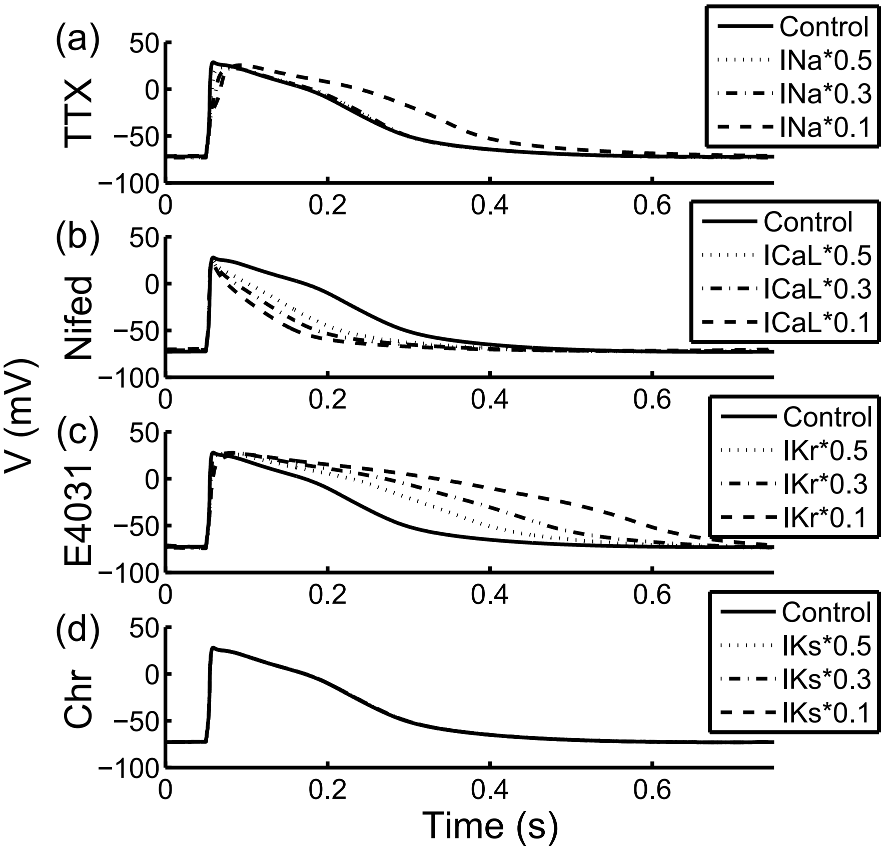

Figure S4: Simulations of the effects of the 4 current blockers on the atrial-like AP.